General solutions to temperature distribution in orthotropic systems subject to variable heat transfer and biological systems during bioheat transfer

by

DAIPAYAN SARKAR

Presented to the Faculty of the Graduate School of
The University of Texas at Arlington in Partial Fulfillment
of the Requirements
for the Degree of

DOCTOR OF PHILOSOPHY

THE UNIVERSITY OF TEXAS AT ARLINGTON

August 2016

To Diya

our Parents

& all my Teachers

ACKNOWLEDGEMENTS

I would like to start by acknowledging Prof. Ankur Jain for accepting me as a Doctoral student in his research group. He has always motivated and pushed me to solve fundamental problems in science and engineering. A quality of him I truly appreciate is his ability to identify a fundamental problem in the large pool of archival publications. Professor, with rise in demand of numerical simulations, I will always cherish the memories of us visiting the white board to do math. I hope we continue this exercise in future. However in the event I am not 'in the lab', I am sure we will find a way around it. Thank you for your vision, guidance, patience, tolerance and providing me with the necessary resources to prepare for a future in academia. I acknowledge the generous support by the Department of Mechanical and Aerospace Engineering and College of Engineering which helped me work on the research presented in this dissertation.

My sincere gratitude towards Prof. A. Haji-Sheikh, my co-advisor. The discussions we have had over the last six years will always be the foundation of future directions that I pursue in my academic and personal life. I have always been intrigued about your curiosity in finding patterns and transformations for mathematical equations representing ode's, pde's, eigenvalue estimation,etc. From observations of my Master's thesis, where you were my supervising professor, I can share this thought - you are the thermal wave and I am the wake region of the wave. I shall always remain in debt for the knowledge I gained working under your supervision.

My doctoral committee - Prof. Benito Chen-Charpentier, Prof. Kamesh Subbarao and Prof. Seiichi Nomura for providing me with suggestions and comments

to improve several aspects of this dissertation. I have been extremely fortunate in learning from the courses, discussing research and seeking help related to the work presented in this dissertation. I will continue to learn from you all!

My sincere acknowledgments to Prof. Vinod Srinivasan and Prof. Richard Goldstein at University of Minnesota and generous support from IUSSTF, for providing me with an opportunity to work in collaboration and co-author on a publication. Prof. Srinivasan, the summer at IISc, Bangalore was a great experience in terms of research and brainstorming over several fundamental and applied problems. I hope we continue working on some exciting problems related to thermal-fluid science.

Many others have contributed towards helping me prepare this dissertation. The staff at MAE - Debi and Lanie have always been so kind and helpful. My lab members at MTL, providing me with feedback during weekly group presentations. Special thanks to Vivek, Krishna, Dean, Ratnesh, Divya and Swapnil with whom I have extensively discussed research and co-authored on some publications. Friends over the years - Saeed, Thanuj, Ashwin, George, Nilabh, Puloma, Debapriya, Shubhodeep, Upa, Soumyava, Alok & company for helping me vent when the pressure was high!

My gratitude and love towards my wife Somdutta, our parents - Maa and Baba and Mitra Sir for the countless sacrifices you all have made. I have always reasoned with the existence of solutions, an expression to capture the physical nature of transport, one equation to express the entire physics of the problem! However, I have failed in my pursuit towards you Maa. I am starting again, maybe not from scratch, but certainly with a bag full of hope to find answers to what put us all in a state of non-equilibrium. So I ask, will we ever regain equilibrium? In your loving memory, I dedicate this attempt to you.

August 4, 2016

ABSTRACT

General solutions to temperature distribution in orthotropic systems subject to variable heat transfer and biological systems during bioheat transfer

DAIPAYAN SARKAR, Ph.D.

The University of Texas at Arlington, 2016

Supervising Professors: Ankur Jain and A. Haji-Sheikh

Bioheat transfer is the phenomenon of heat transfer in biological systems where the dominant modes of heat transfer are conduction and advection. Other factors such as rate of metabolism that are unique to biological systems contribute significantly towards bioheat transfer. In the present work, the Pennes bioheat equation has been solved for a multilayer system to derive steady state and transient temperature solutions in the multilayer skin tissue with a tumor. In nanoparticle based hyperthermia therapy, the body temperature elevates from the physiological core body temperature, 37° C. Analytical solutions for three different therapeutic techniques have been developed to predict the steady state temperature distribution for a five-layer perfused skin tissue model. The transient bioheat model based on Pennes equation introduces an additional challenge for determining the temperature in a two dimensional multilayer skin tissue model. The existence of both real and imaginary eigenvalues in the temperature solution makes it different from classical transient heat conduction problems. This observation has been addressed by introducing a special transformation which modifies the temperature solution such that the tran-

sient solution agrees well with the results from the steady state model. The transient temperature model accounts for the specific absorption rate (SAR) as a function of both space and time. Finally, temperature in vascular tissue with a tumor of any arbitrary shape is derived. The equation for the tumor boundary can be determined using medical imaging techniques. In addition, different values for thermo-physical and physiological parameters are accounted for in the tissue and tumor region of the vasculature. This helps in determining the temperature distribution in the vascular tissue as a function of SAR for nanoparticle assisted hyperthermia therapy which is critical for planning nanoparticle assisted thermal based therapy for cancer.

Another fundamental heat transfer problem is that of the cooling of a cylinder, such as temperature in a Li-ion cell is examined when subject to variable heat transfer. In particular, a general solution for the temperature distribution in the cylinder is derived, accounting for circumferential varying convective heat transfer coefficient around the cylinder, and orthotropic thermal conductivity of the cylinder. This solution procedure is later extended to derive an analytical temperature in an orthotropic and partially orthotropic sphere subject to circumferential varying heat transfer coefficient. A general solution for temperature can provide very fast and highly accurate solutions for different functionally graded materials, heat generation/dissipation rates subject to different cooling loads. Finally, the mathematical procedure derived earlier is applied to estimate the error in steady- state heat transfer measurements due to lateral conduction effects in the heater foil. The error due to lateral conduction effects is quantified by a heat flux correction factor. Correlations for peak error as a function of non-dimensional parameters such as Biot number, ratio of maximum to minimum heat transfer and gradient of shear layer, for both slot and radial jets are obtained. These correlations can help experimentalists estimate error during measurement of steady-state heat transfer coefficient.

TABLE OF CONTENTS

LIST OF FIGURES

LIST OF TABLES

CHAPTER 1

INTRODUCTION

Thermal transport in biological and energy conversion systems have been topics of significant technological importance in recent times. General solutions for temperature in such biological and engineered systems provide good understanding of the physics of thermal transport and also act as an analytical tool that can be used for accurate temperature estimation for variety of cases. This is important as one needs to account for various physiological process while analyzing thermal transport in a human body for therapeutic purposes. In the case of non-biological systems, a general expression for temperature field estimation can provide fast and highly accurate results in comparison to numerical simulations. However, careful interpretation of these analytical solutions are required since they are developed for much simpler geometries than encountered by most engineering and biological systems.

Heat transfer in biological systems is an integral part for design and planning therapies for a disease like cancer, to improve the quality of life of patients and their life expectancy. Researchers in science, oncology, engineering and mathematics participate in addressing such problems related to health-care and translational medicine, study fundamentals of transport and it's application to design of novel therapeutics to develop protocol for an efficient and cost-effective solution. Modern therapeutic measures for treating tumors includes thermo-chemotherapy [3–5] and photo-dynamic therapy [6–9], where in heat generated from exciting nanoparticles is used to destroy tumor cells. However, to date the two most popular choice as recommended by on-

cologists across world still remain chemical based therapy such as chemotherapy and radiation.

In applications related to cryosurgery the heat transfer coefficient is known to vary spatially. For non-biological systems, such as batteries, microprocessors, gas turbines, etc. use this variation in heat transfer coefficient to enhance heat transfer from a surface and thereby ensuring safe device operation. The most common technique of thermal management of such low-high power devices for proper device operation is convective cooling. Convective cooling is known to vary spatially primarily due to fluid flow across objects generating or dissipating moderate to high heat fluxes. Such variation in flow field is incorporated in the heat transfer coefficient which can be used to accurately predict the temperature distribution inside these systems. Furthermore, a general temperature solution accounting for orthotropic thermal properties of novel engineered energy conversion systems subject to spatially varying convective heat transfer can account for thermal management of such devices and contribute towards the design of next generation energy systems for safe operating cycles.

Our focus in preparing this dissertation is in-line with two such areas. They can be broadly categorized as: (1) Thermal based therapy of biological systems such as the human body for treating fatal diseases such as cancer (2) Heat transfer in orthotropic systems (Li-ion batteries) when subject to variable heat transfer. In the best of our interest and the reader, we define the set of problems presented in this dissertation, as a collection of the following chapters.

Thermal transport in tissues is an important physical phenomenon for both healthy and diseased tissue. A significant amount of research in bioheat transfer over the past few decades has led to an understanding of the governing dynamics of thermal transport in a tissue [10–12]. A number of thermal based therapeutic measures have been developed and adopted in practice, including laser surgery, cryosurgery,

magnetic nanoparticle based hyperthermia and chemotherapy [13]. Several models governing the flow of heat in tissues have been proposed. A classical model was presented by H.H. Pennes in 1948 [10], followed by several refinements and related models [12, 14, 15]. Detailed reviews of these bioheat transfer models are also available [14, 15]. The Pennes model includes the effect of heat transfer in a biological body due to diffusion, advection, volumetric heat generation due to metabolism and spatial heating. Thermophysical properties of blood and various tissue have been measured using a variety of methods [16]. The skin tissue can broadly be classified into muscle, subcutaneous and dermal regions. The thermo-physical properties of each region differs from the others and hence consideration of a multi-layer model is necessary for accurate estimation of temperature used in planning of thermal based therapy. The Pennes model is used widely due to its simplicity, but it must be modified depending on unique attributes of the tissue under study. This model includes the effect of heat transfer in a biological body due to diffusion, advection, volumetric heat generation due to metabolism and spatial heating. Diffusion and transient thermal effects in any tissue are based on its thermo- physical properties such as thermal conductivity, density and specific heat. The Pennes equation accounts for blood flow through an advection term, consisting of the thermophysical properties of blood along with the difference between the blood temperature and the local tissue temperature. Some analytical work has been reported on solving the Pennes bioheat transfer equation for specific conditions. Deng et al. reported a closed form analytical solution for spatial and time dependent surface or volumetric conditions using the Greens function method [17]. Laplace transform was used to study the transient effects of sinusoidal heat flux on a one-dimensional semi-infinite tissue [13]. Mahjoob and Vafai developed an analytical model for a biological tissue, assuming a porous media with contributions due to conduction between tissue and vascular system, con-

vective heat transfer between blood and tissue, heat generation due to metabolism and induced surface heat flux [18]. A dual layer biological media was also considered, and analytical solutions for two specific cases were discussed [19]. An analytical study of an axisymmetric tissue-vascular system is used to analyze the effect due to the radio-frequency ablation treatment due to volumetric heat generation in the tissue region due to a heater probe [20]. The application of Pennes equation to magnetic fluid hyperthermia has been studied, where a theoretical solution is presented for a spherical tumor surrounded by a thin shell of magnetic nanoparticles [21]. An analytical model was proposed to investigate the rate of cell destruction during a freezethaw cryosurgical procedure, in order to minimize damage to healthy cells [22]. Steady state temperature distribution in a one dimensional cylindrical tissue has been developed for human limbs [23]. Steady state thermal penetration depth has been derived analytically using method based on Laplace transforms [24]. Analytical solution based on the Laplace transforms is used to solve a two-dimensional Pennes bioheat equation for both Fourier and non-Fourier heat conduction effects for a cylindrical skin tissue [25]. In addition to such analytical models, numerical solutions have also been developed for scenarios where temperature solutions are difficult to determine explicitly. Steady state temperature in breast cancer was studied numerically through user-defined functions to account for blood perfusion and metabolism [26]. An investigation of minimum invasive methods such as microwave thermal therapy was performed both numerically and experimentally, in vivo and in vitro, to determine the extent of the tissue injury [27]. Temperature solution in a system with time-dependent spatial heating has been studied numerically [28]. The cooling of human brain and neck in emergency medical situations has been studied using finite element simulations [29]. In a recent finite element based analysis, an alternating magnetic field is applied to ferrofluids to generate heat inside a tumor. The Pennes bioheat

equation was coupled with Maxwells equation in the finite element model to calculate the input parameters such as the magnetic flux intensity [30]. Skin surface cooling based on optical window contact cooling, cryogenic spray cooling are considered for the Pennes bioheat equation and Weinbaum - Jiji bioheat model. Combined conduction and radiation effects are considered in Pennes equation and the temperature field in the multilayer tissue structure is computed numerically [31]. A number of experimental investigations of bioheat transfer in tissue have also been reported. The different theories involved with hyperthermia treatment were verified by performing experiments on a large bovine kidney by turning it into tissue phantom using alcohol fixation technique [32]. Most of these papers investigate therapy of cancerous tissue, including electroporation-based chemotherapy [33–35], magnetic nanoparticle based heating [21,36] and gold nanoparticle laser heating [37] . In a recent study, a high resolution micro-computed tomography imaging system has been used to investigate the concentration and distribution of injected nanoparticles. Also nanoparticle induced volumetric heat generation rate was measured experimentally [36]. Several studies on estimating the thermal damage potential due to Joule heating and the importance of considering the multilayer nature of skin tissue have also been presented [38, 39]. In a related work, detection of shape, size and depth of a melanoma lesion by applying a cold stimulus at the surface has been reported [40]. In addition, an extension to Pennes bioheat equation is made to include the effect of water evaporation during in the tissue during laser heating. A source term is added to the Pennes bioheat equation to account for the energy required for evaporation process to occur, based on which, a relationship for effective specific heat is derived. Experiments on a liver tissue along with numerical solutions are presented to illustrate the effect of water evaporation from the tissue [41].

Another fundamental topic of importance is the estimation of temperature field in anisotropic systems which are subject to variable heat transfer cooling. The fundamental and applied nature of this research can be easily related to industry applications, such as cooling of microprocessors using liquid jets, cooling of turbine blades using jet impingement and cooling of batteries using natural and forced convection. Such variation in heat transfer due to impinging jets can also lead to lateral conduction errors in transient and steady state heat transfer measurements. Flow past 'blunt bodies' has been a field of study for several decades. Past research has mostly focused towards flow characterization, without much focus in analyzing the temperature distribution inside geometries subject to spatially varying heat transfer. Convective heat transfer between a solid body and fluid flow past the body is an important technological problem for which a vast amount of literature on experimental investigation as well as theoretical modeling exists [42, 43]. For fluid flow past a solid body, the convective heat transfer coefficient h at the surface of the body is known to vary spatially. For the specific case of flow past a cylinder, the variation of h as a function of the circumferential angle, θ is well known. This variation has been experimentally measured for a number of Reynolds numbers [43], and has also been computed by solving the governing energy and momentum conservation equations of the flow [44, 45]. Starting from the stagnation point ($\theta = 0°$), h first decreases due to laminar boundary layer development. For laminar flow, a minima is reached at around $\theta = 80°$ where separation occurs. For large values of the Reynolds number Re, a sharp increase occurs beyond the first minima due to transition to turbulence, following which a second minima occurs due to separation at around $\theta = 140°$. For the case of flow past a cylinder, the velocity and temperature boundary layer in the flow around the cylinder have been computed theoretically and analytically [45]. However, not much work exists that addresses the computation of temperature within the cylinder while accounting for

the θ-dependence of h. The problem of variable convective heat transfer coefficient occurs commonly in the thermal analysis of extended surfaces [46]. This problem has been analyzed in a number of papers. Steady state temperature distribution for a one dimensional rectangular fin with temperature-dependent heat transfer coefficient has been presented [47]. A solution method to determine temperature involving direct integration of the governing differential equation has been presented [48]. A method based on Fourier series expansion has been adopted to determine the two-dimensional temperature field in a rectangular fin in which the heat transfer coefficient varies along the length of the fin [49]. Another paper analyzes the variable heat transfer coefficient problem for computing temperature in the thermal entry region of a hydrodynamically developed duct flow [50]. The Frobenius series expansion technique has been used for fins with different cross-sectional areas with varying heat transfer coefficients [51]. Another paper highlights the performance of annular fins of different profiles when subjected to variable heat transfer coefficient [52]. Semi-analytical solution methods such as the Galerkin based integral method has also been adopted to account for variable heat transfer coefficient in fins [53]. An inverse problem that estimates the functional form of the heat flux at the base of the fin when the surface of the fin is subjected to variable heat transfer coefficient has been presented [54]. Another paper has addressed the inverse problem of computing the space dependent heat transfer coefficient when temperature at certain locations inside the body at certain locations is known *a priori* [55]. A hybrid numerical scheme has been used for transient thermo-elastic analysis of an annular fin [56]. Numerical analysis has also been carried out for determining the transient natural convective heat transfer with variable heat transfer coefficient in the case of domestic refrigerators [57]. The literature cited above indicates that the variable heat transfer coefficient problem has been adequately addressed for extended surfaces. However, there is a lack of literature for

addressing variable heat transfer coefficient in the context of cross flow past a solid cylinder, a problem of considerable technological importance. This is particularly so when thermal conduction inside the cylinder is anisotropic in nature. Recent research on Li-ion batteries suggests the existence of strong anisotropy in thermal conduction in Li-ion cells [2]. Thermal conductivity measurements indicate a 100-fold difference in thermal conductivity in the radial and axial directions [2]. The cooling of Li-ion cells is a problem of much technological importance [58]. Li-ion cells are commonly used energy storage and conversion, and thermal runaway is a significant problem in insufficiently cooled Li-ion cells, which in extreme cases leads to explosion and fire, as evidenced in recent incidents on aircraft [59]. As a result, it is important to develop analytical techniques for computing the temperature of a Li-ion cells that account for the anisotropic nature of thermal conduction within the cell, and also the variable convective heat transfer coefficient around the cell that may occur due to flow of a coolant fluid past the cell.

An extension to flow across a cylinder is that for flow past a sphere where the convective heat transfer coefficient is also known to vary with both azimuthal and polar angles, ϕ and θ, respectively. The dependence of h around the periphery of the sphere has been studied for a variety of flow conditions [45, 60, 61]. The value of the heat transfer coefficient is the largest at the stagnation point ($\phi = 0°$) where flow impinges, following which, h first decreases due to laminar boundary layer development. For laminar flow, a minima is reached at around ($\phi = 109.6°$) where separation occurs [45,60]. The temperature and velocity fields in the flow around the sphere have been measured and numerically computed [62]. The overall heat transfer coefficient was measured for three small spheres in a fluid flow and a relationship between heat transfer, flow velocity and fluid properties was derived using experimental data [63]. An analytical solution for transient heat transfer from a sphere

at low Reynolds number under steady velocity conditions has been developed [64]. Analytical solution for unsteady heat transfer at small Peclet numbers has been developed when the surface temperature of the sphere undergoes a step change [65]. In addition to such analytical approaches, numerical methods have also been used to analyze cases with space-varying heat transfer coefficient. A finite difference based model has been adopted to study the transient heat transfer of a solid sphere in cross flow [66].

Finally, temperature distribution in solids subject to variable temperature can come useful in experimental measurements for heat and mass transfer. The trend of increasing inlet temperatures in gas turbines and the corresponding high cooling requirements of turbine blades requires the development of novel cooling schemes. Accurate measurements that characterize the performance of these cooling schemes are critical for reliable design. In order to estimate the true operating temperatures of various hot section components, designers rely on heat transfer coefficient data obtained from low temperature tests. Small errors in measurements of the heat transfer coefficient can lead to moderate uncertainties in metal operating temperature, and large uncertainties in blade lifetime prediction [67]. Despite considerable care taken by researchers, it is well known that uncertainties in heat transfer experiments are rarely less than $8 - 10\%$. Several techniques are currently used for the measurement of heat transfer coefficients in lab-scale experiments. In recent years, thermocouple-based measurements of temperature at discrete spatial locations have almost completely given way to high resolution whole surface measurements utilizing Thermochromic Liquid Crystals (TLCs), Infra-Red Thermography (IRT), Temperature Sensitive Paint (TSP) or Pressure Sensitive Paint (PSP). All of these techniques, when carefully calibrated, enable temperature measurements with high spatial resolution and low measurement uncertainty of the order of 0.5 K [68]. Independent of the

temperature measurement technique, there are mainly two methods for measurement of heat transfer coefficient on a surface, given by the thermal boundary condition on the surface. Steady-state measurements typically use a constant heat flux surface, established by thin metal foil heaters. The local heat transfer coefficient is found by the relation, $h(\vec{r}) = q_w/(T_w - T_\infty)$ where q_w is the convective heat flux into the fluid after subtracting losses from the power input. The heat loss can be minimized by insulating the heater foil from the back, i.e. on the side not exposed to the flow, and by minimizing radiation loss, which may not always be possible. The uncertainty in estimation of the lost power input can be reduced by having a good knowledge of the emissivity of the foil material, and the thermal properties of the insulation.

Transient experiments utilize the assumption of one dimensional conduction into a semi-infinite medium in order to reconstruct the heat transfer coefficient. The surface temperature field is measured at two different times, and the data are plugged into an analytical solution to extract the heat transfer coefficient. This method and its several variations have been extended for simultaneous calculation of heat transfer coefficient and cooling effectiveness in film cooling flows [69]. Mass transfer based measurements, such as the naphthalene sublimation technique [70], measure transport coefficient distributions over a sublimating surface. Using the analogy between heat and mass transfer in boundary layer flows, these mass transfer distributions can be converted to heat transfer coefficient distributions. Each of these techniques have distinct advantages and disadvantages. Steady-state measurements are conceptually simple and are easy to set up. When used with TLCs, the technique is inexpensive but time-consuming. The transient IR technique is often preferred nowadays, but requires greater care in calibration of the IR camera [71]. Both these techniques suffer from the deficiency that a $1 - D$ conduction model is assumed for the heat flux in one instance, and for the thermal penetration in the other. As such, both

methods are unreliable in regions of strong lateral variation of heat transfer coefficient or geometry. The mass transfer technique based on naphthalene sublimation avoids many of these issues. This technique implicitly simulates a constant temperature boundary condition, and is not subject to lateral conduction error. This technique is capable of very high spatial resolution, and the conversion from mass transfer coefficients (Sherwood numbers) to heat transfer coefficients (Nusselt numbers) has been shown to be reliable in complex systems such as end-wall secondary flows [72]; however, it has not been fully established for regions with recirculating flows, such as immediately downstream of film holes or backward facing steps, or in regions where erosion may cause mass transfer, such as stagnation points of impinging jets.

The lateral conduction error introduced in steady state heat transfer measurements. Lateral conduction errors arise when a constant wall flux is assumed in the presence of large gradients in heat transfer coefficient. If the flux in the heater were purely normal to the surface, these gradients in heat transfer coefficient would cause large gradients in wall temperature. As a result, the path of least thermal resistance from below a low-heat transfer region may involve lateral conduction along the foil into the region of high heat transfer. Such lateral conduction within the foil leads to a non-uniform wall-normal heat flux distribution, which needs to be accounted for during the data reduction process. For the transient heat transfer technique utilizing the assumption of conduction into a semi-infinite medium, the effects of lateral conduction have been documented and analyzed. An early study was by Vedula and Metzger [73], who performed numerical simulations to quantify the effect of lateral conduction, including the effect of anisotropic conduction. Lin and Wang [74] used an inverse 3-D algorithm to avoid making the 1-D heat transfer approximation when processing the raw hue data. They attribute the 12% difference between their results and the results of the $1 - D$ procedure to the effect of lateral conduction. Kingsley-

Rowe et al. [75] used a modified version of the $1-D$ analytical solution and applied a Biot number correction in order to calculate the heat transfer coefficient in the presence of lateral conduction. Bons [76] applied a finite volume method to study the effect of lateral conduction in the presence of surface roughness and showed that the $1-D$ model is inadequate for rough surfaces, due to large peak-to-valley variation in heat transfer coefficients. A comprehensive model for the effects of flow temperature variation and heater foil response in conjunction with lateral conduction on the measurement uncertainty has been presented by von Wolfersdorf and co-workers [77, 78].

These studies confirm that the effects of lateral conduction are most pronounced when there are sharp gradients in the heat transfer coefficient. Such sharp gradients exist at several locations on a modern gas turbine blade, such as the point of laminar/turbulent transition, stagnation points on blade leading edge, as well as on internal channels cooled by shower-head film holes, and separation/reattachment regions near tip/hub end-walls. As an example, consider the distribution of transport coefficient along the blade suction surface shown in Figure 1.1 for a representative high-performance blade profile [1]. Starting from its peak near the leading edge stagnation point, the Sherwood number drops by a factor of 4 over a stream-wise distance of 10% of blade chord. Similarly, near the trailing edge, the Sherwood number rises by a factor of 6 over a stream-wise distance of 20% of the blade chord, due to laminar-turbulent transition. Such sharp gradients can occur in a region where the upstream and downstream transport coefficients are relatively uniform (as for $Tu = 18\%$ in the figure) or near a point of nominal symmetry, such as the leading edge.

While the effect of lateral conduction has been well investigated for the transient measurement technique, little information is available on the appropriate correction for the steady state technique. The steady state technique continues to be used by several groups for gas turbine heat transfer [79, 80]. Partly, this is because a quick

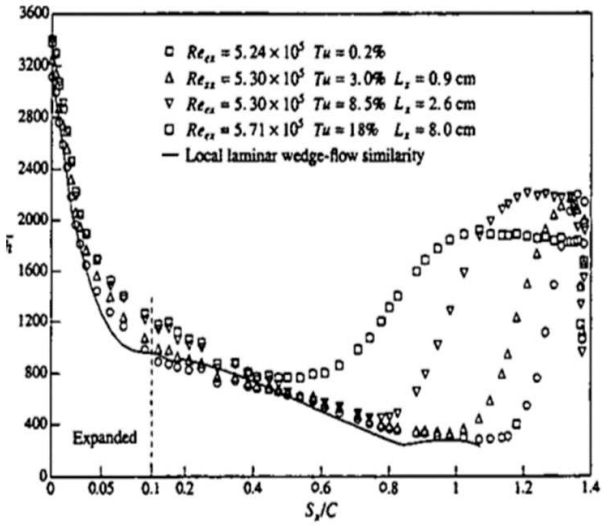

Figure 1.1. Mid-span Sherwood number distribution on the suction surface of a high performance turbine rotor blade (reproduced with permission from Wang et. al, 1998, [1]).

estimate for the lateral conduction correction can be obtained by taking the Laplacian of the observed temperature field on the surface, and adding/subtracting that to the nominal heat flux [81]. However, as we will show, the exact error is sensitive to the location of the gradient region and the behavior of the heat transfer coefficient profile on either side of the gradient region. In this chapter, we outline a technique to estimate *a priori* the error due to the assumption of a uniform wall heat flux in a steady state heat transfer experiment.

In subsequent sections of this dissertation, chapters 2 - 4 presents general solutions for temperature field in multilayer skin tissue in the presence of tumor. Chapter 2, illustrates a time independent analysis of temperature distribution in multi-layer skin tissue in the presence of a tumor [82, 83]. Chapter 3, extends this concept to a transient analysis wherein different spatial heating patterns of tumor site are considered to accurately model the time dependent temperature field. This helps in

monitoring the temperature field of the targeted region of tissue and the tumor simultaneously. It has been found that the existence of both positive and negative eigenvalues (complex) contribute equally towards the temperature solution. This is an important observation as due to varying properties in different layers of tissue, the location of the starting eigenvalue continuously varies. The scenario of missing an eigenvalue due to error in algorithm for locating the first root, may lead to error in the predicted value temperature which is not a desirable outcome for thermal based therapy for cancer [84]. Chapter 4, the tissue and tumor thermo-physical properties are considered to differ. An appropriate model is considered for estimating temperature field inside the vascular tissue during magnetic fluid hyperthermia induced on an arbitrary shaped primary tumor. This model gives the practitioner flexibility in identifying different specific absorption rates for tumors of different sizes and characteristics. Such an analysis can become useful as a tool in predictive oncology for treating different kinds of tumors in different regions of the body [85]. Chapter 5, illustrates a mathematical procedure based on Fourier series expansion to theoretically estimate the steady state temperature distribution in an orthotropic solid cylinder when subject to varying heat transfer. Such applications of cross-flow over a cylinder can be related to cooling of Lithium ion batteries, nuclear fuel rods, etc [86]. Chapter 6, extends the mathematical treatment to an orthotropic spherical system. One challenge is to find candidate functions to satisfy the Legendre differential equation with half-integer coefficients. This chapter presents a general approach using two different methodologies, in estimating of temperature field inside spheres with orthotropic thermal properties [87]. In chapter 7, the mathematical procedure to solve variable heat transfer problems developed above in chapters 5 and 6 is applied to estimate the presence of lateral conduction errors in steady-state heat transfer measurements due to impinging jets. Heat flux correction curves illustrates the percentage error in

steady state heat transfer measurements and correlations provide a tool for experimentalists in design of experimental procedure for measurement of local heat/mass transfer coefficient [88]. Finally, chapter 8 concludes the dissertation and presents a short discussion on future directions and some applications of analytical temperature models developed for biological and engineering systems.

CHAPTER 2

STEADY-STATE TEMPERATURE IN MULTILAYER SKIN TISSUE

2.1 Introduction

Analytical solutions for heat conduction in multilayer bodies have been proposed for other engineering applications [89–91], however, bioheat transfer in a multilayer structure like skin tissue presents additional challenges due to the more complicated nature of the transport phenomena leading to a modified governing equation. This chapter presents the analytical derivation of temperature distribution for a two-dimensional, five layer skin tissue in the presence of a tumor.The tumor is located in the dermal layer of the tissue. The Pennes bioheat equation is solved analytically for a multilayer geometry with varying thermal properties and bio-transport parameters in the layers. Modeling the reaction term adds an additional challenge in the analytical framework since the blood perfusion rate varies in different layers of the tissue. Further, it is found that the analytical treatment needs to be modified significantly depending on the nature of the boundary condition, based on the therapeutic treatment adopted, at the top of the skin surface. In addition to different physical boundary conditions and the reaction term, the analytical solution also includes the effect of metabolism in every layer of the skin tissue, modeled as a volumetric source and the tumor heating region is modeled as a spatially dependent source term. Results are found to be in good agreement with finite-element simulations. The analytical model is used for understanding the thermal effect of hyperthermia therapy in the multilayer skin tissue. Results presented here may help improve the understanding of thermal

transport in multi-layered tissue such as skin, and in particular contribute towards effective thermal-based therapies for skin cancers [82].

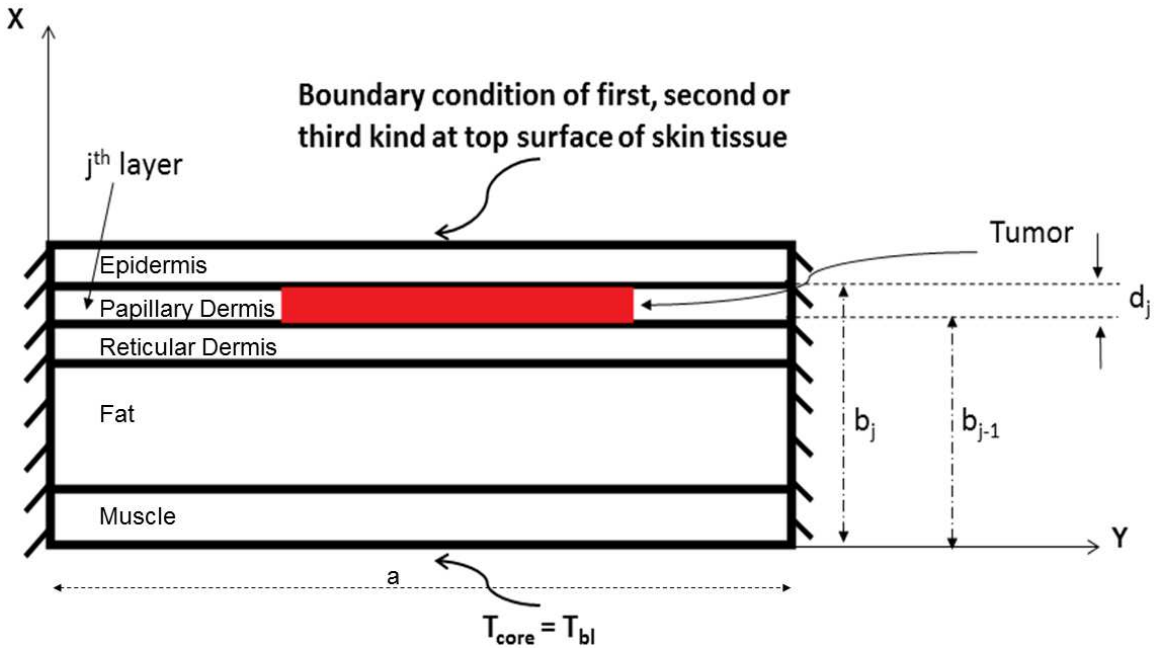

Figure 2.1. Multilayer skin tissue with tumor.

2.2 Mathematical Model

In this section the mathematical derivation of temperature distributions in a multilayer biological body is discussed. Consider the geometry of a five-layer skin tissue shown schematically in Figure 2.1. Consider the presence of a tumor of a given size in the dermal layer. Heat generation in the tumor, as well as boundary conditions of the top and bottom surfaces result in a temperature field in the multilayer tissue. In order to determine this temperature field analytically, the Pennes bioheat equation for each layer is solved, accounting for temperature and heat flux compatibility at the interfaces between adjacent layers. Solutions are derived for three specific boundary

conditions - prescribed temperature, surface heat flux and convective cooling. While the governing equation remains the same for each case, some algebraic modifications to the source term in the governing equation is needed to capture the effect of various terms. The governing energy equation for each layer is given by,

$$\frac{\partial^2 T_j}{\partial x^2} + \frac{\partial^2 T_j}{\partial y^2} - m_j^2(T_j - T_{bl}) + \frac{g_{met,j}}{k_j} + \delta_j \frac{g_{t,j}}{k_j} = 0 \tag{2.1}$$

where,

$$m_j^2 = \left(\frac{w_j \rho c}{k_j}\right)_{bl} \tag{2.2}$$

In 2.1, $g_{met,j}$ refers to the volumetric heat generation inside a tissue due to metabolism. $g_{t,j}(y)$ refers to inherent heat generation in the tumor due to thermal based therapy. The factor δ_j is introduced to determine the presence or absence of the tumor in the j^{th} layer. Other parameters such as w_j, ρ, c and k_j refer to blood perfusion rate, density of blood, specific heat of blood and thermal conductivity of tissue. The temperature $T_j(x, y)$ refers to the temperature at any spatial location inside the tissue. The core of the skin tissue is held at a constant temperature of $T_{bl} = 37^\circ$ C, and side walls are assumed to be adiabatic.

$$T_1 = T_{bl} \qquad \text{at } x = 0 \tag{2.3}$$

$$\frac{\partial T_j}{\partial y} = 0 \qquad \text{at } y = 0, a \tag{2.4}$$

Due to the multilayer nature of the problem, additional equations are obtained from compatibility at the interface between adjacent layers. Assuming perfect thermal contact,

$$T_j = T_{j+1} \qquad \text{at} x = b_j,\ j = 1, 2, 3, 4 \tag{2.5}$$

$$k_j \left(\frac{\partial T_j}{\partial x} \right) = k_{j+1} \left(\frac{\partial T_{j+1}}{\partial x} \right) \qquad \text{at } x = b_j,\ j = 1, 2, 3, 4 \tag{2.6}$$

Three specific boundary conditions that model various physical phenomena at the top of the skin are considered next.

2.2.1 Temperature prescribed at the top surface of skin tissue

This sub-section considers the case where a prescribed temperature is applied at the top surface of the skin tissue.

$$T_5 = T_{sur} \qquad \text{at } x = b_5 \tag{2.7}$$

The solution to equations (2.1)-(2.7) can be obtained by the following superposition technique,

$$T_j(x, y) = T_{j,r}(x) + T_{j,s}(x, y) \tag{2.8}$$

Substituting equation (2.8) in the equations (2.1)-(2.7) results in the following set of equations for $T_{j,r}(x)$:

$$\frac{\partial^2 T_{j,r}}{\partial x^2} = 0 \tag{2.9}$$

$$T_{1,r} = T_{bl} \qquad \text{at } x = 0 \tag{2.10}$$

$$T_{5,r} = T_{sur} \qquad \text{at } x = b_5 \tag{2.11}$$

Similarly the $T_{j,s}(x, y)$ problem is given by:

$$\frac{\partial^2 T_{j_s}}{\partial x^2} + \frac{\partial^2 T_{j,s}}{\partial y^2} - m_j^2 T_{j_s} + \frac{g_{met,j}}{k_j} + \delta_j \frac{g_{t,j}}{k_j} + m_j^2 T_{bl} - m_j^2 T_{j,r}(x) = 0 \tag{2.12}$$

$$T_{1,s} = 0 \qquad \text{at } x = 0 \tag{2.13}$$

$$T_{5,s} = 0 \qquad \text{at } x = b_5 \tag{2.14}$$

$$\frac{\partial T_{j,s}}{\partial y} = 0 \qquad \text{at } y = 0, a \tag{2.15}$$

Note that both $T_{j,r}(x)$ and $T_{j,s}(x, y)$ follow interface compatibility equations similar to equations (2.5) and (2.6). The solution for $T_{j,r}(x)$ is obtained using resistor network analogy [42] as follows:

$$T_{j,r}(x) = T_{j-1,r}(b_{j-1}) + Q\left(\frac{x - b_{j-1}}{a k_j}\right) \tag{2.16}$$

where,

$$Q = \frac{T_{sur} - T_{bl}}{\sum_{j=1}^{5} \frac{d_j}{k_j}} \tag{2.17}$$

where $d_j = b_j - b_{j-1}$ The solution for $T_{j,s}(x, y)$ is obtained using the method of separation of variables, starting with a general transformation,

$$T_{j,s}(x,y) = \sum_{n=0}^{\infty}\sum_{p=1}^{\infty} C_{np} X_{p,j,s}(x) Y_{n,j,s}(y) \tag{2.18}$$

$$\psi_{j,s}(x,y) = \frac{g_{met,j}}{k_j} + \delta_j \frac{g_{t,j}}{k_j} + m_j^2 T_{bl} - m_j^2 T_{j,r}(x) \tag{2.19}$$

Substituting equations (2.18) and (2.19) into equation (2.12) results in

$$\sum_{n=0}^{\infty}\sum_{p=1}^{\infty} C_{np}(\gamma_p^2 + \beta_n^2 + m_j^2) X_{p,j,s}(x) Y_{n,j,s}(y) = \psi_{j,s}(x,y) \tag{2.20}$$

where γ_p and β_n are the eigenvalues. The respective ordinary differential equations in X and $Y$are given by,

$$\frac{X''_{j,s}}{X_{j,s}} = -\gamma_p^2 \qquad \forall \quad p \in Z^+ \tag{2.21}$$

$$\frac{Y''_{j,s}}{Y_{j,s}} = -\beta_n^2 \qquad \forall \quad n \in Z^+ \tag{2.22}$$

Solutions to equations (2.22) and (2.23) are obtained as follows:

$$X_{j,s} = A_{j,s}\cos(\gamma_p(x - b_{j-1})) + B_{j,s}\sin(\gamma_p(x - b_{j-1})) \tag{2.23}$$

$$Y_{j,s} = \cos(\beta_n y); \qquad \beta_n = \frac{n\pi}{a} \qquad \forall \quad n \in Z^* \tag{2.24}$$

The coefficients in equation (2.23) are obtained by using the compatibility condition at the interface of adjacent layers. The coefficients are found out to be governed by recursive relations [89],

$$A_{j+1,s} = A_{j,s}\cos(\gamma_p d_j) + B_{j,s}\sin(\gamma_p d_j) \qquad ; j = 1,2,3,4 \tag{2.25}$$

$$B_{j+1,s} = \frac{k_j}{k_{j+1}}\left(-A_{j,s}\sin(\gamma_p d_j) + B_{j,s}\sin(\gamma_p d_j)\right) \qquad ; j = 1,2,3,4 \tag{2.26}$$

where the coefficients A_1 is zero. B_1 can be selected as any constant. A value of $B_1 = 1$ is selected arbitrarily to be as one. The final step is to determine the series coefficients in equation (2.21) using the orthogonality principle [92],

$$C_{np} = \frac{\sum_{j=1}^{5} \int_{y=0}^{a} \int_{x=b_{j-1}}^{b_j} k_j \left(\frac{\Psi_{j,s}(x,y) X_{p,j,s}(x)}{\gamma_p^2 + \beta_n^2 + m_j^2} \right) Y_{n,j,s}(y) dx dy}{N_x N_y} \tag{2.27}$$

where, the respective norm integrals N_x and N_y are calculated as,

$$N_x = \sum_{j=1}^{5} \int_{x=b_{j-1}}^{b_j} k_j X_{p,j}^2(x) dx \tag{2.28}$$

$$N_y = \int_{y=0}^{a} Y_{n,j}^2(y) dy \tag{2.29}$$

An expression for the final solution for case 2.2.1 is obtained by adding the two solutions,

$$T_j(x,y) = T_{j-1,r}(b_{j-1}) + \frac{T_{sur} - T_{bl}}{\sum_{j=1}^{5} \frac{d_j}{k_j}} \left(\frac{x - b_{j-1}}{a k_j} \right) + \sum_{n=0}^{\infty} \sum_{p=1}^{\infty} \frac{\sum_{j=1}^{5} \int_{y=0}^{a} \int_{x=b_{j-1}}^{b_j} k_j \left(\frac{\Psi_{j,s}(x,y) X_{p,j,s}(x)}{\gamma_p^2 + \beta_n^2 + m_j^2} \right) Y_{n,j,s}(y) dx dy}{N_x N_y} X_{p,j,s}(x) Y_{n,j,s}(y) \tag{2.30}$$

2.2.2 Heat flux prescribed at the top surface of skin tissue

The second case considers a prescribed heat flux applied at the top surface of the skin tissue. The governing equations for this case are given by equations (2.1, 2.3, 2.4), similar to case 2.2.1. In addition, equation (2.7) in section 2.2.1 is replaced by,

$$k_5 \frac{\partial T_5}{\partial x} = q_{sur}(y) \qquad \text{at } x = b_5 \tag{2.31}$$

The solution procedure for equations (2.1)-(2.6) and (2.31) proceeds along similar lines as the solution in section 2.2.1. However, an additional transformation is required, wherein the core body temperature T_{bl} is subtracted out from the temperature distribution:

$$\tilde{T_j}(x,y) = T_j(x,y) - T_{bl} \tag{2.32}$$

The ˜ notation is dropped for convenience and from equation (2.32)the following problem is described to analyze temperature rise:

$$\frac{\partial^2 T_j}{\partial x^2} + \frac{\partial^2 T_j}{\partial y^2} - m_j^2 T_j + \frac{g_{met,j}}{k_j} + \delta_j \frac{g_{t,j}}{k_j} = 0 \tag{2.33}$$

$$T_1 = 0 \qquad \text{at } x = 0 \tag{2.34}$$

$$\frac{\partial T_j}{\partial y} = 0 \qquad \text{at } y = 0, a \tag{2.35}$$

$$\frac{\partial T_5}{\partial x} = \frac{q_{sur}}{k_5} \qquad \text{at } x = b_5 \tag{2.36}$$

Similar to the previous sub-section, $T_j(x,y)$ is split into two components to account for the two non-homogeneities in the governing equations,

$$T_j(x,y) = T_{j,f}(x,y) + T_{j,s}(x,y) \tag{2.37}$$

Inserting equation (2.36) in equation (2.33) we obtain the following set of equations given by,

$$\frac{\partial^2 T_{j,f}}{\partial x^2} + \frac{\partial^2 T_{j,f}}{\partial y^2} - m_j^2 T_{j,f} = 0 \tag{2.38}$$

$$\frac{\partial^2 T_{j,s}}{\partial x^2} + \frac{\partial^2 T_{j,s}}{\partial y^2} - m_j^2 T_{j,s} + \frac{g_{met,j}}{k_j} + \delta_j \frac{g_{t,j}}{k_j} = 0 \tag{2.39}$$

$T_{j,s}(x,y)$ can be determined using a procedure similar to $T_{j,s}(x,y)$ in the previous subsection, with a minor change in the value of the coefficients.$T_{j,f}(x,y)$ presents additional difficulty as discussed below. This derivation starts with the transformation,

$$T_{j,f}(x,y) = \sum_{n=0}^{\infty} D_n X_{n,j,f}(x) Y_{n,j} \tag{2.40}$$

Substituting equation (2.40) in equation (2.38) results in,

$$\frac{X''_{j,s}}{X_{j,s}} + \frac{Y''_{j,s}}{Y_{j,s}} - m_j^2 = 0 \qquad \forall \quad n \in Z^* \tag{2.41}$$

$X_j(x,y)$ and $Y_j(x,y)$ can be separated as follows:

$$\frac{Y''_{j,s}}{Y_{j,s}} = -\beta_n^2 \qquad \forall \quad n \in Z^* \tag{2.42}$$

and

$$\frac{X''_{j,s}}{X_{j,s}} = \beta_n^2 + m_j^2 = \eta_n^2 \qquad \forall \quad n \in Z^* \tag{2.43}$$

Solution to the differential equations (2.42) and (2.43) are given by,

$$Y_{j,s} = \cos(\beta_n y); \qquad \beta_n = \frac{n\pi}{a} \qquad \forall \quad n \in Z^* \tag{2.44}$$

$$X_{n,j,f} = E_{n,j,f} \cosh(\eta_n (x - b_{j-1})) + F_{n,j,f} \sinh(\eta_n (x - b_{j-1})) \quad \forall \quad n \in Z^* \tag{2.45}$$

Note that in the special case of $m_j = 0$, i.e., zero blood perfusion rate in layer j, η_n in equation (2.43) becomes zero for $n = 0$. As a result, for $m_j = 0$ and $n = 0$ is given by the following expression instead of equation (2.45),

$$X_{0,j,f} = E_{0,j,f}(x - b_{j-1}) + F_{0,j,f} \qquad ; \quad m_j = 0, n = 0 \tag{2.46}$$

In this specific case, this scenario is encountered for the epidermis layer ($m_5 = 0$) due to zero perfusion rate of blood in that layer [93]. Heat flux and temperature compatibility at the interfaces are used to derive expressions for the coefficients in equations (2.45) and (2.46):

$$\begin{aligned} E_{n,j+1,f} &= E_{n,j,f}\cosh(\eta_n d_j) + F_{n,j,f}\sinh(\eta_n d_j)\ ; j = 1,2,3,4, n \neq 0, m_j \neq 0 \\ F_{n,j+1,f} &= \frac{m_j k_j}{m_{j+1}k_{j+1}}\left(E_{n,j,f}\sinh(\eta_n d_j) + F_{n,j,f}\cosh(\eta_n d_j)\right)\ ; j = 1,2,3,4, n \neq 0, m_j \neq 0 \end{aligned} \tag{2.47}$$

Note that for the epidermis layer, where $m_5 = 0$, the coefficients corresponding to $n = 0$ are given by,

$$\begin{aligned} E_{0,5,f} &= \left(\frac{k_4}{k_5}\right) m_4\left(E_{0,4,f}\sinh(m_4 d_4) + F_{0,4,f}\cosh(m_4 d_4)\right)\ ; n = 0, m_5 = 0 \\ F_{0,5,f} &= E_{0,4,f}\sinh(m_4 d_4) + F_{0,4,f}\cosh(m_4 d_4)\ ; n = 0, m_5 = 0 \end{aligned} \tag{2.48}$$

Similar to section 2.2.1, the coefficients $E_{n,1,f}$ are zero, whereas the coefficients $F_{n,1,f}$ could be chosen to be any constant are selected to be 1. The final step is to determine the series coefficients in equation (2.40), a procedure similar to section 2.2.1. On substituting equation (2.40) into equation (2.38) and then using orthogonality theorem, the series coefficients are obtained as,

$$D_0 = \frac{\int_{y=0}^{a} q_{sur}(y)dy}{k_5 E_{0,5,f}} \; ; n = 0$$

$$D_n = \frac{\int_{y=0}^{a} q_{sur}(y) Y_{n,j}(y)dy}{k_5 X'_{n,j,f}(b_5) N_y} \; \forall n \in Z^+ \tag{2.49}$$

Following a procedure similar to section for the $T_{j,s}(x,y)$ solution, the temperature solution for the governing equation represented by equation (2.39) for all homogeneous boundary conditions is given by,

$$T_{j,s}(x,y) = \sum_{n=0}^{\infty}\sum_{p=1}^{\infty} \frac{\sum_{j=1}^{5} \int_{y=0}^{a}\int_{x=b_{j-1}}^{b_j} k_j \left(\frac{\Phi_{j,s}(x,y) X_{p,j,s}(x)}{\gamma_p^2+\beta_n^2+m_j^2}\right) Y_{n,j,s}(y)dxdy}{N_x N_y} X_{p,j,s}(x) Y_{n,j,s}(y) \tag{2.50}$$

where, the norm integrals are similar to the integrals in equation (2.28, 2.29) and the source term is given by,

$$\Phi_{j,s}(x,y) = \frac{g_{met,j}}{k_j} + \delta_j \frac{g_{t,j}}{k_j} \tag{2.51}$$

The final temperature solution for the prescribed heat flux boundary condition at the surface of the skin tissue is given by the following expression,

$$T_j(x,y) = T_{bl} + \frac{\int_{y=0}^{a} q_{sur}(y)dy}{k_5 E_{0,5,f}} + \sum_{n=1}^{\infty} \frac{\int_{y=0}^{a} q_{sur}(y) Y_{n,j}(y)dy}{k_5 X'_{n,j,f}(b_5) N_y} X_{n,j,f}(b_5) Y_{n,j}(y)$$
$$+ \sum_{n=0}^{\infty}\sum_{p=1}^{\infty} \frac{\sum_{j=1}^{5} \int_{y=0}^{a}\int_{x=b_{j-1}}^{b_j} k_j \left(\frac{\Phi_{j,s}(x,y) X_{p,j,s}(x)}{\gamma_p^2+\beta_n^2+m_j^2}\right) Y_{n,j,s}(y)dxdy}{N_x N_y} X_{p,j,s}(x) Y_{n,j,s}(y) \tag{2.52}$$

2.2.3 Convective cooling at top of skin surface

The third scenario considered here involves convective cooling of the top surface of the skin tissue, resulting in a boundary condition of third kind,

$$-k_5 \frac{\partial T_5}{\partial x} = h(T(b_5, y) - T_\infty) \qquad \text{at} \qquad x = b_5 \tag{2.53}$$

A solution for this case may be derived using a procedure similar to section 2.2.1. The only departure from section 2.2.1 comes in the resistor network solution, shown in equation (2.16). In this case, $T_{j,r}(x)$ continues to be given by equation (2.16). However, due to the additional convective cooling term in the boundary condition at the top surface, the expression for Q in equation (2.17) must be modified as follows:

$$Q = \frac{T_\infty - T_{bl}}{\sum_{j=1}^{5} \frac{d_j}{k_j} + \frac{1}{h}} \tag{2.54}$$

where, $d_j = b_j - b_{j-1}$, j =1 to 5 and $b_0 = 0$. Thus, $T_{j,r}(x)$ is given by equations (2.16) where Q is replaced by equation (2.54). The rest of the solution continues to be similar to the solution previously derived for $T_{j,s}(x, y)$ in section 2.2.1. A detailed derivation of this case can also be found in [83].

Thus in this section an analytical solution for temperature distribution in a two-dimensional multilayer tissue is derived. The extension of the solution to a three dimensional case is quite straightforward, but more computationally intensive, due to the introduction of double summations and double integrals.

2.3 Results and Discussion

This section discusses temperature distribution in a five-layer skin tissue computed using the analytical models discussed in the previous section. These examples serve as tools to understand the fundamental behavior of the problem. Previously

reported thermophysical property data for various skin layers are used [40, 82]. Figure 2.2(a) shows a comparison between the theoretical solution and a finite element simulation. Temperature at the interface of papillary dermis and epidermis layer is compared. In this case, the temperature is prescribed to be 17° C at the top surface of the skin tissue. Note that in finite-element simulations, the m^2T term is modeled as a temperature-dependent volumetric heat sink. Grid refinement is carried out in order to ensure grid independence of the finite-element simulation results. There is good agreement between the two. Similar validation against finite-element simulations is shown in Figures 2.2(b) and 2.2(c) for constant heat flux and convective boundary conditions respectively at the top surface (sections 2.2.2 and 2.2.3 respectively). In Figure 2.2(b), 10 W/m^2 heat flux is prescribed, while in Figure 2.2(c), a heat transfer coefficient of 5 $W/m^2 - K$ is assumed with an ambient temperature of 17° C. The percentage error in peak temperature between the analytical and finite element solutions is found to be $\approx$ 4% from the blood physiological temperature of 37° C. However, one must note that the finite element simulation under predicts the temperature rise $\approx$ 14%. This error occurs both due to truncation of infinite series in the model, as well as due to discretization involved in the finite-element simulations. In addition to comparison with finite-element simulations, residuals for the governing equation and boundary conditions are computed and found to be very small for each case discussed in section 2.2.

Figures 2.3(a)-2.3(c) present contour plots of the entire tissue region for the three cases discussed in section 2.2. Same parameters as Figure 2.2 are used. A detailed representation of the layer containing the tumor is also shown for each case. These plots illustrate the temperature distribution in the cross section of tissue under study in the presence of a tumor. A parametric analysis is carried out to understand the effect of various geometric and bio-transport parameters, as well as boundary

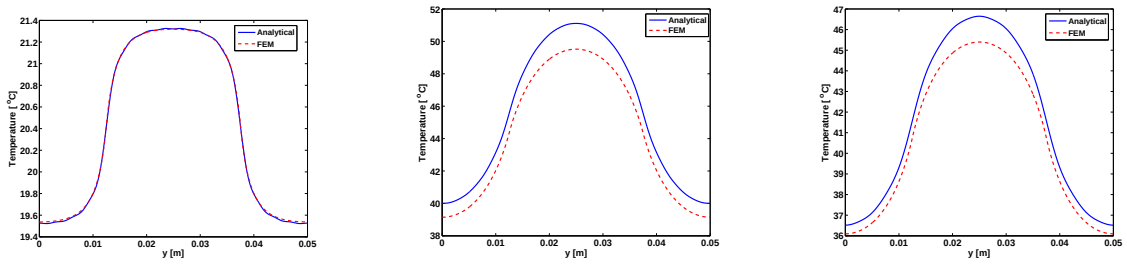

(a) (b) (c)

Figure 2.2. Temperature distribution along the interface of papillary dermis and epidermis layer computed using the analytical model, and comparison with finite-element simulations for (a) prescribed skin surface temperature (b) constant heat flux (c) convective heat transfer.

conditions on the temperature distribution in the multilayer structure. The effect of heat generation rate in the tumor is considered first. Figures 2.5(a)-2.5(c) show temperature plots at the interface of the papillary dermis and epidermis layer for different values of the volumetric heat generation rate in the tumor, while maintaining the tumor length at the half-length of the tissue. These figures correspond to the three boundary conditions discussed in section 2, using the same numerical values as Figures 2.2(a)-2.2(c). Volumetric heat generation rates, g_t (W/m^3) considered here are within the range of values reported in the past for magnetic nanoparticle based thermal therapies for cancer [36]. It is found, as expected, that the temperature at the interface increases within increasing volumetric heat generation strength. The peak temperature rise occurs along the region where the tumor is present, and tapers off outwards.

Figures 2.6(a)-2.6(c) plot the temperature distribution at the same location, as a function of the tumor length for constant total heating strength. These figures correspond to the three boundary conditions discussed in section 2.2. It is found that the temperature distribution widens and the peak temperature rise reduces as the size

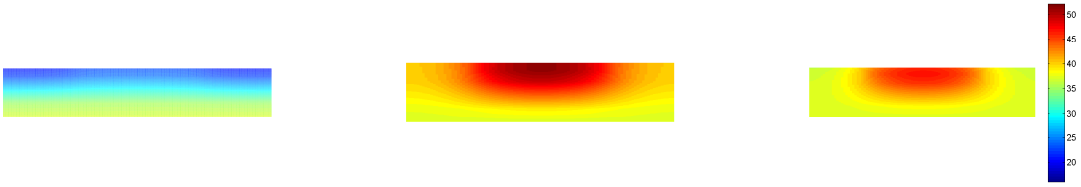

(a) (b) (c)

Figure 2.3. Contour plots of temperature distribution in a multilayer skin tissue for (a) prescribed skin surface temperature (b) constant heat flux (c) convective heat transfer boundary conditions.

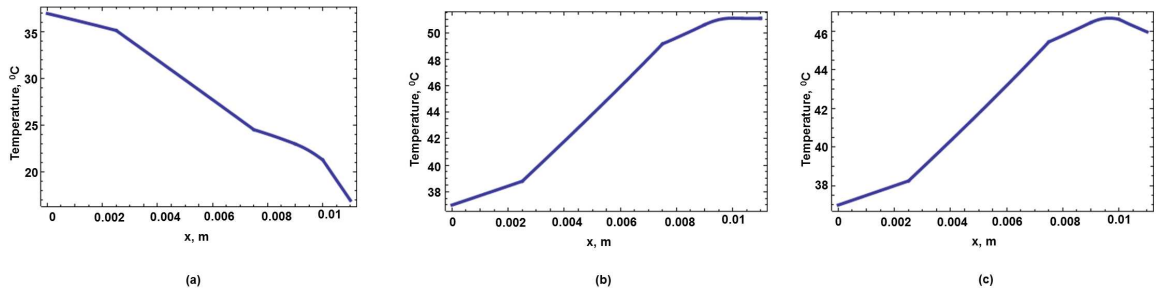

Figure 2.4. Temperature distribution along the centerline ($y = a/2$) for all layers as a function of x (a) prescribed skin surface temperature (b) constant heat flux (c) convective heat transfer boundary conditions.

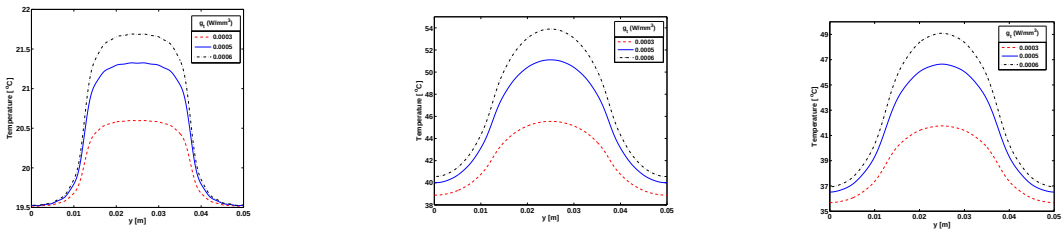

(a) (b) (c)

Figure 2.5. Temperature distribution at the interface between papillary dermis and epidermis layer as a function of volumetric heat generation rate in the tumor for (a) prescribed skin surface temperature (b) constant heat flux (c) convective heat transfer boundary conditions.

of the tumor increases. This occurs due to the reduced volumetric heat generation as the tumor size increases.

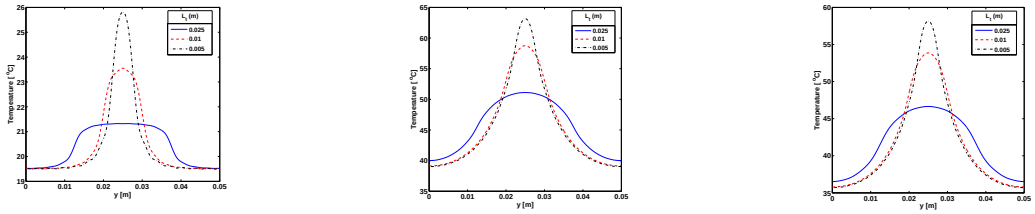

(a) (b) (c)

Figure 2.6. Temperature distribution at the interface between papillary dermis and epidermis layer as a function of tumor size for (a) prescribed skin surface temperature (b) constant heat flux (c) convective heat transfer boundary conditions.

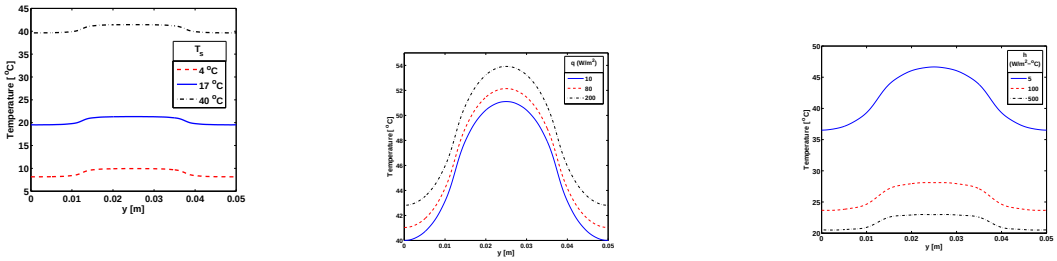

(a) (b) (c)

Figure 2.7. Temperature distribution at the interface between papillary dermis and epidermis layer as a function of the boundary condition for (a) prescribed skin surface temperature (b) constant heat flux (c) convective heat transfer boundary conditions.

Figure 2.7(a) plot the temperature distribution at the same location, as a function of the tumor length for constant total heating strength. These figures correspond to the three boundary conditions discussed in section 2.2. It is found that the temperature distribution widens and the peak temperature rise reduces as the size of the tumor increases. This occurs due to the reduced volumetric heat generation as the tumor size increases. presents the dependence of the temperature distribution on the top surface temperature for the boundary condition of the first kind. As the surface temperature at the top surface drops from 40° C to 4° C, a significant drop in the temperature profile at the top region of the tumor is observed. This is expected as a larger gradient is being created when the value of the surface temperature is reduced.

The analytical model presented in section 2.2 can accurately predict the temperature around the tumor for a constant temperature applied at the surface of skin tissue and can serve as a design tool for various heating or cooling scenarios for skin tissue. Figure 2.7(b) presents similar results for the boundary condition of the second kind. The tissue temperature increases with increase in the intensity of the applied heat flux. This may help in designing and regulating the heat intensity supplied by an external device during therapy. The effect of convective cooling on the top surface of skin is analyzed in Figure 2.7(c) using the derived analytical solution in section 2.2.3. As the value of the convective heat transfer coefficient increases, resulting in a shift from natural to forced convection, the temperature at the interface of papillary dermis and epidermis layer drops. Figures 2.7(a)-2.7(c) quantify the effect of external thermal interventions on the temperature distribution in the multilayer skin structure. Through the analytical derivation of the temperature distribution in the multilayer structure, these analyses may help the design of cooling devices for athletes [94] as well as thermal-based therapies for skin cancers.

CHAPTER 3

TRANSIENT TEMPERATURE IN MULTILAYER SKIN TISSUE

3.1 Introduction

Transient bioheat transfer involves temperature rise in biological systems during hyperthermia therapy. As seen from previous chapter, steady state heat transfer in multilayer tissue occurs due to several heat transfer modes such as conduction, advection and heat generation, wherein heat generation is commonly associated with the distribution of nanoparticles in the tumor and metabolism of the tissue. In this chapter, a transient model of the Pennes bioheat transfer equation is considered as the governing equation for the model. The main focus of this chapter is to illustrate the existence of both real and imaginary eigenvalues, their respective contribution to the temperature solution. The eigenvalues are functions of the blood perfusion rate and since the blood perfusion rate varies in different layers of multilayer tissue, special requirement in the mathematical model is necessary to obtain accurate temperature solutions. The model presented here includes a two layer skin tissue, cutaneous and subcutaneous layers. A two dimensional transient Pennes bioheat equation with the tumor heating source term being a function of both space and time is considered. The cross-section of tissue is subject to adiabatic boundary conditions on the side, constant wall temperature at the muscle core and convective cooling at the surface of the skin, see Figure 3.1.

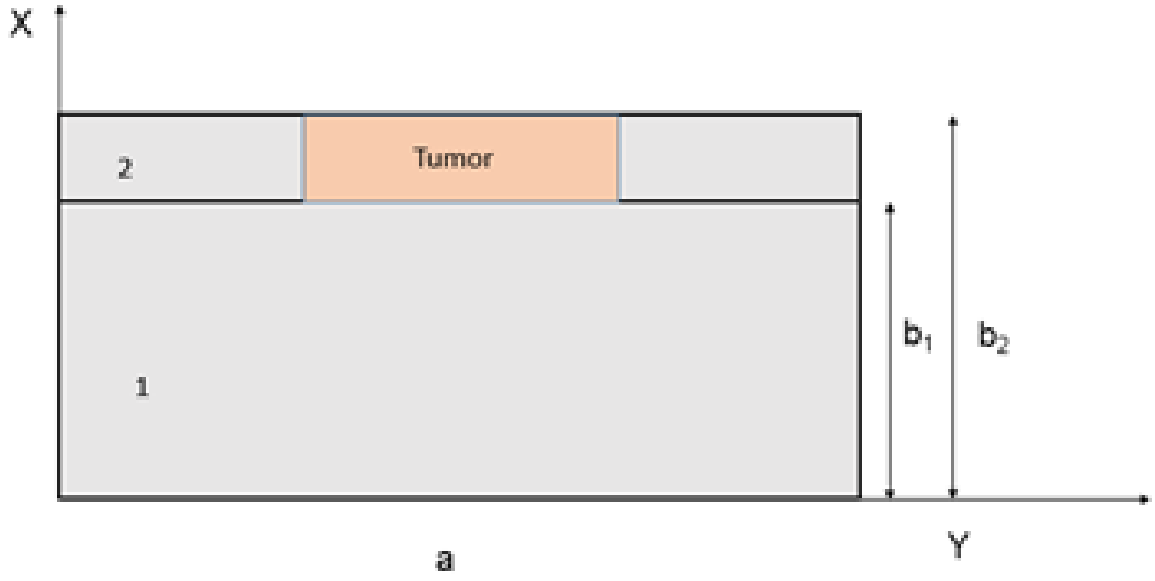

Figure 3.1. Two-layer skin tissue with tumor.

3.2 Mathematical Model

In this section the mathematical derivation of temperature distributions in a multilayer biological body is discussed. Consider the geometry of a two-layer skin tissue. Consider the presence of a tumor of a given size in the subcutaneous layer. Heat generation in the tumor, as well as boundary conditions of the top and bottom surfaces result in a temperature field in the multilayer tissue. In order to determine this temperature field analytically, the Pennes bioheat equation for each layer is solved, accounting for temperature and heat flux compatibility at the interfaces between adjacent layers. Solutions are derived using the classical separations of variables approach. The governing energy equation for each layer is given by:

$$\frac{\partial^2 T_j}{\partial x^2} + \frac{\partial^2 T_j}{\partial y^2} - m_j^2(T_j - T_{bl}) + \frac{g_{met,j}}{k_j} + \delta_j \frac{g_{t,j}(y,t)}{k_j} = \rho c \frac{\partial T_j}{\partial t} \tag{3.1}$$

where,

$$m_j^2 = \frac{(w_j \rho_b c_b)_{bl}}{(\rho c)_{tissue}} \tag{3.2}$$

In 3.1, $g_{met,j}$ refers to the volumetric heat generation inside a tissue due to metabolism. $g_{t,j}(y,t)$ refers to heat generation in the tumor due to thermal based therapy. The factor δ_j is introduced to determine the presence or absence of the tumor in the j^{th} layer. Other parameters such as w_j, ρ, c and k_j refer to blood perfusion rate, density of blood, specific heat of blood and thermal conductivity of tissue. $T_j(x,y)$ refers to the temperature rise above ambient at any spatial location inside the tissue. The core of the skin tissue is held at a constant temperature of 37° C, where T_{bl} in equation 3.3 corresponds the rise in core temperature above ambient, and side walls are assumed to be adiabatic.

Due to the multilayer nature of the problem, additional equations are obtained from compatibility at the interface between adjacent layers. Assuming perfect thermal contact,

$$T_j = T_{j+1} \qquad \text{at} \qquad x = b_j, \quad j = 1,2 \tag{3.3}$$

$$k_j \left(\frac{\partial T_j}{\partial x}\right) = k_{j+1} \left(\frac{\partial T_{j+1}}{\partial x}\right) \qquad \text{at} \qquad x = b_j, \quad j = 1,2 \tag{3.4}$$

The following initial condition and boundary conditions are considered here,

$$T_1 = T_{bl} \qquad \text{at} \qquad x = 0 \tag{3.5}$$

$$\frac{\partial T_j}{\partial y} = 0 \qquad \text{at} \qquad y = 0, a \tag{3.6}$$

$$T_j = T_{bl} \qquad \text{at} \qquad t = 0, \quad j = 1, 2 \tag{3.7}$$

$$k_2 \frac{\partial T_2}{\partial x} + h \ T_2(b_2, y) = 0 \qquad \text{at} \qquad x = b_2 \tag{3.8}$$

The solution to equations (3.1)-(3.9) can be obtained by the following superposition technique,

$$T_j(x, y) = T_{j,ss}(x) + T_{j,t}(x, y, t) \tag{3.9}$$

Substituting equation (3.10) in the equations (3.1)-(3.9) results in the following set of equations for $T_{j,ss}(x)$:

$$\frac{\partial^2 T_{j,ss}}{\partial x^2} = 0 \tag{3.10}$$

$$T_{1,ss} = T_{bl} \qquad \text{at} \qquad x = 0 \tag{3.11}$$

$$k_2 \frac{\partial T_2, ss}{\partial x} + h(T_{2,ss}(b_2, y)) = 0 \qquad \text{at} \qquad x = b_2 \tag{3.12}$$

Similarly the $T_{j,t}(x, y, t)$ problem is given by:

$$\frac{\partial^2 T_{j,t}}{\partial x^2} + \frac{\partial^2 T_{j,t}}{\partial y^2} - \left(\frac{m_j^2}{\alpha_j}\right) T_{j,t} + \Phi(x, y, t) = \frac{\partial T_{j,t}}{\partial t} \tag{3.13}$$

where

$$\Phi(x, y, t) = \frac{g_{met,j}}{k_j} + \delta_j \frac{g_{t,j}(y, t)}{k_j} + \left(\frac{m_j^2}{\alpha_j}\right) T_{bl} - \left(\frac{m_j^2}{\alpha_j}\right) T_{j,ss}(x) \tag{3.14}$$

subject to the following initial and boundary conditions,

$$T_{1,t} = 0 \qquad \text{at} \qquad x = 0 \tag{3.15}$$

$$k_2 \frac{\partial T_{2,t}}{\partial x} + h\ T_{2,t}(b_2, y) = 0 \qquad \text{at} \qquad x = b_2 \tag{3.16}$$

$$\frac{\partial T_{j,t}}{\partial y} = 0 \qquad \text{at} \qquad y = 0, a, \quad j = 1, 2 \tag{3.17}$$

$$T_{j,t} = T_{bl} - T_{j,ss}(x) = F(x) \qquad \text{at} \qquad t = 0, \quad j = 1, 2 \tag{3.18}$$

Note that both $T_{j,ss}\ (x)$ and $T_{j,t}\ (x, y, t)$ follow interface compatibility equations similar to equations (3.3) and (3.4). The solution for $T_{j,ss}(x)$, as seen in previous chapter is obtained using resistor network analogy [42] as follows:

$$T_{j,ss}(x) = T_{j-1,ss}(b_{j-1}) - Q\left(\frac{x - b_{j-1}}{a k_j}\right) \tag{3.19}$$

where,

$$Q = \frac{T_{bl}}{\sum_{j=1}^{2} \frac{d_j}{k_j}} \tag{3.20}$$

and $d_j = b_j\ -\ b_{j-1}$.

The solution for $T_{j,t}(x, y, t)$ is obtained using the method of separation of variables, starting with a general transformation,

$$T_{j,t}(x, y, t) = \sum_{n=1}^{\infty} \sum_{p=1}^{\infty} B_{np}(t) X_{i,n,p}(x) Y_n(y) e^{-(\lambda_{n,p}^2 + m_0^2)t} \tag{3.21}$$

In equation (3.21) the quantity m_0 is chosen to be a reference value which assumes the largest value between m_1 and m_2. Substituting equation (3.21) in the governing differential equation, equation (3.1) to obtain,

$$\sum_{n=1}^{\infty}\sum_{p=1}^{\infty}\left(X''_{j,np}(x)Y_n(y)+X_{j,np}(x)Y''_n(y)-\frac{m_j^2}{\alpha_j}X_{j,np}(x)Y_n(y)\right)B_{np}(t)e^{-(\lambda_{np}^2+m_0^2)t}$$
$$+\Phi(x,y,t)=\sum_{n=1}^{\infty}\sum_{p=1}^{\infty}\left(B'_{np}(t)-(\lambda_{np}^2+m_0^2)B_{np}(t)\right)X_{inp}(x)Y_n(y)e^{-(\lambda_{np}^2+m_0^2)t} \quad (3.22)$$

From equation 3.22, one can hypothesize the following ode's to determine the eigenvalues in X and Y co-ordinates,

$$\frac{X''_{1np}}{X_{1,np}}=-\gamma_{1,np}^2 \qquad \Longrightarrow\ X_{1np}=C_1\sin\left(\gamma_{1,np}\frac{x}{d_1}\right)+D_1\cos\left(\gamma_{1,np}\frac{x}{d_1}\right) \quad (3.23)$$

$$\frac{X''_{2,np}}{X_{2,np}}=-\gamma_{2,np}^2 \qquad \Longrightarrow\ X_{2,np}=C_2\sin\left(\gamma_{2,np}\frac{x-b_1}{d_1}\right)+D_2\cos\left(\gamma_{1,np}\frac{x-b_1}{d_1}\right) \quad (3.24)$$

$$\frac{Y''_n(y)}{Y_n(y)}=-\beta_n^2 \qquad \Longrightarrow\ Y_n(y)=\cos\left(\frac{\beta_n y}{a}\right), \quad \beta_n=(n-1)\pi \quad (3.25)$$

The constant, D_1, is determined using equation (3.15) and is zero. The value of the constant C_1 is arbitrarily chosen to be unity. The constants D_2 and C_2 are then determined using the contact conditions between the layers given by equations (3.3) and (3.4) respectively, a procedure adopted from [84, 89]. The only undetermined constant is the time dependent series coefficient, $B_{np}\ (t)$. Substituting equations (3.23) - (3.25) in equation (3.22) to obtain,

$$\sum_{n=1}^{\infty}\sum_{p=1}^{\infty}\left(-\frac{\gamma_{j,np}^2}{d_j^2}-\frac{\beta_n^2}{a^2}+\frac{\lambda_{n,p}^2}{\alpha_j^2}-\frac{m_0^2-m_j^2}{\alpha_j}\right)B_{np}(t)X_{i,np}(x)Y_n(y)$$
$$+\,\Phi(x,y,t)e^{(\lambda_{np}^2+m_0^2)t}=\sum_{n=1}^{\infty}\sum_{p=1}^{\infty}\frac{1}{\alpha_j}B'_{np}(t)X_{i,np}(x)Y_n(y) \quad (3.26)$$

The eigencondition is derived from the first term of the left hand side in equation (3.26) and is given by,

$$\gamma_{j,np}=d_i\ \sqrt{\frac{\lambda_{np}^2}{\alpha_j}+\frac{m_0^2-m_j^2}{\alpha_j}-\frac{\beta_n^2}{a^2}} \quad (3.27)$$

The eigenvalues, λ_{np} are then determined by substituting equation (3.24) in equation (3.16) using a second order Newton scheme. Equation (3.27) will result in imaginary values for $\gamma_{j,np}$ if $\beta_n^2 > a^2\ (\lambda_{np}^2+m_0^2-m_j^2)/\alpha_j$. In such a scenario the choice of a suitable starting value is essential to determine the eigenvalues. The starting value for λ_{np} for all n and p is given by $\lambda_{np}=(\beta_n/a)\ \alpha_0^{1/2}$, where is equal to the greater of and . Substituting equation (3.27) in equation (3.26) to obtain,

$$\sum_{n=1}^{\infty}\sum_{p=1}^{\infty}B'_{np}(t)X_{j,np}Y_n(y)=\frac{\alpha_j\Phi(x,y,t)}{k_j}e^{(\lambda_{np}^2+m_0^2)t} \quad (3.28)$$

From orthogonality principle [92, 95], applying to equation (3.28),

$$B'_{n,p}(t)=\sum_{j=1}^{2}\left(\frac{\int_{y=0}^{a}\int_{x=b_{j-1}}^{b_j}\Phi(x,y,t)X_{j,np}\,Y_n(y)\,dx\,dy}{\int_{x=b_{j-1}}^{b_j}(\rho c_p)_j\,X_{j,np}^2\,dx\int_{y=0}^{a}Y_n^2(y)\,dy}\right)e^{(\lambda_{np}^2+m_0^2)t} \quad (3.29)$$

The value of b_0 is zero in equation (3.29) as it represents the datum, see Figure 3.1. The coefficient $B_{np}(t)$ is then determined by integrating over time from 0 to t,

$$B_{np}(t) = A_{np} + \int_{\tau=0}^{t} \sum_{j=1}^{2} \left(\frac{\int_{y=0}^{a} \int_{x=b_{j-1}}^{b_j} \Phi(x,y,\tau) X_{j,np}(x)\, Y_n(y)\, dx\, dy}{\int_{x=b_{j-1}}^{b_j} (\rho c_p)_j\, X_{j,n,p}^2(x)\, dx \int_{y=0}^{a} Y_n^2(y)\, dy} \right) e^{(\lambda_{np}^2 + m_0^2)\tau}\, d\tau \tag{3.30}$$

where τ is a dummy variable of integration. Substituting equation (3.30) in equation (3.21) to obtain,

$$T_{j,t}(x,y,t) = \sum_{n=1}^{\infty} \sum_{p=1}^{\infty} \Bigg\{ A_{np} + \int_{\tau=0}^{t} \sum_{j=1}^{2} \frac{\int_{y=0}^{a} \int_{x=b_{j-1}}^{b_j} \Phi(x,y,\tau) X_{j,np}(x)\, Y_n(y)\, dx\, dy}{\int_{x=b_{j-1}}^{b_j} (\rho c_p)_j\, X_{j,n,p}^2(x)\, dx \int_{y=0}^{a} Y_n^2(y)\, dy} e^{(\lambda_{np}^2 + m_0^2)\tau} d\tau \Bigg\} X_{i,n,p}(x) Y_n(y) e^{-(\lambda_{n,p}^2 + m_0^2)t} \tag{3.31}$$

The above procedure obtains the values of series coefficient in the temperature solution, equation (3.21). The undetermined coefficient A_{np} is the constant of integration and can be obtained by applying orthogonality principle to equation (3.31) and using the initial condition given by equation (3.18),

$$A_{np} = \sum_{j=1}^{2} \frac{\int_{y=0}^{a} \int_{x=b_{j-1}}^{b_j} F(x) X_{j,np}(x)\, Y_n(y)\, dx\, dy}{\int_{x=b_{j-1}}^{b_j} (\rho c_p)_j\, X_{j,n,p}^2(x)\, dx \int_{y=0}^{a} Y_n^2(y)\, dy} \tag{3.32}$$

The final temperature solution is given by,

$$T_{j,t}(x,y,t) = \sum_{n=1}^{\infty}\sum_{p=1}^{\infty}\sum_{j=1}^{2}\left\{ \frac{\int_{y=0}^{a}\int_{x=b_{j-1}}^{b_j} F(x)X_{j,np}(x)\,Y_n(y)\,dx\,dy}{\int_{x=b_{j-1}}^{b_j}(\rho c_p)_j\,X^2_{j,n,p}(x)\,dx\int_{y=0}^{a}Y_n^2(y)\,dy} + \right.$$

$$\left. \int_{\tau=0}^{t} \frac{\int_{y=0}^{a}\int_{x=b_{j-1}}^{b_j}\Phi(x,y,\tau)X_{j,np}(x)\,Y_n(y)\,dx\,dy}{\int_{x=b_{j-1}}^{b_j}(\rho c_p)_j\,X^2_{j,n,p}(x)\,dx\int_{y=0}^{a}Y_n^2(y)\,dy} e^{(\lambda^2_{np}+m_0^2)\tau}\,d\tau \right\} X_{i,n,p}(x)Y_n(y)e^{-(\lambda^2_{n,p}+m_0^2)t} \tag{3.33}$$

where $F(x)$ is the effect of initial condition, equation (3.18) and $\Phi(x,y,t)$ is the contribution of the source term, equation (3.14) respectively.

3.3 Results and Discussion

This section will present the temperature distribution in multilayer perfused skin tissue subject to thermal therapy of cancer. The thermophysical properties of human skin are obtained from [16, 82] and are tabulated here.

Table 3.1. Themophysical properties of skin

Layer	Thermal conductivity $W/m-K$	Blood perfusion $m^3/s/m^3$	Heat generation W/m^3	Heat Capacity $J-kg/K$
Muscle	0.56	0.0005	684.2	3770
Dermal	0.37	0.0002	368.1	3400
Tumor	0.37	0.0002	500000	3400

Blood density = 1060 kg/m^3, Blood heat capacity = 3770 $J/kg-K$

Length of tissue = 5 cm, Muscle density = 1080 kg/m^3, Tumor density = 1200 kg/m^3

3.3.1 Skin cooling with skin surface temperature equal to blood temperature

In this example, the heat transfer coefficient, $h = 10\ W/m^2 - K$. Initially the tissue remains at the blood temperature, T_b for both layers. To illustrate the behavior of eigenvalues, in this example the skin surface temperature is assumed to be the same as the blood temperature, 37° C. This simplifies the problem with the transformation, $\Theta_j(x, y, t) = T_j(x, y, t) - T_b$, where $\Theta_j(x, y, t)$ here is the temperature rise anywhere in the tissue above blood temperature. Figure 3.2 illustrates the behavior of eigenvalues. Note the starting eigenvalue for the eigencondition from equation (3.16) varies. In order to compute the starting eigenvalue using a second order Newton scheme, equation (3.27) is necessary to satisfy the initial condition.

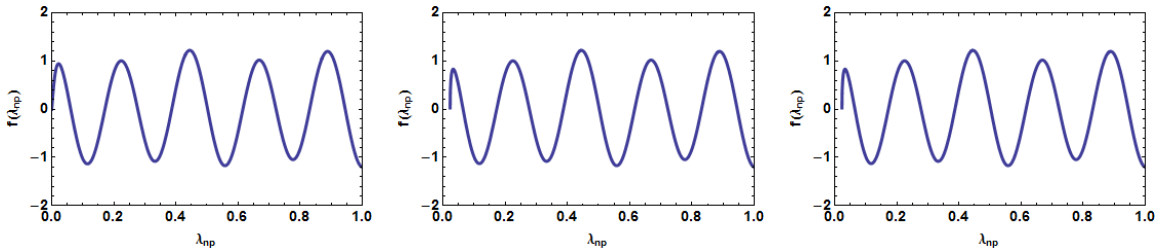

(a) (b) (c)

Figure 3.2. Eigenvalue plots for (a) $\beta = 0$ (b)$\beta = \pi$ (c) $\beta = 2\pi$.

Figure 3.3 illustrates a plot of temperature as function of time at the interface of two layers, $x = b_1, y = a/2$. From the figure steady state is observed to be reached around 800s. In figure 3.4 the transient temperature solution at time of 1400s is compared against the steady state solution. The steady state solution for the present problem is derived using the methodology in Chapter 2. A shot note on the derivation is presented at end of this chapter, see 3.4. Results indicate that the transient temperature solution agrees well with steady state temperature profile,

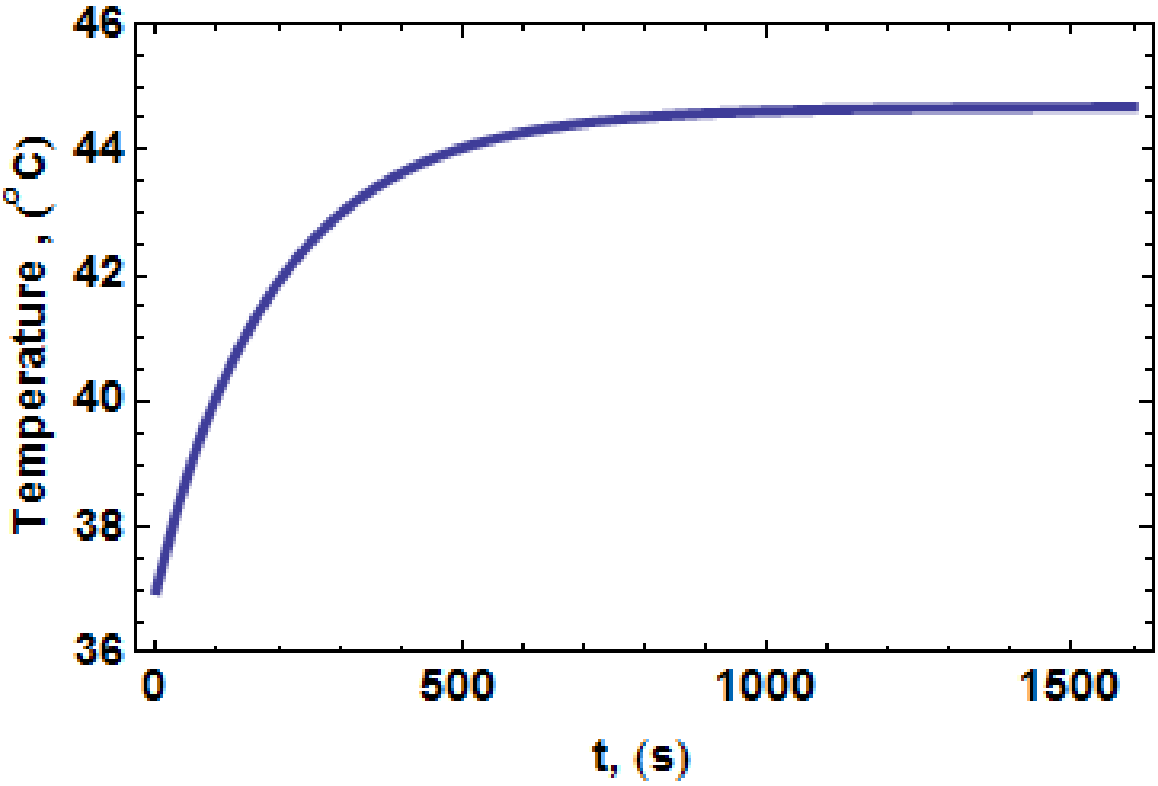

Figure 3.3. Temperature at the interface of the two layers, $x = b_1$ and $y = a/2$ with respect to time.

given by equation (3.38). This verifies the behavior of the transient model and 3.33 gives the temperature as a function of space and time in tissue during hyperthermia.

Figure 3.5 is an illustration of temperature distribution at the interface of the two layers and at time equals to $500s$ versus the length of tissue when a tumor with varying volumetric heat generation rate is considered while maintaining the same length for the tumor. As expected as the strength of the tumor increases the temperature in the tissue increases. Figure 3.6 presents the temperature distribution along the interface when the tumor volumetric strength is held constant at 0.000375 W/mm^3 for time equals to $500s$ while varying the length of the tumor section. As

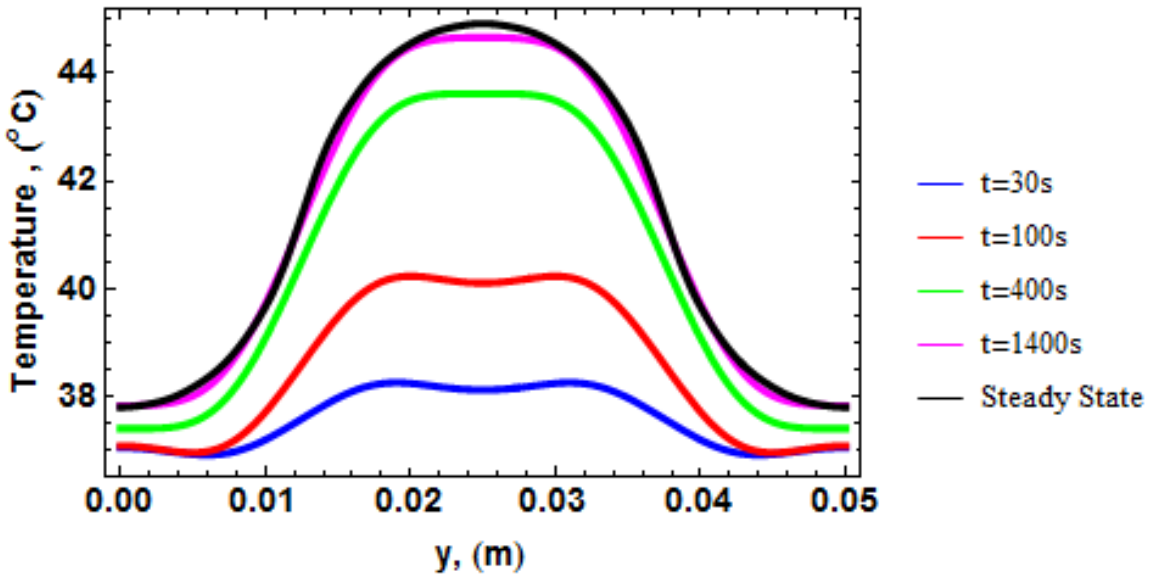

Figure 3.4. Temperature versus length of tissue at the interface of the two layers, $x = b_1$ for constant volumetric strength, $g_t = 0.0005\ W/mm^3$ and size of the tumor is maintained uniform at half the tissue length.

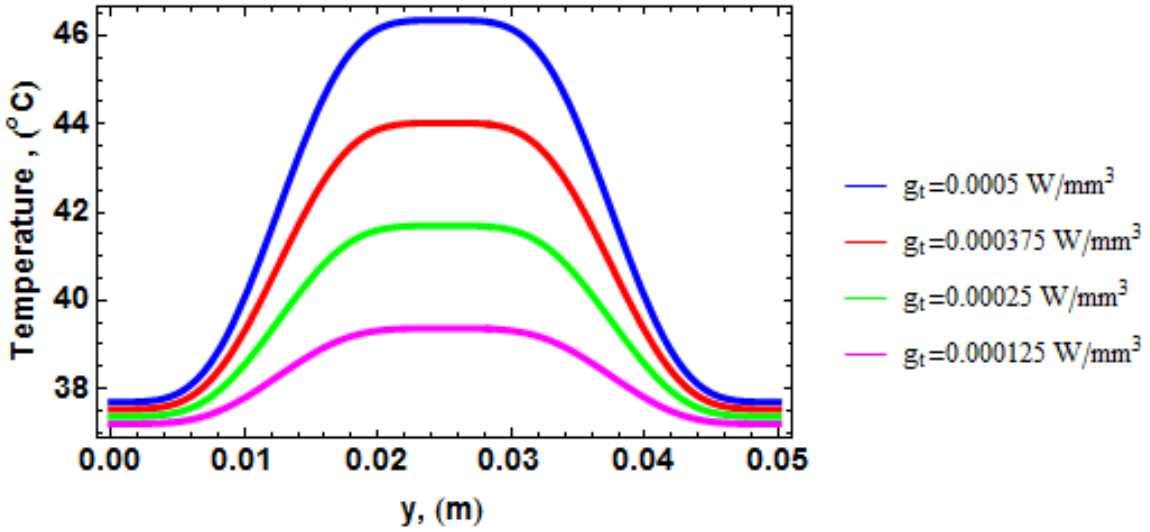

Figure 3.5. Temperature at the interface of two layers versus the length of tissue for $x = b_1$ and $t = 500s$ when the length of the tumor is maintained uniform and the volumetric strength is varied.

observed from the figure that a smaller size tumor causes less internal heat generation as compared to a larger tumor, which is along expected lines.

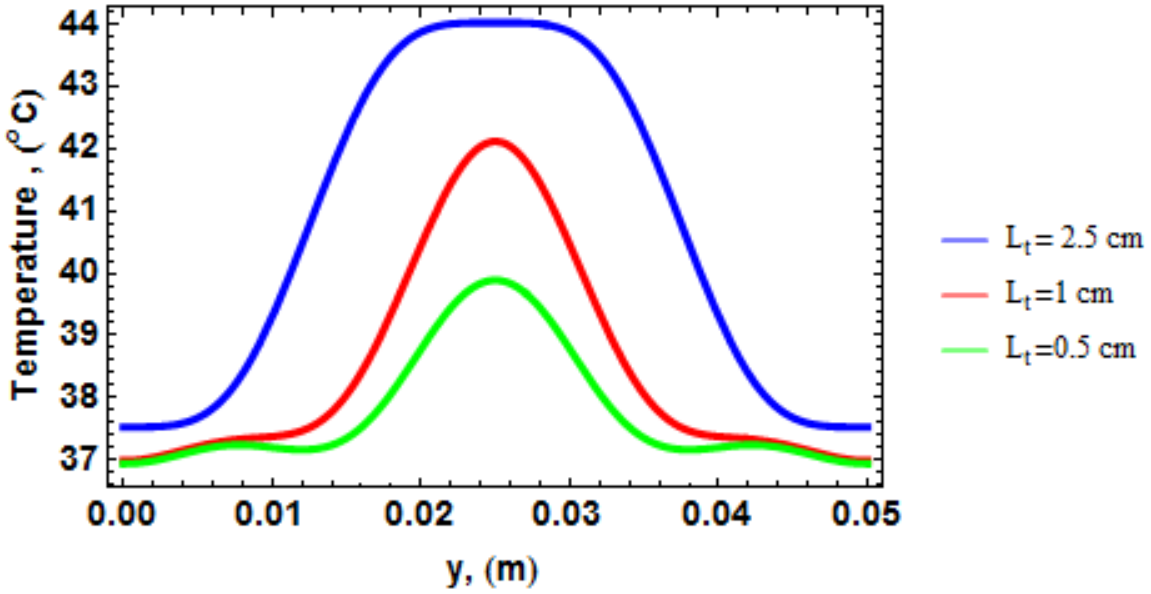

Figure 3.6. Temperature at the interface of two layers versus the length of tissue for $x = b_1$ and $t = 500s$ when the volumetric strength is kept uniform, $g_t = 0.000375$ W/mm^3 and the length of the tumor section is varied.

3.4 Appendix: Steady State Temperature Solution

The mathematical procedure adopted to derive the steady state temperature solution is obtained from [82, 83]. The governing equation is given by,

$$\frac{\partial^2 T_j}{\partial x^2} + \frac{\partial^2 T_j}{\partial y^2} - m_j^2(T_j - T_{bl}) + \frac{g_{met,j}}{k_j} + \delta_j \frac{g_{t,j}(y,t)}{k_j} = 0 \tag{3.34}$$

The interface and boundary conditions are similar to the transient problem discussed in section 3.2 by equations (3.3) - (3.8). The solution of respective ODEs after separating variables in X and Y-directions are given by,

$$\tilde{X}_{1,p}(x) = \sin(\gamma_p\ x) \tag{3.35}$$

$$\tilde{X}_{2,p}(x) = \sin(\gamma_p\ b_1)\ \cos(\gamma_p\ (x - b_1)) + \frac{k_1}{k_2}\ \cos(\gamma_p\ b_1)\ \sin(\gamma_p\ (x - b_1)) \tag{3.36}$$

$$\tilde{Y}_n(y) = \cos\left(\frac{n\pi y}{a}\right) \tag{3.37}$$

The final form of the steady state temperature solution is given by,

$$T_j(x,y) = \sum_{n=0}^{\infty}\sum_{p=1}^{\infty}\sum_{j=1}^{2} \frac{\int_{y=0}^{a}\int_{x=b_{j-1}}^{b_j} g_j(y)\tilde{X}_{j,p}(x)\tilde{Y}_n(y)dxdy}{\left(\gamma_p^2 + \beta_n^2 + m_j^2\right)\int_{x=b_{j-1}}^{b_j} k_j\tilde{X}_{j,p}^2(x)dx \int_{y=0}^{a}\tilde{Y}_n^2(y)dy}\tilde{X_{j,p}}(x)\ \tilde{Y}_n(y) \tag{3.38}$$

where $b_0 = 0$ and $g_j(y) = g_{met,j} + g_{t,j}(y)$.

CHAPTER 4

BIOHEAT TRANSFER WITH TUMOR OF ARBITRARY SHAPES DURING NANOPARTICLE BASED HYPERTHERMIA THERAPY

4.1 Introduction

Bioheat transfer for regular or orthogonal shaped tissue and tumor is discussed previously in chapters 2 and 3 of this dissertation. In most situations for one-dimensional isotropic diffusion problems an exact solution is possible [42, 92, 96]. In this chapter a general mathematical procedure for handling orthogonal and non-orthogonal shapes for tumor and tissue is presented. The mathematical procedure to develop the general solution to Pennes bioheat equation in this chapter uses the Galerkin based-integral method [97]. The Galerkin method in principle is very similar to the finite element method [98]. The major difference is finite element method includes a large set of elements of simple geometry, where the trial function is often a low-order polynomial. However, a higher order-polynomial approximation is possible using Galerkin method. In both methods, the linear combination of these trial functions is approximated to the real solution for the partial differential equation.

The range of the Galerkin method encompasses boundary value problems in heat conduction with homogeneous or non-homogeneous boundary conditions and governing equation. In addition to its application to diffusion problems in geometries involving arbitrary shape, the Galerkin method is well-suited for encompassing heterogeneity in the domain. This is important it helps us consider different thermal properties for the tumor and surrounding vasculature [96, 97]. For optimal planning of cancer therapy using nanoparticle mediated hyperthermia therapy, a general tem-

perature solution can help provide an accurate temperature distribution in diseased tissue associated with ablation therapies.

4.2 Mathematical model

The Pennes bioheat equation, 4.1, can be written in a generalized form

$$\nabla(k(\vec{r})\nabla T) + w_b(\vec{r},t)\rho_b(\vec{r})c_b(\vec{r})\ (T_b - T) + g_{met}(\vec{r},t) + g_{NP}(\vec{r},t) = \rho(\vec{r})c(\vec{r})\frac{\partial T}{\partial t} \quad (4.1)$$

where $T = T(\vec{r},t)$ is the temperature rise of the vasculature above ambient, $\vec{r}$ is the position vector and t is corresponding to time. The thermo-physical properties are space dependent thermal conductivity, $k(\vec{r})$, specific heat, $c_p(\vec{r})$ and density, $\rho(\vec{r})$. The index 'b' denotes blood thermo-physical properties and T_b corresponds to arterial temperature or core body temperature. For cases discussed in this chapter, the arterial temperature is held constant at the physiological temperature of 37° C.

Figure 4.1 illustrates the geometry of the problem considered in this chapter. The inclusion region marked in red denotes the tumor and rest is vascular tissue. The tissue and tumor thermal conductivity is found to vary [99].

The tissue as shown in Figure 4.1, represent the muscle or dermal region of skin tissue. A tumor of arbitrary shape, Γ_E represent the affected region of the tissue. In principle the thermal properties and blood perfusion in tumor domain (equation of curve, $\Gamma_E = 0$) can vary with respect to the tissue domain, Γ_M. The intersection of tumor and tissue domains, represent the vasculature diagnosed with tumor growth, Γ. In equation (4.1), the source terms g_{met} represent the metabolic heat generation rate of tissue and tumor and g_{NP} represent the volumetric heat generation inside tumor region due to nanoparticle distribution for laser or magnetic flux assisted hyperthermia therapy. The tissue sidewalls in the x-direction are assumed to be maintained

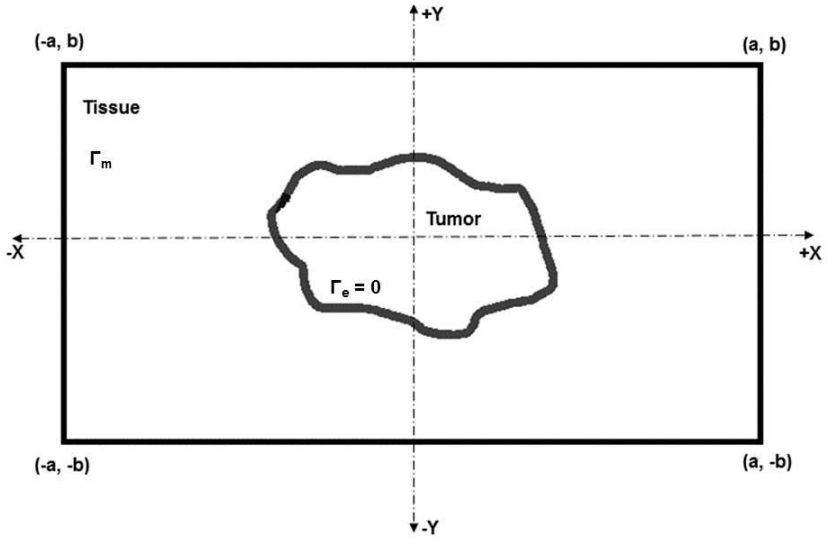

Figure 4.1. Tissue with arbitrary shape tumor.

at blood arterial temperature. In y-direction, convective boundary conditions with constant heat transfer coefficient are considered.

$$\frac{\partial T}{\partial x} = 0 \qquad \text{at } x = -a, a \tag{4.2}$$

$$\frac{\partial T}{\partial y} \pm \ hT = 0 \qquad \text{at } y = -b, b \tag{4.3}$$

Following the above discussion, this chapter will present a detailed mathematical procedure to obtain a general temperature field in the vasculature. To perform a transient analysis for the bioheat equation, the tissue and tumor are assumed to maintain the same initial conditions. The Galerkin method based on the principles of variational calculus, helps in capturing the physical effects associated with hyperthermia therapy in a less complicated technique as compared to alternate numerical

techniques for solving partial differential such as Finite Difference and Finite Volume methods [100]. However, the choice of method is independent to the problem discussed here and alternate techniques may serve equally well in providing accurate temperature solutions.

The tissue domain, Γ_M and tumor domain, Γ_E is considered to maintain perfect contact between them. This is expressed by,

$$(T_M)_{\Gamma_E=0} = (T_E)_{\Gamma_E=0} \tag{4.4}$$

$$k_M \left(\frac{\partial T_M}{\partial n}\right)_{\Gamma_E=0} = k_E \left(\frac{\partial T_E}{\partial n}\right)_{\Gamma_E=0} \tag{4.5}$$

Let equation (4.6) be a general temperature solution at any point in the vasculature,

$$T(\vec{r},t) = \sum_{n=1}^{N} P_n(t)\ \psi_n(\vec{r})\ e^{-\lambda_n t} \tag{4.6}$$

In equation (4.6), the coefficient $P_n(t)$ is to be determined. The undetermined coefficient will account for the contribution of the different source terms in equation (4.1). In the same equation, $\psi_n(\vec{r})$ and λ_n correspond to basis functions and eigenvalues respectively. A set of candidate basis functions can either be orthogonal functions such as *sine* or *cosine* or regular polynomials. The choice of special polynomials such as Chebyshev polynomials, the solution technique is very similar to spectral techniques [101]. Substituting equation (4.4) in equation (4.1) for every value of n results in,

$$\sum_{n=1}^{N} P_n(t)\left[\nabla(k(\vec{r})\nabla\psi_n(\vec{r}) - w_b(\vec{r},t)\rho_b(\vec{r})c_b(\vec{r})\ \psi_n(\vec{r}) + \lambda_n\rho(\vec{r})c(\vec{r})\ \psi_n(\vec{r})\right]e^{-\lambda_n t} + S(\vec{r},t) = \sum_{n=1}^{N}\rho(\vec{r})c(\vec{r})\psi_n(\vec{r})\frac{\partial P_n(t)}{\partial t} \quad (4.7)$$

where,

$$S(\vec{r},t) = g_{met}(\vec{r},t) + g_{NP}(\vec{r},t) + w_b(\vec{r},t)\rho_b(\vec{r})c_p(\vec{r})\ T_b \quad (4.8)$$

Based on the Galerkin-integral method, $\psi_n(\vec{r})$ is the eigenfunction which is given by a linear summation of polynomial, $f_j(\vec{r})$ also known as basis functions,

$$\psi_n(\vec{r}) = \sum_{n=1}^{N} d_{nj} f_j(\vec{r}) \quad (4.9)$$

Using equation (4.7), multiplying with f_i and integrating over the domain, Γ

$$\sum_{j=1}^{N} P_n(t)\ e^{-\lambda_n t}\int_\Gamma f_i\left[\nabla(k(\vec{r})\nabla\psi_n(\vec{r}) - w_b(\vec{r},t)\rho_b(\vec{r})c_b(\vec{r})\ \psi_n(\vec{r})\right.$$
$$\left.+\lambda_n\rho(\vec{r})c(\vec{r})\ \psi_n(\vec{r})\right]d\Gamma + \int_\Gamma f_i\ S(\vec{r},t)\ d\Gamma = \sum_{j=1}^{N}\frac{\partial P_n(t)}{\partial t}\ \int_\Gamma \rho(\vec{r})c(\vec{r})f_i\psi_n(\vec{r})d\Gamma \quad (4.10)$$

The first term in equation (4.10) constitutes the eigenvalue problem based on the Galerkin procedure found in [96, 97].

$$\int_\Gamma f_i\left[\nabla(k(\vec{r})\nabla\psi_n(\vec{r}) - w_b(\vec{r},t)\rho_b(\vec{r})c_b(\vec{r})\ \psi_n(\vec{r}) + \lambda_n\rho(\vec{r})c(\vec{r})\ \psi_n(\vec{r})\right]d\Gamma = 0 \quad (4.11)$$

In matrix form, the eigenvalue problem for the homogeneous governing bioheat equation is represented as,

$$(\boldsymbol{A} + \lambda_n\boldsymbol{B})\boldsymbol{d}_n = 0 \quad (4.12)$$

where elements of square matrices $\boldsymbol{A}$ and $\boldsymbol{B}$ of size N are given by,

$$a_{ij} = \int_{\Gamma} f_i \left[\nabla(k(\vec{r})\nabla f_j - w_b(\vec{r},t)\rho_b(\vec{r})c_b(\vec{r})\ f_j\right]\ d\Gamma$$

$$b_{ij} = \int_{\Gamma} f_i\ \rho(\vec{r})c(\vec{r})\ f_j\ d\Gamma \tag{4.13}$$

Subsequently, rest of the procedure in obtaining the coefficients $P_n(t)$ is very similar to the mathematical procedure adopted in Chapter 3. In addition, detailed procedure on obtaining final temperature solution is presented in [96,102]. Therefore, the expression for final temperature solution is given by,

$$T(\vec{r},t) = \sum_{n=1}^{N}\sum_{m=1}^{N} p_{nm}\ \psi_n(\vec{r}) \left[\int_{\Gamma} \rho(\vec{r})c(\vec{r})F(\vec{r})f_m(\vec{r})\ d\Gamma\ e^{-\lambda_n t} + \int_{\tau=0}^{t}\int_{\Gamma} e^{-\lambda_n(t-\tau)}S(\vec{r},\tau)f_m(\vec{r})\ d\Gamma\ d\tau\right] \tag{4.14}$$

where, $F(\vec{r}) = T_b - T_\infty$, represent the initial condition. The coefficient p_{nm} is given by $[(\boldsymbol{DB})^T]^{-1}$ and square matrix $\boldsymbol{D}$ of size N is composed of the eigenvectors $(\boldsymbol{d}_n)^T$.

4.3 Basis function for heterogeneous vasculature

In this section a procedure to obtain basis function for heterogeneous bodies will be discussed in brief. For detailed section on the methodology please see [96,102,103]. For this section only, the boundary at $y = \pm b$ of the vascular domain, Γ is assumed to be maintained at uniform blood arterial temperature, T_b. Equation (4.3) is replaced by the following equation (4.15) and since T represents the temperature rise, we obtain,

$$T = 0 \qquad \text{at } y = \pm b \tag{4.15}$$

The sidewalls along X-axis are assumed to be sufficiently long to consider adiabatic boundary conditions, equation (4.2). Hence we can start with the assumption that basis function in variable y is a polynomial of j^{th} order as given by,

$$f_j(y) = (c_1 + c_2 y^2)\ y^{(2j-2)} \tag{4.16}$$

Using any one condition given by equation (4.15), a relationship between the two constants c_1 and c_2 can be obtained. Finally, the basis function for prescribed vascular wall temperature is given by,

$$f_j(y) = (b^2 - y^2)\ y^{(2j-2)} \tag{4.17}$$

Using similar procedure, the basis for adiabatic vascular walls in x-direction is given by,

$$f_i(x) = (a^2 i - (i-1)x^2)\ x^{(2i-2)} \tag{4.18}$$

The basis function for the inclusion is obtained from [103]

$$f_{ij,e} = f_{ij,m} + U + \Gamma_E H \qquad \text{for } i = 1, 2, \ldots N;\ j = 1, 2, \ldots N \tag{4.19}$$

where $f_{ij,e}$ is the basis function of the inclusion, $f_{ij,m}$ is the basis function for the main domain which in this case is given by the product of equations (4.17) and (4.18). The expressions for parameters U and H are as follows,

$$U = -\frac{k_m}{C}\left(\frac{\partial f_{ij,m}}{\partial n}\right)_{\Gamma_E=0} \tag{4.20}$$

$$H = \frac{(\nabla f_{ij,m} \cdot \nabla\Gamma_E)_{\Gamma_E=0}\ (k_m/k_e - 1) - \nabla U \cdot (\nabla\Gamma_E)_{\Gamma_E=0}}{(\nabla\Gamma_E \cdot \nabla\Gamma_E)_{\Gamma_E=0}} \tag{4.21}$$

In equation (4.20), C stands for contact conductance which in the present analysis is infinite since perfect contact is assumed between tumor wall and surrounding tissue in the vasculature. Hence, as $C \to \infty$, $U \to 0$ and hence equations (4.4) and (4.5) are satisfied. The parameters, k_m and k_e represent the thermal conductivities of tissue and tumor region respectively.

4.4 Results and Discussion

A simple test case is considered to analyze the temperature solution, equation (4.14) derived in section 4.2. The top and bottom vascular sidewalls at $y = \pm b$ are maintained at the blood arterial temperature, $T_b = 37^\circ$ C. The sidewalls of vascular tissue, $x = \pm a$ are considered to be long such that the boundary does not affect the temperature solution. Hence an adiabatic boundary condition is considered. The effective skin tissue thermal conductivity, k_m is found to be in range $0.3-0.6W/m-K$ for normal flow to enhanced flow conditions [99]. In the present analysis the value of tissue thermal conductivity is considered to be $k_m = 0.4W/m-K$ and tumor thermal conductivity to be $k_e = 0.6W/m-K$. A square domain of size $1cm \times 1cm$ represents the vascular region affected by tumor growth. All other tissue and tumor properties for examples presented in this section can be obtained from 3.1.

Figure 4.2 illustrates the temperature plot as a function of x at $y = 0$. The heat generation due to metabolism in tissue and tumor is equal to 368 W/m^3. In the tumor domain, Γ_E the heat generation due nanoparticle distribution for hyperthermia therapy is assumed to be equal to 250000 W/m^3 [36]. The aspect ratio of the ellipse is 5:1 with the half major axis equal to 5 mm and half minor axis equal to 1 mm. From results, considering 21 polynomial trial functions is sufficient for convergence in the temperature solution.

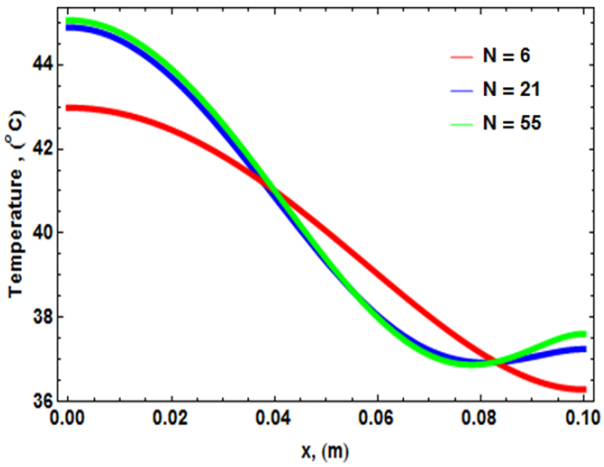

Figure 4.2. Temperature plot for verifying convergence of solution of and elliptical shape tumor for $N = 6$, $N = 21$ and $N = 55$, where N is the number of terms in series.

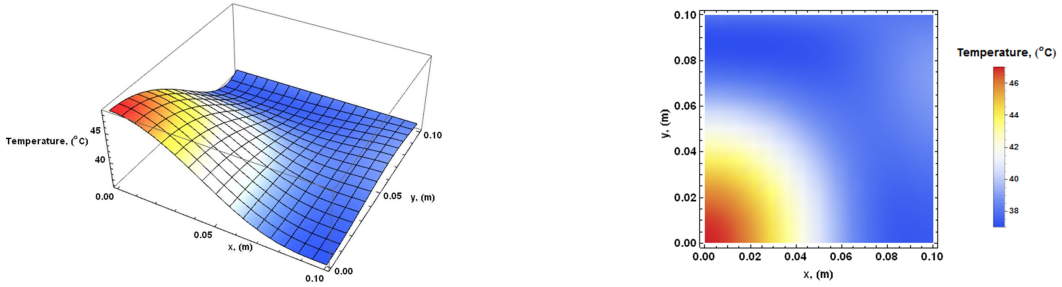

(a) (b)

Figure 4.3. Temperature distribution for nanoparticle based hyperthermia at time, $t = 10$ mins for a tumor of circular shape, radius $= 5mm$ (a) 3-D temperature distribution, $g_{NP} = 150000\ W/m^3$ (b) Contour plot for temperature as function of x and y.

Figures 4.3(a) and 4.3(b) illustrate the temperature distribution in vascular tissue in presence of transient hyperthermia therapy. Figure 4.3(a) illustrates a quarter of the entire vascular region as shown in Figure 4.1. Blood perfusion rate through

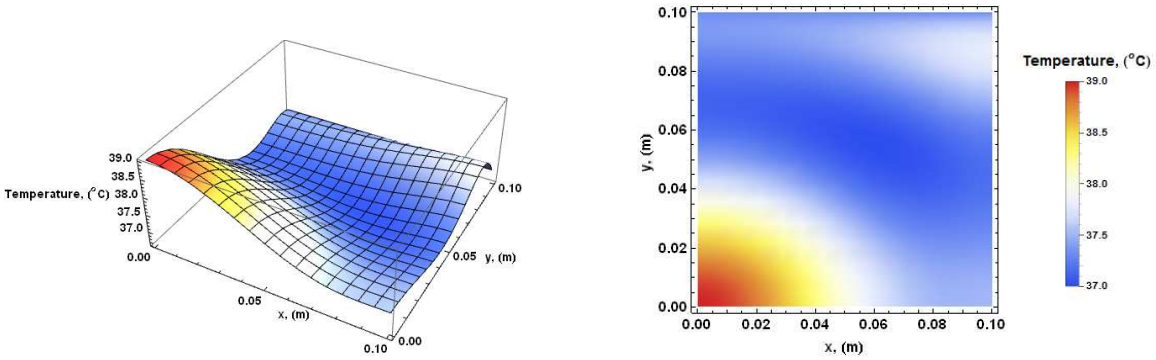

(a) (b)

Figure 4.4. Temperature distribution for nanoparticle based hyperthermia at time, $t = 10$ mins for a tumor of elliptical shape (a) 3-D temperature distribution, $g_{NP} = 250000W/m^3$ (b) Contour plot for temperature as function of x and y.

the tumor is assumed same as the tissue. However, in the temperature solution given by equation (4.14) different blood perfusion rates in the tissue and tumor region can be easily handled. The source term in the Pennes bioheat equation representing heat generated due to nanoparticles for this case is equal to $g_{NP} = 150000W/m^3$.

This is important because in principle, malignant tumor cells obtain nutrients from newer blood vessels that originate from existing blood vessels through signal exchange of growth factors such as vascular endothelial growth factor (VEGF). The newer blood vessels that are formed as the tumor grows in size are leaky with pore size ranging in tens of microns [104]. Nanoparticle assisted hyperthermia therapy, utilizes functionalized nanoparticles, nanoshells that travel through the blood vessels and through the pores into the tumor region. Once in the diagnosed region, the nanoparticles are excited using external sources such as laser beam or an alternating magnetic field to elevate the temperature of that region. It has been observed that elevating the temperature of malignant tumor cells increases their susceptibility to subsequent radiation or chemotherapy treatments [105].

A similar analysis for an elliptical shape tumor with half major axis equal to 5 mm and half minor axis equal to 1 mm is illustrated as Figure 4.4. The only variation from Figure 4.3 is the heat generated due to nanoparticles for this case is equal to $g_{NP} = 250000 W/m^3$. The variation in value is due to the different equations of tumor domain, $\Gamma_E = 0$ in an attempt to maintain the maximum temperature around 43° C.

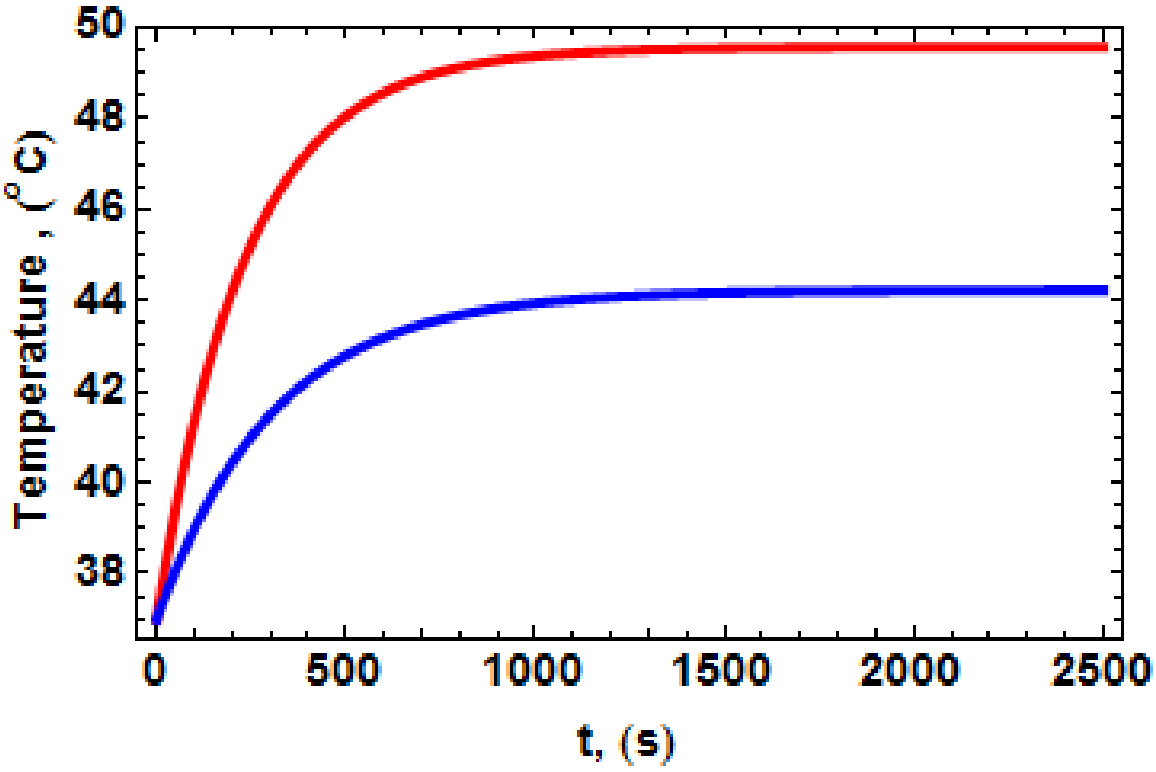

Figure 4.5. Temperature as a function of time at the core of the tumor for circular shape tumor (red) and elliptical shape tumor (blue).

Figure 4.5, represents the core temperature of the tumor as a function of time. As seen from the figure, the circular tumor, (shown in red) being larger in size than the elliptical tumor, (shown in blue) produces more heat for a given distribution of nanoparticle volumetric heating. The nanoparticle concentration is proportional to the heat generation in the tumor volume or the specific absorption rate (SAR).

In principle, the SAR expression is a distribution over a given space and varies with time. Hence, consideration of this has been provided in the general temperature solution, where the source term $S(\vec{r}, t)$ given by equation 4.8, is integrated over the vascular domain Γ over the time planned for the therapy. Therefore, one can use the methodology presented in this chapter to either determine the temperature anywhere in diseased tissue or use the temperature distribution obtained from equation 4.14 to accurately estimate the value for SAR, thereby the nanofluid concentration to be delivered at the tumor, in order to avoid overheating of healthy tissue in the case of hyperthermia.

Alternately, one can apply the mathematical procedure in 4.2 to solve problems related to cryo-therapy and cryo-cooling [106] where the heat transfer coefficient is known to vary. Physical models both living and engineered are often subject to variable heat transfer conditions such as cryoneedle used in treatment of prostate cancer [107], jet impingement using a cryogun are common in practice. The next few chapters of this dissertation will address this fundamental heat transfer model using a simple mathematical model.

CHAPTER 5

TEMPERATURE INSIDE AN ORTHOTROPIC CYLINDER SUBJECT TO VARYING HEAT TRANSFER

5.1 Introduction

Convective heat transfer of a cylinder in cross-flow is a classical boundary layer problem and have been addressed both using theoretical models based on mass, momentum and energy conservation of fluid leading to boundary layer theory and from experimental measurements [43]. Although the fluid velocity and temperature has continuously been characterized, not sufficient models exist which analyze the temperature inside a heat generating orthotropic cylinder subject to such spatially varying flows. In this chapter, an analytical method is developed to compute the temperature profile within an infinite and a finite cylinder subject to internal heat generation and varying convective heat transfer coefficient at the outer surface . The analytical model results in a series solution for the temperature profile with coefficients that can be computed easily by solving a well-defined set of linear algebraic equations. Using the functional form of $h(\theta)$ from well-known experiments, [42,43], the expected temperature profile is computed inside a cylinder subject to an external coolant flow. The dependence of the temperature profile on a number of parameters such as the Reynolds number of the external flow, extent of thermal conduction anisotropy, aspect ratio, etc. is discussed. In addition to addressing a classical theoretical problem, this chapter may also help develop design tools for thermal management of Li-ion cells using external coolant flow.

5.2 Mathematical Model

A steady state thermal conduction problem in two and three dimensional cylindrical systems is considered here. A cylinder of radius R and uniform internal heat generation is subject to circumferentially varying heat transfer represented by $h(\theta)$. Note that $h(\theta)$ must be an even function and periodic with a period of 2π. Two specific cases shown in Figure 5.1 are considered an infinitely long cylinder, and a finite cylinder of height H. The finite cylinder is subjected to a constant convective heat transfer coefficient h end at the top and bottom surfaces. Thermal conduction within the cylinder is assumed to be orthotropic, with the radial, circumferential and axial thermal conductivities given by k_r, k_θ and k_z respectively.

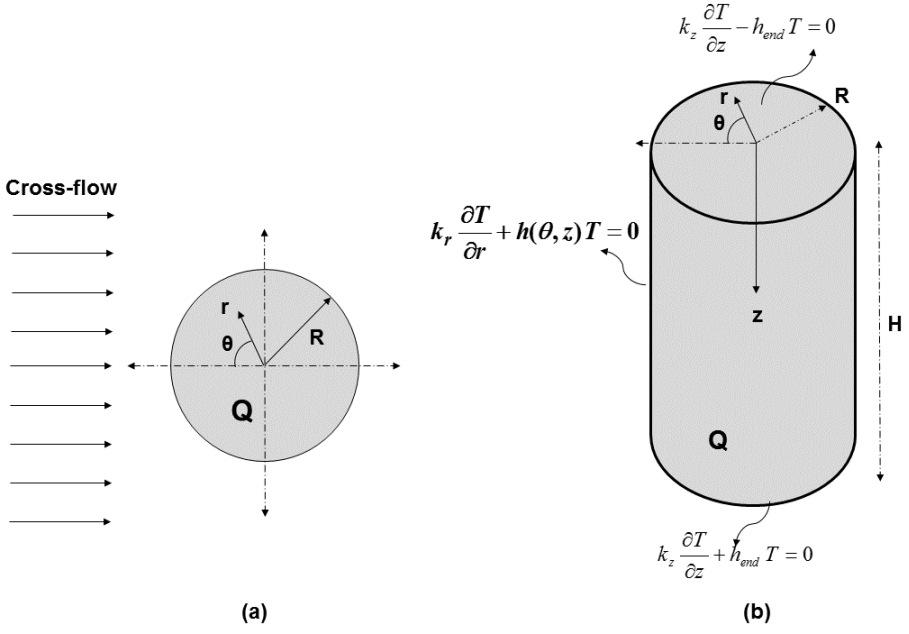

Figure 5.1. Schematic of the geometry under consideration for (a) infinite, and (b) finite cylinder subjected to circumferentially varying convection at the surface due to cross-flow.

Such anisotropy in thermal conduction, occurs in a Lithium-ion battery. Recent experimental measurements have indicated a 100− fold difference in the axial and radial thermal conductivities [2]. The following sections will present a detailed derivation of temperature solution in infinite and finite length cylinders when subject to varying heat transfer.

5.2.1 Infinite cylinder

The governing equation is given by,

$$\frac{k_r}{r}\,\frac{\partial}{\partial r}\,\left(r\frac{\partial T}{\partial r}\right)+\frac{k_\theta}{r^2}\,\frac{\partial^2 T}{\partial \theta^2}+g=0 \tag{5.1}$$

where $T(r,\theta)$ is the temperature rise above ambient. The problem is subject to the following boundary conditions:

$$T<\infty,\ \text{bounded and finite},\ \frac{\partial T}{\partial r}=0 \qquad \text{at} \qquad r=0 \tag{5.2}$$

$$k_r\,\frac{\partial T}{\partial r}+h(\theta)\,T=0 \qquad \text{at} \qquad r=R \tag{5.3}$$

$$T(\theta)=T(\theta+2\pi) \tag{5.4}$$

$$\left(\frac{\partial T}{\partial \theta}\right)_{\theta=0}=\left(\frac{\partial T}{\partial \theta}\right)_{\theta+2\pi} \tag{5.5}$$

Equation (5.2) requires the core temperature to be bounded. In other words, heat cannot move towards the core of the solid cylinder due to forced, spatially-varying convective cooling outside and thus the temperature of the core must remain

finite. Equation (5.3) illustrated accounts for Newton cooling at the cylinder external surface and introduces the spatial variation in heat transfer, $h(\theta)$. Equations (5.4) and (5.5) represent temperature and periodicity in the circumferential direction.

Equations (5.1) - (5.5) , represent a thermal conduction problem in which the governing energy equation is non-homogeneous, whereas all boundary conditions are homogeneous. If the convective heat transfer coefficient in equation. (5.3) were to be constant, this set of equations admits a straightforward solution using the separation of variables approach. However, h-dependence of h precludes this approach. Instead, a more general approach that accounts for h-dependence of h must be adopted. The temperature field is first split into two parts as follows:

$$T(r,\theta) = w(r,\theta) - \frac{gr^2}{4k_r} \tag{5.6}$$

Subsequently the $w(r,\theta)$ results into a homogeneous governing equation and with one non-homogeneous boundary condition. The following set of equations are obtained for the $w(r,\theta)$ problem,

$$\frac{k_r}{r}\,\frac{\partial}{\partial r}\left(r\frac{\partial w}{\partial r}\right) + \frac{k_\theta}{r^2}\,\frac{\partial^2 w}{\partial \theta^2} = 0 \tag{5.7}$$

subject to

$$w < \infty, \text{ bounded and finite}, \frac{\partial w}{\partial r} = 0 \qquad \text{at} \qquad r = 0 \tag{5.8}$$

$$k_r\,\frac{\partial w}{\partial r} + h(\theta)\,w = F(\theta) \qquad \text{at} \qquad r = R \tag{5.9}$$

$$w(\theta) = w(\theta + 2\pi) \tag{5.10}$$

$$\left(\frac{\partial w}{\partial \theta}\right)_{\theta=0} = \left(\frac{\partial w}{\partial \theta}\right)_{\theta+2\pi} \tag{5.11}$$

where

$$F(\theta) = \frac{gR}{2}\ \left(1 + \frac{h(\theta)R}{2k_r}\right) \tag{5.12}$$

The solution for $w(r,\theta)$ is expressed in terms of an infinite series as follows:

$$w(r,\theta) = \sum_{m=0}^{\infty} C_m\ cos(m\theta)\ \left(\frac{r}{R}\right)^{m\ \sqrt{k_\theta/k_r}} \tag{5.13}$$

Equation (5.13) satisfies the governing equation given by equation (5.7) along with three boundary conditions, equations (5.8), (5.10) and (5.11). The unknown coefficients, C_m can be determined using equation (5.9). This would require substituting equation (5.13) in equation (5.9) to get,

$$k_r\ \sum_{m=0}^{\infty} C_m cos(m\theta)\frac{m\sqrt{k_\theta/k_r}}{R} + h(\theta)\ \sum_{m=0}^{\infty} C_m\ cos(m\theta) = F(\theta) \tag{5.14}$$

Finally, equation (5.14) is is multiplied by $cos(j\theta)$ and integrated from $\theta = 0$ to $\theta = 2\pi$. Because h is a function of θ, this results in a set of linear equations involving the unknown coefficients:

$$C_j b_j + \sum_{m=0}^{\infty} C_m\ d_{jm} = f_j \qquad\qquad j = 0, 1, 2, ..., \tag{5.15}$$

where

$$b_j = \frac{j\sqrt{k_r k_\theta}}{R} \int_{\theta=0}^{2\pi} cos^2 j\theta\ d\theta \tag{5.16}$$

$$d_{jm} = \int_{\theta=0}^{2\pi} h(\theta) \cos j\theta \cos m\theta \; d\theta \tag{5.17}$$

$$f_j = \int_{\theta=0}^{2\pi} F(\theta) \cos j\theta \; d\theta \tag{5.18}$$

Assuming that the maximum value of m in equation (5.14) is M, equation (5.15) represents a set of $(M+1)$ linear equations in $(M+1)$ unknowns $C_j, j = 0, 1, 2, ..., M$, from where the unknown coefficients can be computed. Once the coefficients are computed, equations (5.6) and (5.13) represent the temperature distribution in the anisotropic cylinder. Putting $k_r = k_\theta$ in equations above reduces the solution to that for an isotropic cylinder with identical thermal conductivity in each direction. It is to be noted that in the special case of h being independent of θ, d_{jm} become zero except when $j = m$. As a result, equation (5.15) reduces to $(b_j + d_j j)C_j = f_j$, from where all $C_j s$ can be obtained explicitly without the need to solve a set of algebraic equations. This corresponds to the separation of variables approach for constant heat transfer boundary conditions, in which all coefficients can be obtained explicitly, as opposed to the case considered here, where the coefficients are determined through the solution of a set of linear algebraic equations.

5.2.2 Finite cylinder of height H

This sub-section considers a finite cylinder of height H. In this case, the governing energy equation is given by

$$\frac{k_r}{r} \frac{\partial}{\partial r} \left(r \frac{\partial T}{\partial r} \right) + \frac{k_\theta}{r^2} \frac{\partial^2 T}{\partial \theta^2} + k_z \frac{\partial^2 T}{\partial z^2} + g = 0 \tag{5.19}$$

The temperature field $T(r, \theta, z)$ satisfies the boundary conditions given by equations (5.2)(5.5). Note that the convective heat transfer coefficient in equation (5.3) is

now a function of h as well as z, i.e. $h = h(\theta, z)$. The temperature field also satisfies the following boundary conditions in the z direction:

$$k_z \frac{\partial T}{\partial z} - h_{end} T = 0 \qquad \text{at} \qquad z = 0 \tag{5.20}$$

$$k_z \frac{\partial T}{\partial z} + h_{end} T = 0 \qquad \text{at} \qquad z = H \tag{5.21}$$

In this case, the solution methodology is similar to that described for the infinite cylinder in Section 5.2.1. The temperature solution is given by,

$$T(r, \theta, z) = w(r, \theta, z) + f(z) \tag{5.22}$$

where $f(z)$ can be expressed by an exact solution expressed as,

$$f(z) = \frac{QH^2}{2k_z} \left(\frac{z}{H} \left(1 - \frac{z}{H}\right) + \frac{1}{Bi} \right) \tag{5.23}$$

and $Bi = h_{end} H / k_Z$.

Substituting equation (5.22) in equation (5.19) to obtain the set of equations for $w(r, \theta, z)$:

$$\frac{k_r}{r} \frac{\partial}{\partial r} \left(r \frac{\partial w}{\partial r} \right) + \frac{k_\theta}{r^2} \frac{\partial^2 w}{\partial \theta^2} + k_z \frac{\partial^2 w}{\partial z^2} + g = 0 \tag{5.24}$$

The functional form for $w(r, \theta, z)$ satisfies the boundary conditions given by equations equations (5.8), (5.10) and (5.11). In addition, w also satisfies

$$k_z \frac{\partial w}{\partial z} - h_{end} w = 0 \qquad \text{at} \qquad z = 0 \tag{5.25}$$

$$k_z \frac{\partial w}{\partial z} + h_{end} w = 0 \qquad \text{at} \qquad z = H \tag{5.26}$$

and

$$-k_r \left(\frac{\partial w}{\partial r} \right)_{r=R} = h(\theta, z)(w + f(z)) \tag{5.27}$$

Using an approach similar to Section 5.2.1, $w(r, \theta, z)$ may be written as

$$w(r, \theta, z) = \sum_{m=0}^{\infty} \sum_{n=1}^{\infty} C_{mn} \; I_{\nu_m}(\eta_n \; \sqrt{k_z/k_r}) \; cos(m\theta) \left[\frac{h_{end}}{\eta_n k_z} \sin \eta_n z + \cos \eta_n z \right] \tag{5.28}$$

where I is the modified Bessel function of the first kind. The order of the Bessel function is given by,

$$\nu_m = m\sqrt{k_\theta / k_r} \tag{5.29}$$

The eigenvalues η_n are determined from roots of the equation,

$$\tan \nu_n H = \frac{2\nu_n H Bi}{(\nu_n H)^2 - Bi^2} \tag{5.30}$$

The solution form shown in equation (5.28), when substituted in the boundary condition at r = R, given by equation (5.27) results in

$$\begin{aligned} k_r \eta_n \sqrt{\frac{k_z}{k_r}} \sum_{m=0}^{\infty} \sum_{n=1}^{\infty} C_{mn} \left[\frac{m}{\eta_n R} \sqrt{\frac{k_\theta}{k_z}} \; I_{\nu_m} \; \left(\eta_n \; \sqrt{\frac{k_z}{k_r}} \; R \right) + I_{\nu_m + 1} \; \left(\eta_n \; \sqrt{\frac{k_z}{k_r}} R \right) \right] \\ cos(m\theta) \left[\frac{h_{end}}{\eta_n k_z} \sin(\eta_n z) + \cos(\eta_n z) \right] + \sum_{m=0}^{\infty} \sum_{n=1}^{\infty} C_{mn} \; h(\theta, z) I_{\nu_m} \left(\eta_n \; \sqrt{\frac{k_z}{k_r}} R \right) \\ cos(m\theta) \left[\frac{h_{end}}{\eta_n k_z} \sin(\eta_n z) + \cos(\eta_n z) \right] = -h(\theta, z) f(z) \end{aligned} \tag{5.31}$$

Using a similar approach as shown in Section 5.2.1 following equation (5.14), use of orthogonality in Eq. (5.31) results in a set of linear equations involving the unknown coefficients given by,

$$C_{ji}b_{ji} + \sum_{m=0}^{\infty}\sum_{n=1}^{\infty} C_{mn}d_{jimn} = f_{ji} \tag{5.32}$$

where

$$b_{ji} = \eta_i\sqrt{k_z\ k_r}\ \left[\frac{j}{\eta_i R}\ \frac{k_\theta}{k_z}\ I_{\nu_j}\ \left(\eta_i\ \sqrt{\frac{k_z}{k_r}}\ R\right) + I_{\nu_j+1}\ \left(\eta_i\ \sqrt{\frac{k_z}{k_r}}\ R\right)\right]\ N_\theta N_z \tag{5.33}$$

$$d_{jimn} = I_{\nu_m}\ \left(\eta_n\ \sqrt{\frac{k_z}{k_r}}R\right)\int_{z=0}^{H}\int_{\theta=0}^{2\pi} h(\theta,z)\cos\left(m\theta\right)\cos\left(j\theta\right.$$
$$\left[\frac{h_{end}}{\eta_n k_z}\sin(\eta_n z) + \cos(\eta_n z)\right]\ \left[\frac{h_{end}}{\eta_i k_z}\sin(\eta_i z) + \cos(\eta_i z)\right]\ d\theta\ dz \tag{5.34}$$

$$f_{ji} = -\int_{z=0}^{H}\int_{\theta=0}^{2\pi} h(\theta,z)f(z)\cos(j\theta)\left[\frac{h_{end}}{\eta_n k_z}\sin(\eta_n z) + \cos(\eta_n z)\right]d\theta dz \tag{5.35}$$

The norms N_θ and N_z in equation (5.33) are given by [92]

$$N_\theta = \int_{\theta=0}^{2\pi}\cos^2(j\theta)d\theta = \begin{cases} 2\pi & \text{when } j = 0 \\ \pi & \text{when } j \neq 0 \end{cases} \tag{5.36}$$

$$N_z = \frac{h_{end}}{\eta_n k_z}\sin(\eta_n z) + \cos(\eta_n z) = \left(\frac{h_{end}^2}{(\eta_i k_z)^2} + 1\right)\ \frac{H}{2} + \frac{h_{end}}{k_z\eta_i^2} \tag{5.37}$$

Solving the set of linear algebraic equations involving the coefficients C_{mn} given by equation (5.32) results in the determination of the temperature distribution for the

finite cylinder given by equation (5.22). Note that the ratios of various thermal conductivities appearing in the solution account for the thermal conduction anisotropy in the cylinder. Putting $k_r = k_\theta = k_z$ results in a solution for the isotropic cylinder.

5.3 Results and Discussions

Fig. 5.2 presents a polar plot of temperature distribution in an infinite cylinder of radius 13 mm with $Re = 7960$ computed using the model in Section 5.2.1. The h-variation of θ is obtained from well-known experimental data [43]. Radial and circumferential thermal conductivities are assumed to be $k_r = 0.2W/m - K$and $_\theta = 30W/m - K$, respectively, based on recent measurements on a 26650 Li-ion cell [2]. While the h-variation in the temperature distribution shown in Figure 5.2 may not be readily apparent due to the much larger radial variation, it is clearly seen in Figure 5.3, which presents line plots of temperature distribution as a function of h at the outer surface (Figure 5.3(a)), and as a function of r (Figure 5.3(b)). Inset in Figure 5.3(a) shows the variation of h as a function of θ. Figures 5.3(a) and 5.3(b) also present the temperature distributions predicted by a finite-element simulation. Similar plots are presented for a finite-cylinder at the mid-height in Figures 5.4(a) and 5.4(b). For the finite cylinder case, a cylinder of radius 13 mm and height 65 mm is used, which corresponds to the geometry of the commonly used 26650 Li-ion cell. Figs. 5.3 and 5.4 show that the infinite cylinder and finite cylinder models are both in excellent agreement with finite-element simulation results. The temperature field is found to have maxima and minima at h locations where the distribution of the heat transfer coefficient has minima and maxima respectively. This is along expected lines since a large value of the local convective heat transfer coefficient results in greater local heat transfer from the solid to the fluid, and thus lower solid temperature.

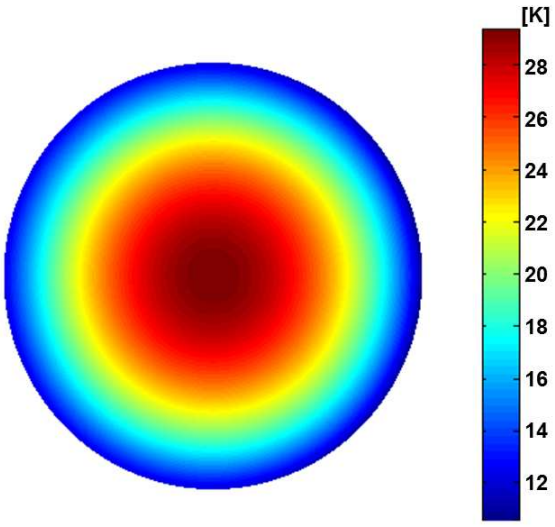

Figure 5.2. Polar plot of the temperature distribution in an anisotropic infinite cylinder at $Re = 7960$.

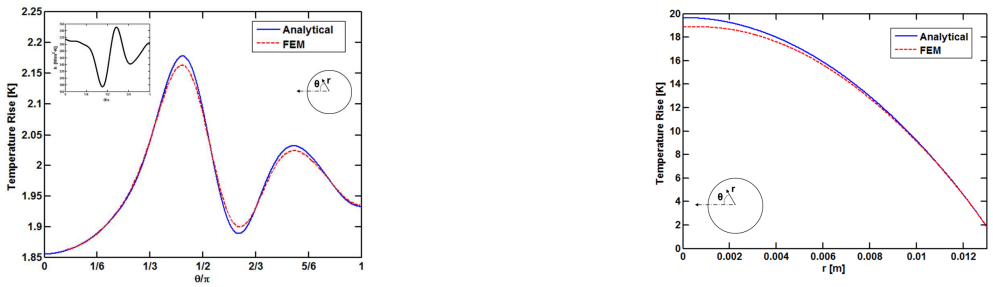

(a) (b)

Figure 5.3. Comparison of the analytically computed temperature distribution for the infinite cylinder with finite-element modeling results (a) shows variation with θ, (b) shows variation with r.

While the model predictions and finite-element simulation results are within less than 1% of each other for most of the cylinder, the maximum deviation between the two is about 3%, which occurs at the temperature peaks. This small error occurs possibly due to approximations related to the number of eigenvalues used in the model, and due to numerical errors in computing the integrals present in the

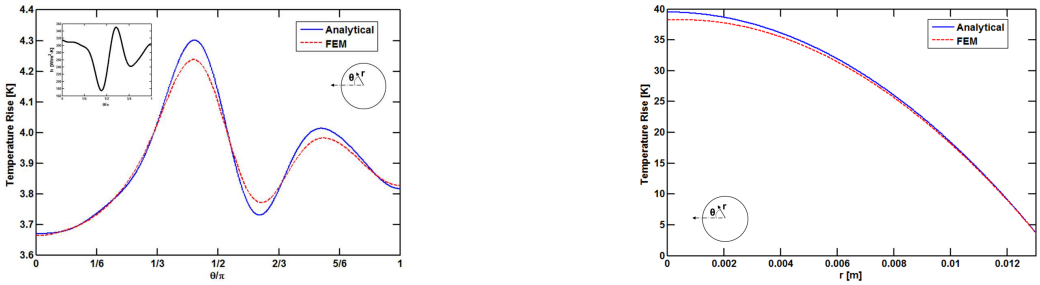

(a) (b)

Figure 5.4. Comparison of the analytically computed temperature distribution for the finite cylinder at mid-height with finite-element modeling results (a) shows variation with θ, (b) shows variation with r.

model. Additionally, approximations in the finite-element simulation may also have contributed to the small error.

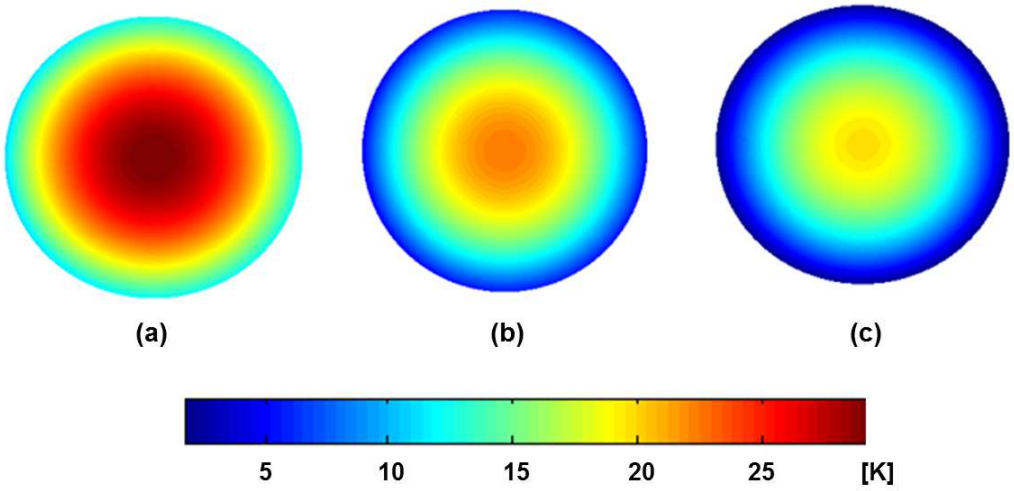

Figure 5.5. Polar plots for the temperature distribution in an anisotropic infinite cylinder with three different values of Reynolds number, with $k_r = 0.2W/m - K$, $k_\theta = 30W/m - K$ based on recent measurements.

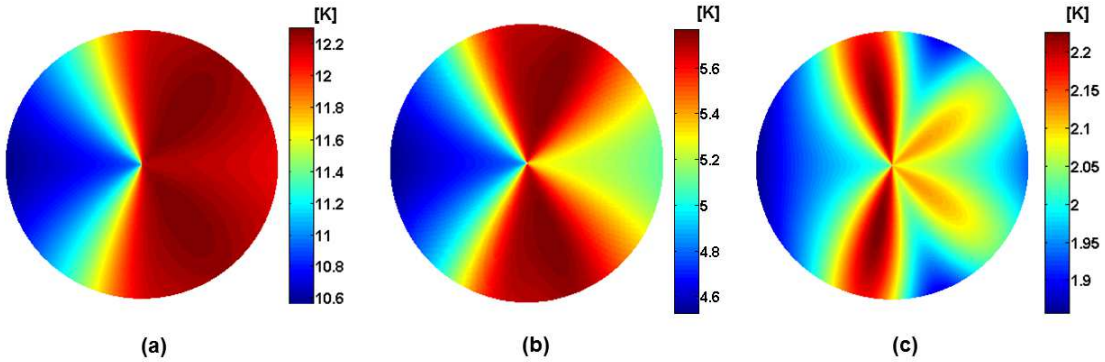

Figure 5.6. Polar plots for the temperature distribution in an anisotropic infinite cylinder with three different values of Reynolds number, with $k_r = 30W/m - K$, $k_\theta = 0.2W/m - K$.

The model presented in Section 5.2 is next used to determine the temperature distribution within the cylinder for different values of *Re*. Well-known measurements of the convective heat transfer coefficient on the cylinder surface as a function of h at various values of Re [43] are used in these computations. Figure 5.5 shows polar plots of temperature distribution in the cylinder for three values of Re. The thermal properties and heat generation rate are the same as used in Figures. 5.2 and 5.3. Figure 5.5 shows that as Re increases, the temperature field within the cylinder reduces, as expected. In addition, these polar plots also demonstrate the radial and circumferential variations in the temperature field within the cylinder. As expected, the core of the cylinder is the hottest in each case, while the outer surface directly facing the fluid flow is the coolest. In order to illustrate the strong effect of anisotropy in thermal conduction, Figure 5.6 shows temperature plots at three values of Re, with

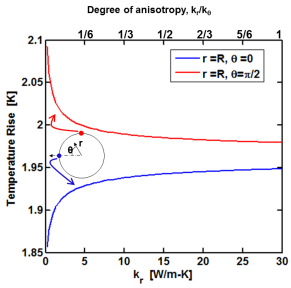

Figure 5.7. Plot of temperature rise as a function of the degree of thermal conduction anisotropy in an infinite cylinder.

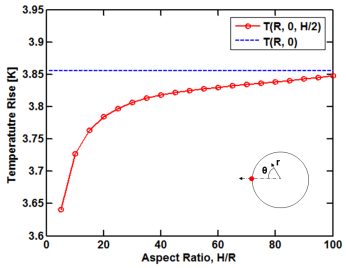

Figure 5.8. Plot of temperature as a function of aspect ratio for a finite cylinder.

$k_r = 30W/m-K$ and $k_\theta = 0.2W/m-K$, which is the opposite of the assumption for Figure 5.5. In this case, the much lower value of k_θ relative to k_r is expected to result in significant temperature gradients in the h direction, which is clearly seen in Figure 5.6. Recent measurements on a 26650 Li-ion cell [2] indicate that k_r is expected to be much lower than k_θ, which is why Figure 5.5 may be more representative of an actual Li-ion cell than Figure 5.6.

In order to further demonstrate the effect of anisotropic thermal conduction, the temperature field in the cylinder is computed as a function of the radial thermal conductivity, while keeping the other thermal conductivities constant. Figure 5.7 plots temperature at $\theta = 0°$, and $\theta = 90°$, both at r=R as functions of k_r. The ratio k_r/k_θ, which represents the degree of anisotropy is also indicated.

Figure 5.7 shows that the temperature at $\theta = 0°$ increases while the temperature at $\theta = 90°$ decreases as k_r increases. At large k_r, the temperatures at the two points converge to the same value, which is along expected lines, since the cylinder will behave as an isothermal body in the limit of large k_r. Finally, the finite cylinder model is used to compute the temperature distribution in a finite cylinder as a function of

aspect ratio H/R, while keeping the volumetric heat generation rate constant. The temperature at the stagnation point at mid-height ($r = R, h = 0, z = H/2$) is plotted in Figure 5.8 as a function of the aspect ratio. Figure 5.8 also shows the temperature at this point for an infinite cylinder with the same volumetric heat generation rate and thermal properties. Figure 5.8 shows that as the aspect ratio increases, the temperature predicted by the finite model approaches that of the infinite cylinder, since the finite cylinder approaches the limit of an infinite cylinder as the aspect ratio increases.

CHAPTER 6

TEMPERATURE INSIDE AN ORTHOTROPIC SPHERE SUBJECT TO VARYING HEAT TRANSFER

6.1 Introduction

This chapter presents an analytical derivation to compute the temperature distribution in a solid sphere with spatially varying convective heat transfer coefficient on its surface. Thermal conduction within the sphere is assumed to be orthotropic in general, with different thermal conductivity values in r, ϕ and θ directions. Volumetric heat generation occurs within the sphere, which is cooled on the outside surface with a convective heat transfer coefficient that depends on both azimuthal and polar angles. A Fourier series form of the temperature distribution is assumed. It is shown that the series coefficients can be determined by solving a set of linear algebraic equations that account for the general spatial variation of h on the sphere surface. The temperature distribution computed by this analytical solution is found to be in good agreement with results from finite-element simulations. The dependence of the temperature profile on a number of parameters such as the heat transfer coefficient, thermal conduction orthotropy, etc. is discussed. The theoretical derivation of temperature field in a sphere with orthotropic thermal properties is important because while most commercial finite-element simulation tools enable analysis of orthotropic thermal conduction in rectangular and cylindrical coordinate systems, the treatment of orthotropic thermal conduction in spherical coordinates is not available. By deriving the temperature distribution for this very general case, the treatment presented

here may help expand the capability of thermal analysis in spherical coordinate systems.

6.2 Mathematical Model

This section presents the derivation of the steady state temperature distribution in an orthotropic sphere with internal volumetric heat generation and spatially dependent h. Based on the general derivation presented next in Section 6.2, a special case for a partially orthotropic sphere where $k_\phi = k_\mu$ is presented in Section 6.2.1. Section 6.2.3 discusses an alternate analytical approach for solving the general problem. Finally a brief discussion is presented, showing that for isotropic conditions, i.e. all thermal conductivities being the same, the solutions presented for the orthotropic and partially orthotropic cases reduce to that of the isotropic solution as one would expect.

6.2.1 Orthotropic Sphere

Figure 6.1 shows a schematic of the general heat transfer problem being addressed in this sub-section. The steady-state governing energy equation in a three dimensional orthotropic sphere is given by,

$$k_r \left[\frac{\partial^2 T}{\partial r^2} + \frac{2}{r}\frac{\partial T}{\partial r}\right] + \frac{k_\phi}{r^2(1-\mu^2)}\,\frac{\partial^2 T}{\partial \phi^2} + \frac{k_\mu}{r^2}\,\frac{\partial}{\partial \mu}\left[(1-\mu^2)\frac{\partial T}{\partial \mu}\right] + g = 0 \qquad (6.1)$$

where $T(r, \phi, \mu)$ is the temperature rise above ambient, $\mu = \cos(\theta)$, k_r, k_ϕ and k_μ are thermal conductivities in the r, μ and ϕ directions, and g is the volumetric heat generation rate.

The temperature distribution is subject to the following boundary conditions,

$$T < \infty, \text{ bounded and finite}, \frac{\partial T}{\partial r} = 0 \qquad \text{at} \qquad r = 0 \qquad (6.2)$$

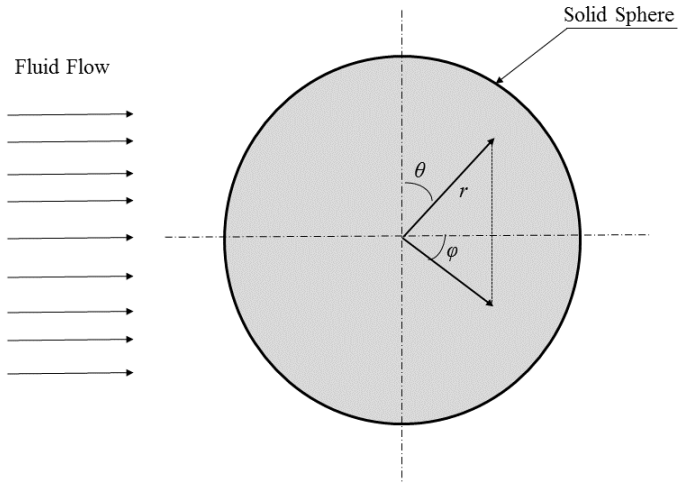

Figure 6.1. Schematic of the problem.

$$k_r \frac{\partial T}{\partial r} + h(\phi, \mu)\, T = 0 \qquad \text{at} \qquad r = R \tag{6.3}$$

$$T(r, \phi, \mu) = T(r, \phi + 2\pi, \mu) \tag{6.4}$$

$$\left(\frac{\partial T}{\partial \phi}\right)_{\phi=0} = \left(\frac{\partial T}{\partial \phi}\right)_{\phi+2\pi} \tag{6.5}$$

Equation (6.2) represents the requirement for the temperature field to be finite at $r = 0$. The circumferential variation of h at $r = R$ is accounted for by equation (6.3). Equations. (6.4) and (6.5) represent temperature periodicity and heat flux continuity in the ϕ direction. In addition to satisfying equations (6.1) - (6.5) the temperature field must also remain bounded in the μ direction [92].

If h were a constant number, then the solution for equations (6.1) - (6.5) can be obtained by the separation of variables method in a straightforward fashion [92].

However, the general case of spatially varying h considered here cannot be addressed by this approach. In this case, the temperature field is first transformed as follows:

$$T(r,\phi,\mu) = w(r,\phi,\mu) - \frac{gr^2}{6k_r} \tag{6.6}$$

In equation (refeq:7-6), the second term absorbs the non-homogeneity in the governing equation, thereby leaving a homogeneous governing equation for $w(r,\phi,\mu)$ and transferring the non-homogeneity to the boundary condition at $r = R$ for w. The set of equations for $w(r,\phi,\mu)$ is as follows,

$$k_r \left[\frac{\partial^2 w}{\partial r^2} + \frac{2}{r}\frac{\partial w}{\partial r}\right] + \frac{k_\phi}{r^2(1-\mu^2)}\,\frac{\partial^2 w}{\partial \phi^2} + \frac{k_\mu}{r^2}\,\frac{\partial}{\partial \mu}\left[(1-\mu^2)\frac{\partial w}{\partial \mu}\right] = 0 \tag{6.7}$$

subject to

$$w < \infty,\ \text{bounded and finite},\ \frac{\partial w}{\partial r} = 0 \qquad \text{at} \qquad r = 0 \tag{6.8}$$

$$k_r\,\frac{\partial w}{\partial r} + h(\phi,\mu)\ w = F(\phi,\mu) \qquad \text{at} \qquad r = R \tag{6.9}$$

$$w(r,\phi,\mu) = w(r,\phi+2\pi,\mu) \tag{6.10}$$

$$\left(\frac{\partial w}{\partial \phi}\right)_{\phi=0} = \left(\frac{\partial w}{\partial \phi}\right)_{\phi+2\pi} \tag{6.11}$$

where

$$F(\phi,\mu) = \frac{gR}{3}\,\left(1 + \frac{h(\phi,\mu)R}{2k_r}\right) \tag{6.12}$$

The solution for $w(r, \phi, \mu)$ is written in the form of the following infinite series:

$$w(r,\phi,\mu) = \sum_{n=0}^{\infty}\sum_{m=0}^{n} C_{nm}\ cos(m\phi)\ P_n^{\sqrt{\beta}\ m}(\mu)\ \left(\frac{r}{R}\right)^{-0.5+\sqrt{\alpha n^2+\alpha n+0.25}} \tag{6.13}$$

where $\alpha = k_\mu/k_r$ and $\beta = k_\phi/k_\mu$.

This particular form of the solution is chosen because it satisfies the governing differential equation (6.7) and several boundary conditions, given by equations (6.8), (6.10) and (6.11). Note that in general, the associated Legendre functions in equation (6.13) may have non-integer order due to unequal thermal conductivities in the polar and azimuthal directions. The coefficients C_{nm} in equation (6.13) can then be calculated to satisfy the boundary condition at the surface $r = R$, given by equation (6.9). To do so, the form of $w(r, \mu, \phi)$ given by equation (6.13) is inserted in equation (6.9), resulting in

$$k_r \sum_{n=0}^{\infty}\sum_{m=0}^{n} C_{nm}\ cos(m\phi)\ P_n^{\sqrt{\beta}\ m}(\mu)\ \left(\frac{-0.5+\sqrt{\alpha n^2+\alpha n+0.25}}{R}\right) + h(\phi,\mu)\sum_{n=0}^{\infty}\sum_{m=0}^{n} C_{nm}\ cos(m\phi)\ P_n^{\sqrt{\beta}\ m}(\mu) = F(\phi,\mu) \tag{6.14}$$

While equation 6.14 involves infinite series in both polar and azimuthal directions, it can be simplified by multiplying throughout by $\cos(j\phi)$ and $P^{\sqrt{\beta}j}(\mu)$, and then integrating over ϕ and μ. Since h is in general a function of ϕ and μ, this results in a set of linear equations involving the unknown coefficients, given by

$$C_{ij}\ a_{ij} + \sum_{n=0}^{\infty}\sum_{m=0}^{n} C_{nm} b_{ijnm} = f_{ij} \quad \text{for each} \quad i = 0,1,2,3,....and \quad j \le i \tag{6.15}$$

where,

$$a_{ij} = \left(\frac{-0.5+\sqrt{\alpha\ i^2+\alpha\ i+0.25}}{R}\right) \int_{\theta=0}^{2\pi} \cos^2(j\phi)\ d\phi \int_{\mu=-1}^{1} \left[P_i^{\sqrt{\beta}j}(\mu)\right]^2\ d\mu \tag{6.16}$$

$$b_{ijnm} = \int_{\theta=0}^{2\pi} \int_{\mu=-1}^{1} h(\phi,\mu)\ \cos(m\phi)\cos(j\phi)\ P_n^{\sqrt{\beta}m}(\mu) P_i^{\sqrt{\beta}j}(\mu)\ d\mu\ d\phi \tag{6.17}$$

$$f_{ij} = \int_{\theta=0}^{2\pi} \int_{\mu=-1}^{1} F(\phi,\mu)\ \cos(j\phi)\ d\phi\ P_i^{\sqrt{\beta}j}(\mu)\ d\mu\ d\phi \tag{6.18}$$

Assuming that zero through N eigenvalues are considered in the μ direction, equation (6.15) represents a set of $(N+1)\times(N+2)/2$ linear equations in the same number of unknowns C_{ij}, $i = 0, 1, 2, \ldots N$ and $j \leq i$, from where the unknown coefficients can be computed. For example, if eigenvalues up to $N = 10$ are considered, the total number of unknown coefficients is 66. Once the coefficients are computed, equations (6.6) and (6.13) represent the temperature distribution in the orthotropic cylinder. Note that in the special case of h being a constant, the integral in the expression for b_{ijnm} in equation6.17 would yield all zero values except when $i = n$ and $j = m$ due to orthogonality of eigenfunctions [92]. As a result, for this case, the coefficients C_{ij} can be computed explicitly, given by $(a_{ij} + d_{ijij})C_{ij} = f_{ij}$. This special case is the commonly used separation of variables approach where all coefficients are determined explicitly in case h is a constant. For the more general case of spatially varying h considered here, a set of linear algebraic equations given by equations (6.15) - (6.18) are to be solved to determine the series coefficients.

The next sub-section considers two special cases in which the fully orthotropic thermal conduction within the cylinder is relaxed.

6.2.2 Partially orthotropic and isotropic sphere

In several engineering applications, thermal conduction in the sphere may be partially orthotropic. For example, when the sphere is made up of multiple concentric layers, thermal conductivity in the radial direction may be lower than the other

two components due to thermal contact resistance between layers, whereas thermal conductivities in the azimuthal and polar directions may be equal, $k_\phi = k_\mu = k_c$, where k_c is a constant. The temperature distribution in such a case may be obtained from the treatment in Section 6.2.1 by setting $k_\phi = k_\mu = k_c$, and hence $\beta = 1$. The temperature distribution is still given by equation (6.6), but the modified form for $w(r, \phi, \mu)$ is as follows,

$$w(r,\phi,\mu) = \sum_{n=0}^{\infty}\sum_{m=0}^{n} C_{nm}\ cos(m\phi)\ P_n^m(\mu)\ \left(\frac{r}{R}\right)^{-0.5+\sqrt{\alpha n^2+\alpha n+0.25}} \tag{6.19}$$

In this case, the eigenfunctions in the l direction are associated Legendre polynomials, a special case of associated Legendre functions that appear in equation (6.13), with integer order, since $\beta = 1$. The procedure to determine the unknown coefficients C_nm in equation (6.19) remains the same as before. The matrix elements a_{ij}, b_{ijnm} and f_{ij} are somewhat simplified, and are now given by,

$$a_{ij} = \left(\frac{-0.5+\sqrt{\alpha\ i^2+\alpha\ i+0.25}}{R}\right)\int_{\theta=0}^{2\pi}\cos^2(j\phi)\ d\phi\int_{\mu=-1}^{1}\left[P_i^j(\mu)\right]^2\ d\mu \tag{6.20}$$

$$b_{ijnm} = \int_{\theta=0}^{2\pi}\int_{\mu=-1}^{1} h(\phi,\mu)\ \cos(m\phi)\cos(j\phi)\ P_n^m(\mu)P_i^j(\mu)\ d\mu\ d\phi \tag{6.21}$$

$$f_{ij} = \int_{\theta=0}^{2\pi}\int_{\mu=-1}^{1} F(\phi,\mu)\ \cos(j\phi)\ d\phi\ P_i^j(\mu)\ d\mu\ d\phi \tag{6.22}$$

Note that the integer order of the associated Legendre polynomials leads to significant reduction in computational cost. Explicit expressions for the integrals in equations (6.20)(6.22) are available for integer order only [92,108,109]. These integrals can also be computed symbolically [110] for any arbitrary, even function $h(\phi, \mu)$. In

comparison, for the more general, orthotropic case discussed in, Section 6.2.1, exact expressions for the norm integral, as well as the double integrals for b_{ijnm} and f_ij are not available, and must be computed numerically.

As a further step, substituting $k_r = k_c$ in equations above reduces the temperature distribution to the special case of an isotropic sphere with identical thermal conductivity in all directions. In this case, while $T(r, \phi, \mu)$ is still given by equation (6.6), $w(r, \phi, \mu)$ has a simplified form given by,

$$w(r, \phi, \mu) = \sum_{n=0}^{\infty} \sum_{m=0}^{n} C_{nm} \; cos(m\phi) \; P_n^m(\mu) \; \left(\frac{r}{R}\right)^n \tag{6.23}$$

The coefficients are still governed by a set of linear algebraic equations given by equation (6.15). b_{ijmn} and f_{ij} are given by equations (6.21) and (6.22) respectively. Due to isotropy in thermal conductivity, expression for a_{ij} given previously by equation (6.20) can be simplified further to,

$$a_{ij} = \left(\frac{i}{R}\right) \int_{\theta=0}^{2\pi} \cos^2(j\phi) \; d\phi \int_{\mu=-1}^{1} \left[P_i^j(\mu)\right]^2 \; d\mu \tag{6.24}$$

6.2.3 Alternate analytical approach for orthotropic sphere

This section presents an alternate approach for solving the general problem involving orthotropic thermal conduction given by equations (6.1)(6.5) in Section 6.2.1. In this approach, the temperature is still transformed as given by equation (6.6). However, instead of equation (6.13), the functional form for $w(r, \phi, \mu)$ is written as follows,

$$w(r, \phi, \mu) = \sum_{n=0}^{\infty} \sum_{m=0}^{n} C_{nm} \; cos(m\phi) \; P_{\eta_n}^{\nu_m}(\mu) \; \left(\frac{r}{R}\right)^n \tag{6.25}$$

where $\eta_n = -0.5 + \sqrt{\bar{\alpha}n^2 + \bar{\alpha}n + 0.25}$, $\bar{\alpha} = 1/\alpha$ and $\nu_m = \beta m$. α and β are ratios of thermal conductivities as defined earlier in Section 6.2.1. In general, η_n and nu_m , the degree and order respectively of the associated Legendre function in equation (6.25) can be non-integers [111]. Due to the arbitrary nature of both degree and order, the associated Legendre function appearing in Eq. (25) is now expressed by a Gauss hypergeometric series [111]. Such functions are encountered, for example in problems related to a sphere surface cut by a cone [92].

Note that similar to equation (6.13) , the functional form of w represented by equation (6.25) satisfies equations (6.7), (6.8), (6.10) and (6.11), and the series coefficient C_{nm} may be determined using a procedure similar to Section 6.2.1 utilizing the boundary condition involving the spatially vaying convective heat transfer coefficient, given by equation (6.9).

$$k_r \sum_{n=0}^{\infty}\sum_{m=0}^{n} C_{nm}\ cos(m\phi)\ P_{\eta_n}^{\nu_m}(\mu)\ \left(\frac{n}{R}\right) + h(\phi,\mu)\sum_{n=0}^{\infty}\sum_{m=0}^{n} C_{nm}\ cos(m\phi)\ P_{\eta_n}^{\nu_m}(\mu) = F(\phi,\mu) \quad (6.26)$$

Similar to Section 6.2.1, equation (6.26) is multiplied throughout by $\cos(j\phi)$ and $P_{\eta_i}^{\nu_j}$ to result in the following linear system for the series coefficients,

$$C_{ij}\ a_{ij} + \sum_{n=0}^{\infty}\sum_{m=0}^{n} C_{nm}\ b_{ijnm} = f_{ij} \quad \text{for each} \quad i = 0,1,2,3,\ldots n \quad and \quad j \le i \quad (6.27)$$

where

$$a_{ij} = \left(\frac{i}{R}\right)\int_{\theta=0}^{2\pi} \cos^2(j\phi)\ d\phi \int_{\mu=-1}^{1} \left[P_{\eta_i}^{\nu_j}(\mu)\right]^2\ d\mu \quad (6.28)$$

$$b_{ijnm} = \int_{\theta=0}^{2\pi} \int_{\mu=-1}^{1} h(\phi,\mu)\ \cos(m\phi)\cos(j\phi)\ P_{\eta_n}^{\nu_m}(\mu)\ P_{\eta_i}^{\nu_j}(\mu)\ d\mu\ d\phi \tag{6.29}$$

$$f_{ij} = \int_{\theta=0}^{2\pi} \int_{\mu=-1}^{1} F(\phi,\mu)\ \cos(j\phi)\ d\phi\ P_{\eta_i}^{\nu_j}(\mu)\ d\mu\ d\phi \tag{6.30}$$

In general, the associated Legendre function is defined by the Gauss hypergeometric series in the region $|\mu^2| < 1$ for any arbitrary μ, η and ν [111]. Substituting $\alpha = \beta = 1$ in equation (6.25) results in the solution for isotropic thermal conduction within the sphere, as expected.

Thus, a general solution for temperature in an orthotropic spherical body has been derived in two different ways, and special, less restrictive cases have been discussed. In the next section, the various theoretical models presented in this section are computed. Results are compared against finite element simulations, and the effect of various properties and geometry on the temperature distribution is discussed.

6.3 Results and Discussion

Figure 6.2 shows a polar plot of temperature distribution in a solid sphere of radius 10 cm with uniform heat generation rate, $Q = 1432.39 W/m^3$, based on a total heat generation rate of 6W in the sphere. The ϕ variation of h is chosen to be $h(\phi) = h_0\ (1 + cos^2(\phi/2))$ with $h_0 = 100 W/m^2K$, an even function with maxima at $\phi = 0$ and $\phi = \pi/2$, and minima at $\phi = \pi/2$. Radial, azimuthal and polar thermal conductivities are assumed to be $k_r = 0.2 W/m - K$, $k_\mu = 20 W/m - K$ and $k_\phi = 30 W/m - K$ respectively, consistent with the expectation that for a sphere made of multiple layered materials, the radial thermal conductivity will be the lowest due to multiple thermal contact resistances between layers. Temperature variation in Figure 6.2 is predominantly in the radial direction due to the low value of k_r

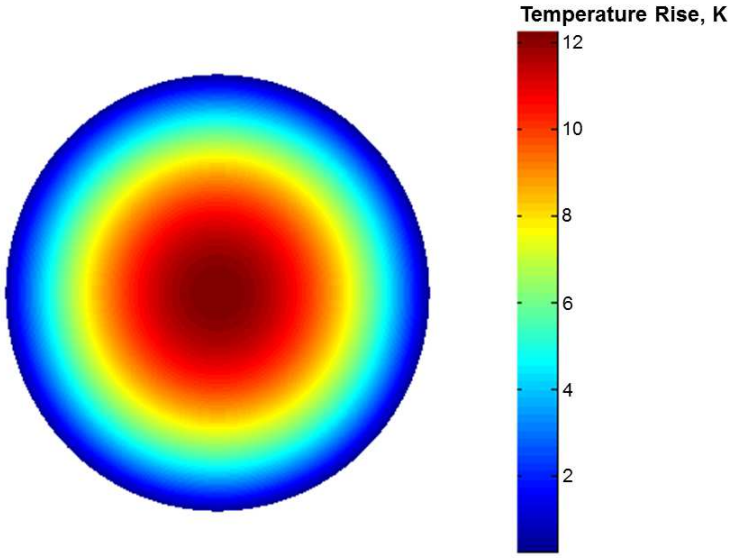

Figure 6.2. Polar plot for temperature distribution for an orthotropic sphere with $k_r = 0.2W/m - K$, $k_\phi = 30W/m - K$ and $k_\mu = 20W/m - K$.

relative to k_μ and k_ϕ. The temperature gradient in the ϕ direction is seen more clearly in Figure 6.3, which presents line plots of temperature distribution for the isotropic sphere ($k = 0.2W/m - K$) as a function of r along the plane $\theta = \pi/2$ and $\phi = 0$ which is the region that includes the stagnation point (Figure 6.3(a)), and similarly temperature as a function of u at $r = R$ (Figure 6.3(b)). Inset in Figure 6.3(b) shows the variation of h as a function of ϕ. The location of the maxima in temperature coincides with the minima in h, which is also along expected lines. Figures 6.3(a) and 6.3(b) also present comparison of the temperature distribution obtained from the analytical model discussed in Section 6.2 for the isotropic case with results from finite-element simulation. The finite-element simulations are carried out in ANSYS CFX, with sufficiently refined grid to rule out grid dependence. Good agreement is found between the temperature distribution computed from equations (6.6), (6.23) and (6.24) and the one predicted by the finite element model. Note

that since orthotropic thermal conduction in spherical coordinate systems cannot be modeled in ANSYS CFX, the comparison between analytical model and finite-element simulations shown in Figure 6.3 has been carried out only for the case of isotropic thermal conduction.

(a) (b)

Figure 6.3. Comparison of analytical solution for the temperature distribution in an isotropic sphere with finite-element modeling results (a) shows variation with r, (b) shows variation with ϕ.

Figure 6.4 shows temperature variation in the radial direction with changing values of k_r, while holding k_ϕ and k_μ at a constant value of $0.2W/m-K$. The temperature increases as k_r reduces, as expected. It is found that the partially orthotropic temperature distribution given by equation (6.19) reduces to the temperature solution for an isotropic sphere given by equation (6.24), also shown in Figure 6.4. Figure 6.5 analyzes a different case, where kr is held constant at $0.2W/m-K$, and k_ϕ is varied. The value of k_μ is held equal to k_ϕ. Figure 6.5 plots the temperature as a function of u along the surface at $r = R$ and $\phi = 0$. As expected, the peak temperature of the temperature curves illustrated in Figure 6.5 reduce as k_ϕ increases. The inset in Figure 6.5 shows the variation of h with ϕ. As expected, the maxima in temperature coincides with minima in the heat transfer coefficient.

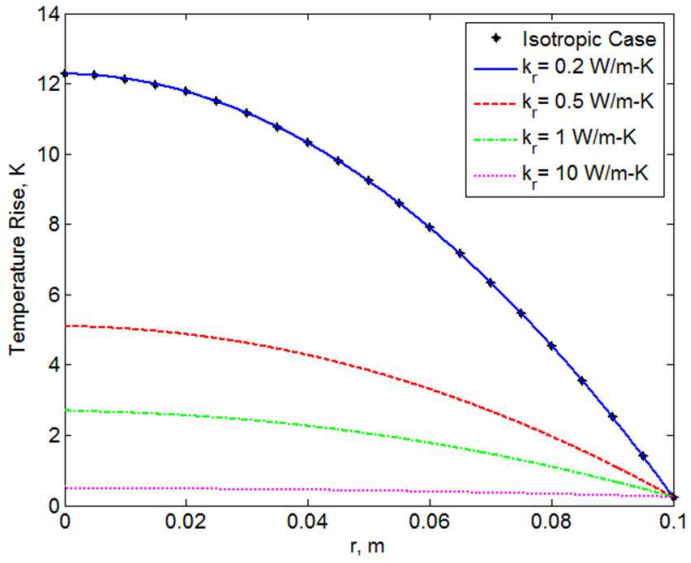

Figure 6.4. Plot for temperature distribution in an orthotropic sphere versus as a function of r for different values of k_r while maintaining $k_\phi = k_\mu = 0.2W/m - K$.

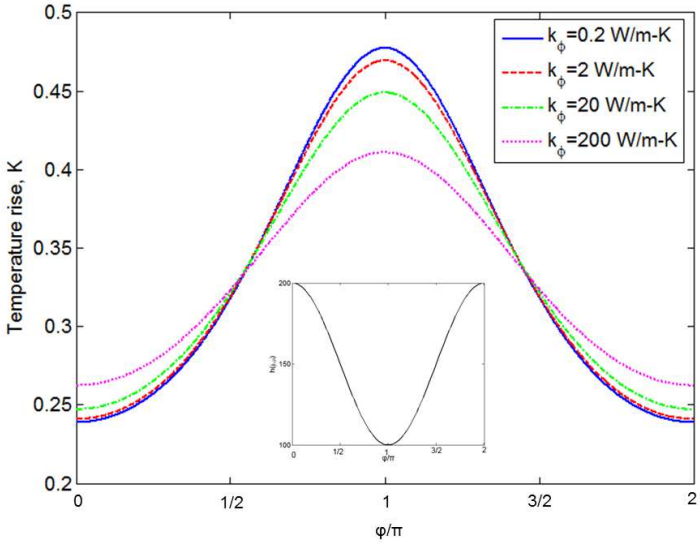

Figure 6.5. Plot for temperature distribution in an orthotropic sphere as a function of ϕ for different values of k_ϕ while maintaining $k_r = 0.2W/m - K$. The value of k_μ is equal to the k_ϕ for each case.

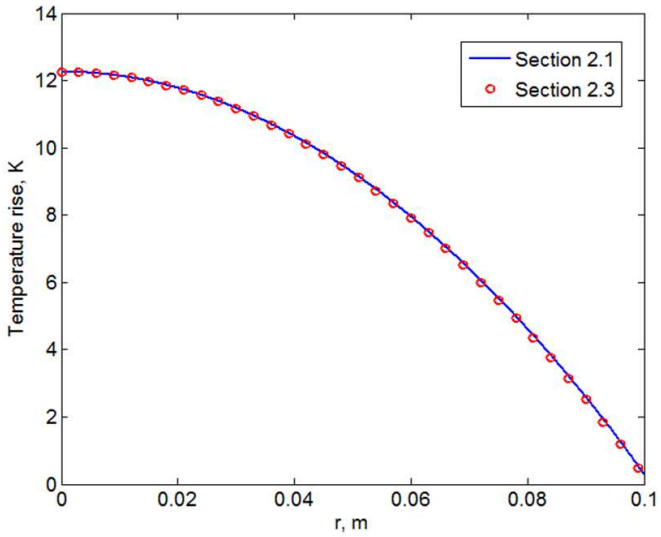

Figure 6.6. Plot for temperature distribution in an orthotropic sphere as a function of radius using two different solution techniques, for $k_r = 0.2W/m-K$, $k_\phi = 30W/m-K$ and $k_\mu = 20W/m - K$.

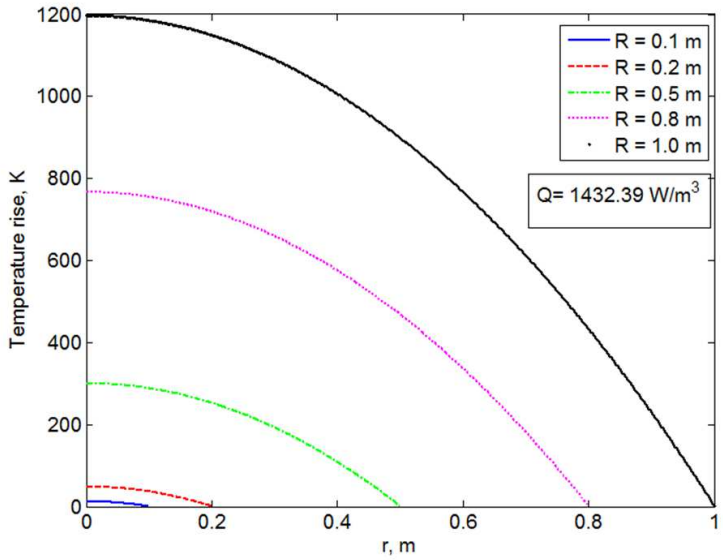

Figure 6.7. Plot for temperature distribution in an orthotropic sphere as a function of r for spheres of different radii R, while maintaining constant internal heat generation rate.

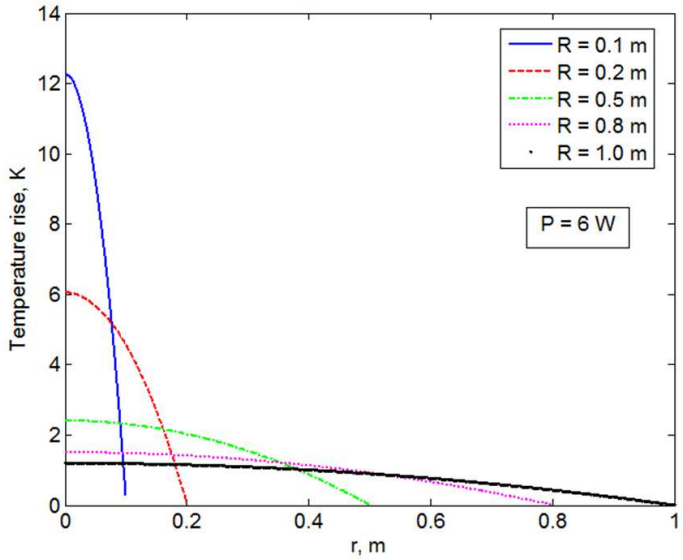

Figure 6.8. Plot for temperature distribution in an orthotropic sphere versus r for spheres of different radii R, while maintaining constant power.

(a) (b)

Figure 6.9. Comparison of analytical solution for the temperature distribution in an isotropic sphere with finite-element modeling results (a) shows variation with r, (b) shows variation with ϕ.

Figure 6.6 shows a comparison of the temperature distribution as a function of r for the two solution techniques discussed in Sections 6.2.1 and 6.2.3. There is good agreement between the two solutions, as expected, which shows that either of the

two approaches discussed in Sections 6.2.1 and 6.2.3 may be adopted for computing temperature field in a general, orthotropic sphere.

Figure 6.7 illustrates the variation in radial temperature distribution in spheres of different sizes with the volumetric heat generation rate maintained constant. The value of the volumetric heat generation rate is based on 6W power in a solid sphere of radius 0.1 m as the reference case. As expected, a sphere with a larger radius has a larger temperature gradient, due to greater power generated inside the sphere of a larger radius. Conversely, in Figure 6.8, the total power is held constant at 6W, and it is found that there is greater temperature rise in the small radius sphere due to the increased volumetric heat generation rate.

Finally, Figure 6.9 analyses the temperature variation in the radial and azimuthal directions as functions of convective cooling rates.As expected, the peak temperature drops in both cases with increase in the cooling rate. The reduction in temperature is less significant at higher values of h_0, which could be because at high h_0, total thermal resistance is dominated by thermal conduction within the sphere rather than convective thermal resistance at the boundary.

CHAPTER 7

CORRECTIONS FOR LATERAL CONDUCTION ERROR IN HEAT TRANSFER MEASUREMENTS

7.1 Introduction

Steady state measurements of convective heat transfer coefficient often use a constant wall heat flux condition along with measured temperature distribution to generate heat transfer coefficient maps. Large spatial gradients in the heat transfer coefficient may lead to lateral conduction within the heater foil, causing non-uniformity in the actual convective flux into the fluid, yielding errors in the calculated Nusselt numbers. This chapter presents an analytical procedure for correcting such errors for a model system with a known heat transfer coefficient distribution and nominal $1-D$ applied wall heat flux. The resulting $2-D$ conduction problem is parametrized in terms of the Biot number Bi and the heat transfer coefficient distribution, expressed by the change in magnitude r and the peak gradient γ, as well as the proximity of the gradient region to a symmetry plane. Three model configurations are studied: a region of large gradients that is located far away from lateral boundaries, and two cases where the gradient region is located near a symmetry plane, viz. impingement heat transfer due to a slot jet and a round jet.

It is shown that sharp spatial variations in heat transfer coefficient can lead to significant error in Nusselt number determination when the wall heat flux is assumed to be uniform. The error is shown to be amplified when the gradient region is located near a symmetry plane. Finally, the wall heat flux is correlated using of an expression that captures the results of the analytical calculations for the ranges of Bi, r

and γ studied, which can be used to evaluate experimental designs for heat transfer measurement, and make corrections for the two-dimensional nature of heat transfer in the foil and insulation.

The rest of this chapter is organized as follows: Section 7.2 presents the mathematical framework used to analyze the two-dimensional conduction problem. Briefly, it involves expansion of the unknown temperature field in terms of orthogonal functions (Fourier series) and applying the boundary conditions to evaluate the unknown coefficients. Section 7.2.1 discusses the problem of a slot jet for two cases, one when the jet width is much larger than the gradient region, and another when it is comparable. Section 7.2.2 repeats the analysis for a circular jet. Section 7.2.3 defines a heat flux correction factor, which can be applied to nominal $1 - D$ calculations in order to account for two-dimensional effects. Section 7.3 presents the results of the calculations, as well as correlations for the correction factor.

7.2 Mathematical Model

A typical test section for studying heat transfer to a jet from a constant-flux involves the use of a resistive foil of thickness b_2 (typically 50 mm) stretched over an insulating surface, as is shown in Figure 7.1. The insulation is usually a low conductivity polymer, with or without an air gap to further increase the thermal resistance beneath the foil. The present mathematical analysis can include variation in the fluid jet temperature, for example compressible jets and film cooling applications. If one accounts for such variations in the estimation of local heat transfer distribution, the analytical procedure illustrated here is well suited to estimate the error in the heat transfer distribution due to lateral conduction. The thickness b_1 of the insulation is chosen such that even for low values of the heat transfer coefficient, the thermal resistance in the downward direction (b_1/k_1) is much greater than the thermal resis-

tance above the foil ($1/h_{min}$). The thermal conductivities of the insulation and foil are given by k_1 and k_2. The convective heat transfer coefficient on the top surface is assumed to vary spatially, $h = h(x)$ or $h(r)$, as is the case with slot and radial jets.

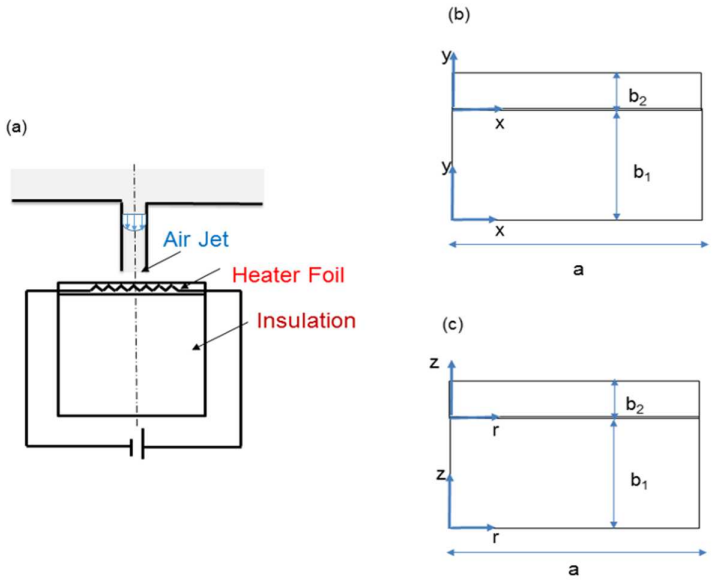

Figure 7.1. (a) Schematic of the experimental setup for jet impingement cooling of a metal foil with an insulation layer, (b) Geometry for slot jet cooling in cartesian coordinates, (c) Geometry for circular jet cooling in cylindrical coordinates.

To obtain the local wall heat flux at every location, we solve for the temperature distribution in a two-layer medium with heat generation in the top layer, which is convectively cooled. Using the temperature solution in the multilayer body, an expression for the heat flux correction factor is determined to account for the effect of lateral conduction. The mathematical model discussed in this section assumes thermal conduction in the insulation material to be anisotropic, as is often the case. Heat transfer in the case of isotropic materials is discussed as a special case. The error estimated by the correction factor results in quantification of the lateral conduction effects within the foil in regions of sharp gradient of convective heat transfer.

In order to understand the effects of gradient in heat transfer coefficient, we choose an idealized distribution which is parametrized in terms of its maximum and minimum values, as well as the region over which this variation occurs, expressed in terms of the maximum slope. For the case of a gradient region that is far away from any boundaries, we use the expression

$$\frac{h(x)}{h_{max}} = \frac{1 - R\ \tanh\left(\gamma\ \left(\frac{x-10}{w}\right)\right)}{1+R} \tag{7.1}$$

where $\rho = h_{max}/h_{min}$ and $R = (\rho - 1)/(\rho + 1)$. The parameter γ is directly proportional to the maximum slope in the heat transfer coefficient, and inversely proportional to the region over which the variation occurs. The parameter w, corresponds to the width of the gradient region for the case of an asymmetric jet and jet-half width for the case of a symmetric jet.

This expression is plotted in Figure 7.2 for $\rho = 5$ and various values of γ. The function asymptotes to 1 at $x/w = 5$ and to 0.2 at $x/w = 15$ where x/w is in the range of 0 - 20. The steepness of the gradient is characterized by the gradient parameter γ, and is centered at $x/w = 10$.

For the case corresponding to a slot/plane jet, we use the distribution to represent the case of an impingement region where the gradient region is centered on 1, adjacent to a symmetry plane. The expression is given by, $h(x) = h_{max}$ $\left(1 + R\ \tanh\left(\gamma\ \left(\frac{w}{x} - \frac{x}{w}\right)\right)\right)/(1+R)$. From observation, when $x \to 0$, $\tanh\left(\gamma\ \left(\frac{w}{x} - \frac{x}{w}\right)\right)$ ≈ 1. As a result, in the above expression, $h(x)$ reduces to h_{max} as $x \to 0$. A similar expression in radial coordinates is used in calculations for a round jet in which the spatial co-ordinate x in above equations for $h(x)$ is replaced by the radial co-ordinate r.

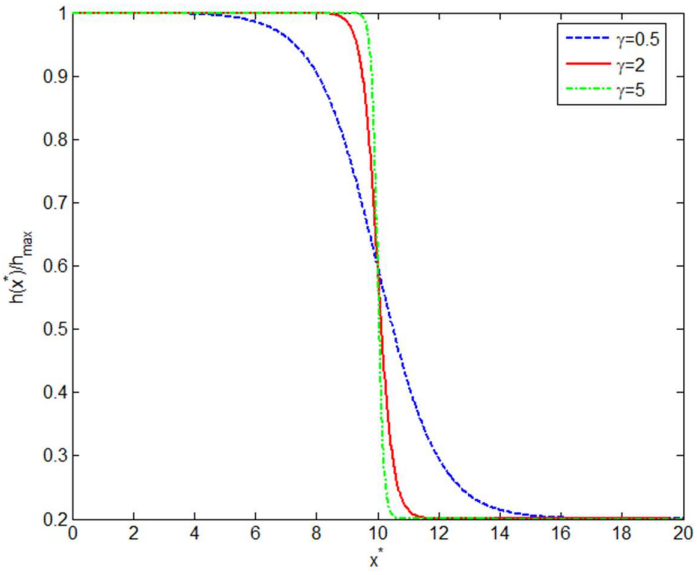

Figure 7.2. Heat transfer coefficient as a function of x for different values of γ.

7.2.1 Heat transfer due to a slot jet

The geometry of the slot jet case is shown in Figure 7.1(b). Note that while the heater foil (layer 2), typically a metal, is usually isotropic ($k_{2x} = k_{2y} = k_2$), thermal conduction in the insulation layer, typically a low thermal conductivity material, may be orthotropic ($k_{1x} \neq k_{1y}$). The following parameters are used for non-dimensionalization of this problem:

$$
\begin{aligned}
x^* = \frac{x}{w}; \quad y^* = \frac{y}{w};
\\
a^* = \frac{a}{w}; \quad b_1^* = \frac{b_1}{w}; \quad b_2^* = \frac{b_2}{w}
\\
T_j^* = \frac{k_2(T_j - T_\infty)}{g_2 \ w^2}
\\
Bi = \frac{h_{max} b_2}{k_2}
\\
\psi_j = \begin{cases} 0 & j = 1 \\ 1 & j = 2 \end{cases}
\end{aligned}
\tag{7.2}
$$

For convenience, the $(*)$ notation is dropped in the remainder of this paper, so that all subsequent variables are in dimensionless form. The governing energy conservation equation is given by

$$
\frac{\partial^2 T_j}{\partial x^2} + \frac{k_{jy}}{k_{jx}} \frac{\partial^2 T_j}{\partial y^2} + \frac{k_2 \ \psi_j}{k_{jx}} = 0 \qquad\qquad j = 1, 2 \tag{7.3}
$$

where heat generation occurs only in the metal foil layer due to Joule heating. It must also be noted that the heat generation in the foil due to Joule heating is assumed to be uniform. This is usually achieved by choosing a material with low temperature coefficient of resistance. This equation is subject to the following boundary conditions and interface conditions,

$$
T_1(x, 0) = 0 \tag{7.4}
$$

$$
\frac{\partial T_2}{\partial y} + \frac{Bi}{b_2} \ h(x) \ T_2 = 0 \qquad\qquad y = b_2 \tag{7.5}
$$

$$
\frac{\partial T_j}{\partial x} = 0 \qquad\qquad x = 0, a \qquad\qquad j = 1, 2 \tag{7.6}
$$

$$T_1(x, b_1) = T_2(x, b_2) \tag{7.7}$$

$$k_{1y} \left(\frac{\partial T_1}{\partial y}\right)_{y=b_1} = k_2 \left(\frac{\partial T_2}{\partial y}\right)_{y=0} \tag{7.8}$$

Equations (7.7) and (7.8) represent the compatibility condition at the interface where each layer is assigned its individual co-ordinate system with the origin at the bottom-left corner of each layer. The following transformation absorbs the non-homogeneity from the governing Equation (7.3),

$$T_j x, y = \theta_j(x, y) - \frac{k_2}{k_{jx}} \frac{\psi_j}{2} y^2 \tag{7.9}$$

Based on the above transformation the transformed boundary value problem is given by

$$\frac{\partial^2 \theta_j}{\partial x^2} + \frac{k_{jy}}{k_{jx}} \frac{\partial^2 \theta_j}{\partial y^2} = 0 \qquad\qquad j = 1, 2 \tag{7.10}$$

subject to the following boundary conditions and interface conditions

$$\theta_1(x, 0) = 0 \tag{7.11}$$

$$\frac{\partial \theta_2}{\partial y} + \frac{Bi}{b_2} h(x) \theta_2 = \psi_2 b_2 \left(1 + \frac{Bi\ h(x)}{2}\right) \qquad\qquad y = b_2 \tag{7.12}$$

$$\frac{\partial \theta_j}{\partial x} = 0 \qquad\qquad x = 0, a \qquad\qquad j = 1, 2 \tag{7.13}$$

$$\theta_1(x, b_1) = \theta_2(x, b_2) \tag{7.14}$$

$$k_{1y} \left(\frac{\partial \theta_1}{\partial y}\right)_{y=b_1} = k_2 \left(\frac{\partial \theta_2}{\partial y}\right)_{y=0} \tag{7.15}$$

Using Fourier series expansion and separation of variables, the temperature solutions in layers 1 and 2 are found to be given by,

$$\theta_1(x,y) = C_0(y) + \sum_{n=1}^{\infty} C_n \ \sinh(\lambda_n y) \ \cos(\lambda_n x) \tag{7.16}$$

$$\theta_2(x,y) = C_0\left(b_1 + \frac{y}{k}\right) + \sum_{n=1}^{\infty} C_n \ (\sinh(\lambda_n b_1)\cosh(\lambda_n y) + (1/\kappa \ \cosh(\lambda_n b_1)\sinh(\lambda_n y)) \ \cos(\lambda_n x) \tag{7.17}$$

where $\lambda_n^2 = \beta_n^2(k_{jy}/k_{jx})$ and $\beta_n = n\pi/a$. Substituting equation (7.17) in equation (7.12) results in a set of linear system of $N+1$ equations in $N+1$ variables, namely $C_0, C_1, C_2 \ldots C_N$ where N is the number of eigenvalues considered in the solution. In order to determine these unknown coefficients, the principle of orthogonality is used, resulting in,

$$C_0\left(\frac{a}{\kappa} + \frac{Bi}{b_2}\left(b_1 + \frac{b_2}{\kappa}\right)\right)\int_0^a h(x)dx + \sum_{n=1}^{\infty} C_n \ \left(\frac{Bi}{b_2}\right) P_n \int_0^a h(x)\cos(\lambda_n x)dx = \int_0^a F(x)dx \tag{7.18}$$

$$C_0\left(\frac{Bi}{b_2}\right)\left(b_1 + \frac{b_2}{\kappa}\right)\int_0^a h(x)\cos(\lambda_i x)dx + C_i\lambda_i\frac{S_i a}{2} + \sum_{n=1}^{\infty} C_n \ \left(\frac{Bi}{b_2}\right) P_n \int_0^a h(x)\cos(\lambda_n x)cos(\lambda_i x)dx = \int_0^a F(x)\cos(\lambda_i x)dx \tag{7.19}$$

where,

$$S_n = \sinh(\lambda_n b_1)\sinh(\lambda_n b_2) + (1/\kappa)\cosh(\lambda_n b_1)\cosh(\lambda_n b_2) \tag{7.20}$$

$$P_n = \sinh(\lambda_n b_1)\cosh(\lambda_n b_2) + (1/\kappa)\cosh(\lambda_n b_1)\sinh(\lambda_n b_2) \tag{7.21}$$

$$F(x) = \psi_2 b_2 \left(1 + \frac{Bi\ h(x)}{2}\right) \tag{7.22}$$

Equations (7.18) and (7.19) are the result of the use of orthogonality principle to obtain a linear system of $N + 1$ equations in $N + 1$ variables. The index i in Equation (7.19) corresponds to the contribution of the diagonal terms of the matrix. Note that the standard approach of using principle of orthogonality for constant heat transfer coefficient results in explicit expressions for each unknown coefficient. However, similar to other papers addressing space - dependent convective heat transfer coefficient [49, 86, 87], in this case, since h is a function of x, a set of coupled, linear algebraic equations is obtained. The coefficients, C_0 and C_n s can be obtained by solving this set of linear algebraic equations. The final temperature solution in each layer is then given by substituting equations (7.16) and (7.17) in equation (7.9). The mathematical treatment for a slot jet on an infinite plate is the same, however, an appropriate length of the plate must be chosen during analysis.

7.2.2 Heat transfer due to a radial jet

The methodology for deriving the temperature distribution for a radial jet is similar to a slot jet, except that the cylindrical coordinate system must be employed. Further, because the effect of orthotropic thermal conduction in layer 1 is found to be negligible, as discussed in Section 7.3, the derivation in this section is presented for an isotropic insulation layer. Non-dimensionalization is first carried out using the following equations:

$$
\begin{aligned}
r^* = \frac{r}{w}; \quad z^* = \frac{z}{w};\\
a^* = \frac{a}{w}; \quad b_1^* = \frac{b_1}{w}; \quad b_2^* = \frac{b_2}{w}\\
T_j^* = \frac{k_2(T_j - T_\infty)}{g_2\ w^2}\\
Bi = \frac{h_{max} b_2}{k_2}\\
\psi_j = \begin{cases} 0 & j = 1 \\ 1 & j = 2 \end{cases}
\end{aligned}
\tag{7.23}
$$

Similar to section 7.2.1, the $(*)$ notation is dropped in the remainder of this section for convenience. In non-dimensional form, the temperature distribution is governed by,

$$
\frac{\partial^2 T_j}{\partial r^2} + \frac{1}{r}\frac{\partial T_j}{\partial r} + \frac{\partial^2 T_j}{\partial y^2} + \psi_j = 0 \qquad\qquad j = 1, 2 \tag{7.24}
$$

subject to the following boundary conditions and interface conditions,

$$
T_1(r, 0) = 0 \tag{7.25}
$$

$$
\frac{\partial T_2}{\partial z} + \frac{Bi}{b_2}\ h(r)\ T_2 = 0 \qquad\qquad z = b_2 \tag{7.26}
$$

$$
\frac{\partial T_j}{\partial r} = 0 \qquad\qquad r = 0, a \qquad\qquad j = 1, 2 \tag{7.27}
$$

$$
T_1(r, b_1) = T_2(r, b_2) \tag{7.28}
$$

$$
k_1\ \left(\frac{\partial T_1}{\partial z}\right)_{z=b_1} = k_2\ \left(\frac{\partial T_2}{\partial z}\right)_{z=0} \tag{7.29}
$$

Equations (7.28) and (7.29) represent the compatibility condition at the interface where each layer is assigned its individual co-ordinate system with the origin at the bottom-left corner of each layer. Similar to previous section, a transformation is introduced in order to absorb the non-homogeneity in the governing equation (7.24),

$$T_j r, z = \theta_j(r, z) - \frac{\psi_j}{2} z^2 \tag{7.30}$$

Based on the above transformation, the transformed boundary value problem is given by,

$$\frac{\partial^2 \theta_j}{\partial x^2} + \frac{1}{r}\frac{\partial \theta_j}{\partial r} + \frac{\partial^2 \theta_j}{\partial z^2} = 0 \qquad\qquad j = 1, 2 \tag{7.31}$$

subject to the following boundary conditions and interface conditions

$$\theta_1(r, 0) = 0 \tag{7.32}$$

$$\frac{\partial \theta_2}{\partial z} + \frac{Bi}{b_2}\ h(r)\ \theta_2 = \psi_2 b_2 \left(1 + \frac{Bi\ h(r)}{2}\right) \qquad\qquad z = b_2 \tag{7.33}$$

$$\frac{\partial \theta_j}{\partial r} = 0 \qquad\qquad r = 0, a \qquad\qquad j = 1, 2 \tag{7.34}$$

$$\theta_1(r, b_1) = \theta_2(r, b_2) \tag{7.35}$$

$$k_1\ \left(\frac{\partial \theta_1}{\partial z}\right)_{z=b_1} = k_2\ \left(\frac{\partial \theta_2}{\partial z}\right)_{z=0} \tag{7.36}$$

Following a similar procedure as Section 7.2.1, the temperature solutions in layers 1 and 2 are given by the following expressions,

$$\theta_1(r,z) = C_0 z + \sum_{n=1}^{\infty} C_n \ \sinh(\lambda_n z) \ J_0(\lambda_n r) \tag{7.37}$$

$$\theta_2(r,z) = C_0 \left(b_1 + \frac{z}{k}\right) + \sum_{n=1}^{\infty} C_n \ \left(\sinh(\lambda_n b_1)\cosh(\lambda_n z) + (1/\kappa \ \cosh(\lambda_n b_1)\sinh(\lambda_n z)\right) \ J_0(\lambda_n r) \tag{7.38}$$

where λ_n 's are roots of $J_1(\lambda_n a) = 0$. Substituting equation (7.38) in equation (7.33) results in a linear system of $N+1$ equations in $N+1$ variables. In order to determine the coefficients, the principle of orthogonality is used, resulting in the following set of algebraic equations in the unknown coefficients,

$$C_0 \left(\frac{a}{\kappa} + \frac{Bi}{b_2}\left(b_1 + \frac{b_2}{\kappa}\right)\right) \int_0^a r \ h(r) dr + \sum_{n=1}^{\infty} C_n \ \left(\frac{Bi}{b_2}\right) P_n \int_0^a r \ h(r) J_0(\lambda_n r) dr = \int_0^a r F(r) dr \tag{7.39}$$

$$C_0 \left(\frac{Bi}{b_2}\right)\left(b_1 + \frac{b_2}{\kappa}\right) \int_0^a r \ h(r) J_0(\lambda_i r) dr + C_i \lambda_i S_i N_{\lambda_i} + \sum_{n=1}^{\infty} C_n \ \left(\frac{Bi}{b_2}\right) P_n \int_0^a r h(r) J_0(\lambda_n r) J_0(\lambda_i r) dr = \int_0^a r F(r) J_0(\lambda_i r) dr \tag{7.40}$$

where

$$N_{\lambda_i} = \frac{a^2}{2} J_0^2(\lambda_i a) \tag{7.41}$$

$$F(r) = \psi_2 b_2 \left(1 + \frac{Bi \ h(r)}{2}\right) \tag{7.42}$$

Equations (7.39) - (7.41) are the result of the use of orthogonality principle in radial systems to obtain a linear system of $N+1$ equations in $N+1$ variables. The

index i in equations (7.40) and (7.41) corresponds to the contribution of the diagonal terms of the matrix. In addition, equation (7.41) represents the norm integral in radial systems [92]. Expressions for S_n and P_n are given by equations (7.20) and (7.21) in Section 7.2.1. On solving the linear system of equations simultaneously, the coefficients C_0 and C_n s are determined, and thus, the temperature solution in each layer is given by substituting equations (7.37) and (7.38) in Equation (7.30).

7.2.3 Heat flux correction factor

The heat flux correction factor needed to correctly account for lateral effects due to spatial variation in the heat transfer coefficient is defined as follows,

$$\bar{q_c} = \frac{(h_{max} b_2/k_2)\ \phi(x^*)\ T^*_{2,top}}{(b_2/w)^2} - 1 = \frac{Bi\ \phi(x^*)\ T^*_{2,top}}{(b_2^*)^2} - 1 \tag{7.43}$$

Equation (7.43) is the dimensionless form of the heat flux correction factor, in which $T_{2,top}$ is $T_2(x, b_2)$ or $T_2(r, b_2)$ for Cartesian and cylindrical coordinate systems respectively. Note that the '$*$' notation has been adopted only for Equation (7.43) in this section. This is to distinguish between dimensional and dimensionless parameters in the general definition of the heat flux correction factor.

Note that when the heat transfer coefficient $h(x)$ is constant, the two terms in the numerator $h(x)\ (T_{2,top} - T_\infty)$ and $g_2 b_2$ are equal to each other based on overall energy conservation, and thus $\bar{q_c}$ reduces to zero. When there is a spatial variation in h, Equation (7.43) accounts for the dimensionless correction factor in heat flux needed as a result. Note that this correction needs to be computed based on the temperature at the top of the two-layer structure, as given by the final results of Sections 7.2.1 and 7.2.2 for slot and circular jets respectively. For a fixed geometry and appropriate choice of thermal conductivity ratio, the heat flux correction factor $\bar{q_c}$ is a function

of three non-dimensional parameters - Bi, ρ and γ. While the theoretical models discussed above capture this dependence exactly, it is also desirable to determine simple power law correlations to represent these theoretical results. Such correlations could be used by experimentalists in the design of experiments and improvement in the accuracy of heat transfer measurements. The following section discusses results from this analysis.

7.3 Results and Discussion

Figure 7.3(a) illustrates the effects of lateral conduction for parameter values $Bi = 0.001$, $\rho = 5$ and $\gamma = 2$, for an infinite plate, i.e. for the case where the gradient region is far from any geometric boundaries. The peak positive and negative errors are labeled as e^+ and e^-. For a packet of thermal energy generated in the foil at a value of x just greater than 10, the path of least resistance is one that involves lateral conduction through the foil, and convection into the fluid at $x < 10$. The result is that around $x = 10$, the local wall-normal heat flux is no longer uniform, and increases above the nominally constant value for $x < 10$, and decreases for $x > 10$. In conventional methods of heat transfer measurements, this effect is not accounted for due to the one dimensional nature of the problem, whereas the two-dimensional analysis shown here accounts for this effect, resulting in greater accuracy.

For the case of a slot jet on a finite plate, Figure 7.3(b) shows a comparison of the heat flux correction curves between an orthotropic insulation material and its isotropic equivalent for $Bi = 0.001$, $\rho = 5$, $\gamma = 2$ and $\kappa = 1000$ where $\kappa = k_2/k_{1y}$ due to anisotropy and k_{1y} equals to k_1 for isotropic condition. Results indicate that there is not much variation in the correction factor for the case where the in-plane thermal conductivity is five times the out-of-plane thermal conductivity in the insulation material. For all subsequent results discussed in this section, both the resistive heater

(a) (b)

Figure 7.3. (a) Heat flux correction curve illustrating lateral conduction effects for a slot jet over an infinite metal foil. (b) Comparison of finite plate heat flux correction curves for isotropic insulation layer with an orthotropic case, where in-plane thermal conductivity is five times the out-of-plane thermal conductivity.

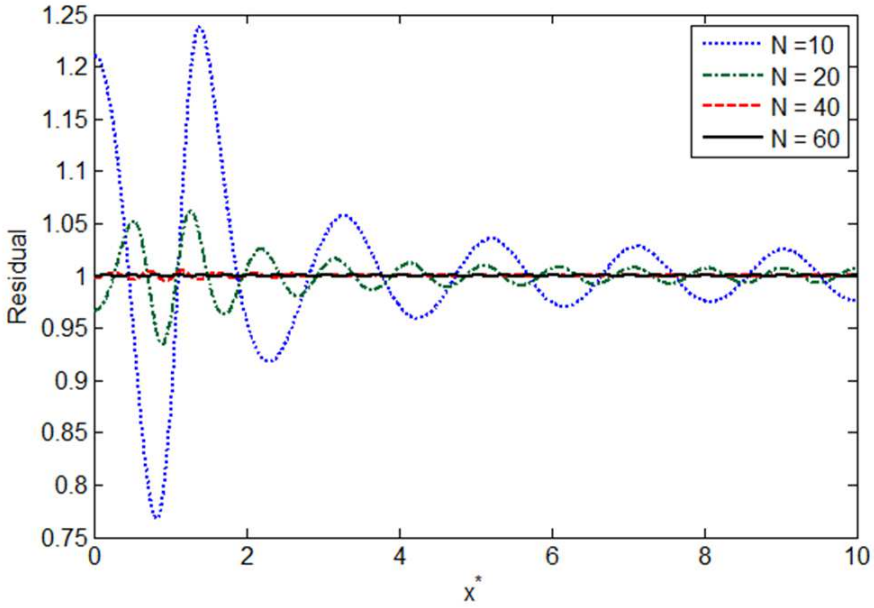

Figure 7.4. Convergence in temperature solution as a function of maximum number of eigenvalues.

foil and insulation material are considered to have isotropic properties. In order to determine the number of eigenvalues required for accuracy of the temperature solution depend strongly on the values of ρ, γ and κ. Figure 7.4 plots the residual as a function of x^* along the $y = b_2$ boundary for the case $\rho = 5$, $\gamma = 2$ and $\kappa = 1000$.

The residual is defined based on equation (7.5) as the ratio of the heat flux at the heater foil boundary exposed to jet impingement to the effect of Newton cooling, in non-dimensional sense, $Bi\ h(x)\ T_2(x, b_2)/b_2$. The residual characterizes how well the solution satisfies equation (7.5). Figure 7.4 shows that as the number of eigenvalues increases, the residual approaches the ideal value of 1. Around 60 eigenvalues are needed for the residual to be nearly 1 over the entire range of x^*. There may be significant error if a lower number of eigenvalues is used, particularly around $x^* = 1$ which represents the gradient region in the flow field.

(a) (b)

Figure 7.5. Heat flux corrections for slot jet impingement over an infinite plate with $\rho = 5$ and $\gamma = 2$, for (a) $\kappa = 100$, (b) $\kappa = 1000$.

(a) (b)

Figure 7.6. Dependence of slot jet infinite plate heat flux corrections on (a) ρ, (b) γ $\kappa = 1000$ and $Bi = 0.001$.

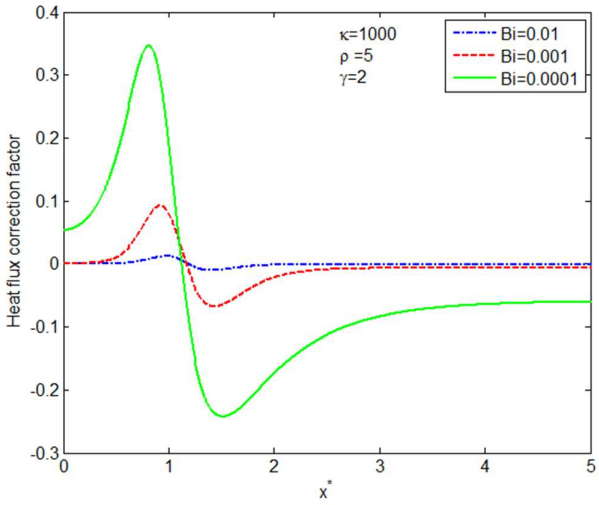

Figure 7.7. Heat flux corrections for slot jet impingement over a finite plate with $\rho = 5$ and $\gamma = 2$, for $\kappa = 1000$.

(a) (b)

Figure 7.8. Dependence of slot jet finite plate heat flux corrections on (a) ρ, (b) γ $\kappa = 1000$ and $Bi = 0.001$.

Figure 7.5(a) and 7.5(b) illustrate the effect of foil to insulation thermal conductivity ratio, κ at varying Biot numbers for the case of a slot jet impinging on an infinite plate. Figure 7.5(a) shows that for low foil-to-insulation conductivity ratio and a low value of Biot number, a large fraction of heat ($\approx 40\%$) flows inward through the foil into the insulation, even for $\kappa = 100$. This is expected as the thermal resistance offered by the insulation material is lower than that offered by the impinging jet (i.e. $h_{min}\ b_1/k_1$ is O(1)). However, this is not desirable for experiments designed

to calculate the heat transfer coefficient, as it leads to large $\bar{q}_c$, and hence incorrect measurement of heat transfer. This can be improved by proper selection of foil and insulation materials such that ($h_{min}\ b_1/k_1 = Bi\ b\ \kappa/\rho >> 1$), which is satisfied by selecting the conductivity ratio greater than 1000. For the same set of parameters and increased conductivity ratio, Figure 7.5(b) shows improved results in terms of percentage errors. Regardless, the percentage error due to lateral conduction effect is still large and can be further reduced by proper design of the experiments. For example, both Figures 7.5(a) and 7.5(b) show significantly reduced error when the Biot number is large.

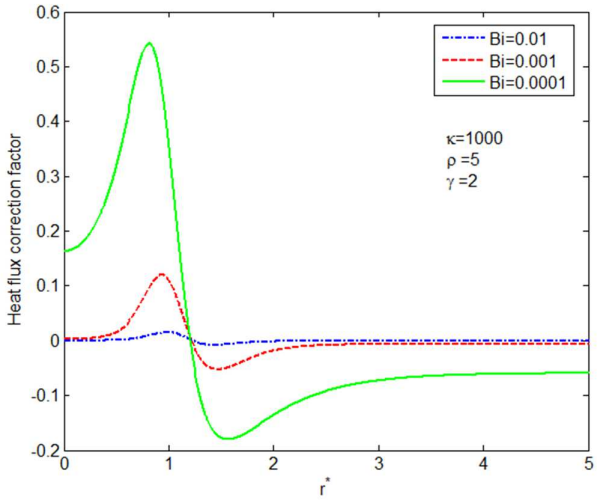

Figure 7.9. Heat flux corrections for slot jet impingement over a disk with $\rho = 5$ and $\gamma = 2$, for $\kappa = 1000$.

Similar results for slot jets are shown in Figures 7.6(a) and 7.6(b) where the non-dimensional quantities, ρ and γ are varied at a constant Biot number of 0.001. These results indicate that as the ratio of maximum to minimum heat transfer coefficient increases, the resulting error increases, as expected. The parameter γ, as described

(a) (b)

Figure 7.10. Dependence of slot jet finite plate heat flux corrections on (a) ρ, (b) γ $\kappa = 1000$ and $Bi = 0.001$.

earlier determines the gradient region of the jet. In Figure 7.6(b) for $\gamma = 5$, the profile of the jet is that of a step, and maximum error in heat flux is observed. This is because due to sudden change in the jet profile, lateral effects are predominant as compared to the $\gamma = 0.5$ case, where the jet profile does not encounter an extreme step change. Most lab-scale experiments are analyzed by considering a symmetric profile for the jet. This is a reasonable approximation to make, however by forcing the symmetric condition, the percentage error increases as shown in Figure 7.7. For instance, the peak error (e^+) in Figure 7.7 is almost double of its infinite case equivalent Figure 7.5(b) for a Biot number of 0.0001. The larger error primarily occurs due to the symmetric boundary condition forced on the side walls of the foil and insulation at $x = 0$. Figure 7.8 illustrates the variation of r and g for Biot number of 0.001 for a slot jet impinging on a finite length plate. Peak errors increase with increasing values of ρ and γ, as expected.

Figure 7.9 illustrates the comparison between the errors for a radial jet impinging on a two layered disk for $\kappa = 1000$, $\rho = 5$ and $\gamma = 2$. The peak error (e^-) is appreciable for the $Bi = 0.0001$ case. Also in addition, with reduction in magnitude of the Biot number, the conduction effects become predominant and hence the error

increases. Figure 7.10 illustrates the variation in the error for different values of ρ and γ while maintaining constant values for Bi and κ.

(a) (b)

Figure 7.11. Correlations for peak percentage error for infinite plate (a) positive error, (b) negative error.

(a) (b)

Figure 7.12. Correlations for peak percentage error for finite plate (a) positive error, (b) negative error.

The mathematical analysis in Section 7.2 is used to calculate the correction factor and peak percentage errors for a wide range of test cases spanning the Bi, ρ and γ parameter space relevant for typical experimental conditions. Based on the results, correlations for estimating the percentage errors for all cases discussed in Section 7.2 are determined. These results may be useful to experimentalists in two ways, by both facilitating better experimental design and by allowing for corrections

(a) (b)

Figure 7.13. Correlations for peak percentage error for finite plate (a) positive error, (b) negative error.

to measured data. The ratio of thermal conductivity of heater foil to insulation (κ) rarely exceeds 100 in practice. Using these values, the experimentalist can use the correlations given in Figures 7.11 - 7.13 to *a priori* estimate the error for a given Biot number, and thus adjust the dimensions of the heater foil and/or insulation thickness accordingly. This yields bounds on the maximum over- and under-estimation of the heat transfer coefficient in the vicinity of a gradient region. The correlations are, strictly speaking, valid only for the peak over- and under-estimate of the heat transfer coefficient, and do not give local corrections. However, one can observe that these maximum deviations occur at either end of the gradient region. Therefore, some information about the distribution can be obtained in the region where the errors are highest. To obtain a correction everywhere, one would have to repeat the analytical procedure presented in the paper. A power law expression is used to represent this data. The pre-factor and exponents in the power law are determined so as to minimize the least-squares error between the error predicted by the theoretical model and the power law. This procedure successfully provides correlations to accurately capture the theoretical model results for each case. Figure 7.11 presents the error from the theoretical model and from the power-law correlation for a slot jet impinging upon an infinite plate. The final form of the power law correlation is also shown. The ideal 45°

line is shown. Subsequently, correlations with similar capabilities to represent results from the theoretical models are obtained for slot jets (finite plate) and circular jets (disk), are illustrated as Figures. 7.12 and 7.13. In each case, the correlation captures nearly all data within a 10% error band. This accuracy could be improved further by neglecting test cases corresponding to extremely poor experimental design.

7.4 Appendix: Acknowledgment

This work was was generously supported from the Research Internship in Science and Engineering (RISE) Program of the Indo-US Science and Technology Forum and the Indian Institute of Science under the supervision of Dr. Vinod Srinivasan (currently at University of Minnesota, Minneapolis) is gratefully acknowledged. Assistance from Ratnesh Raj in development of correlations is also gratefully acknowledged.

CHAPTER 8

CONCLUSION AND FUTURE WORK

General temperature solutions for two class of problems in heat transfer have been derived. The results are compared to finite element models and good agreement is to be found. These results can come useful in planning thermal based therapeutics for diseases like cancer and thermal management in energy storage/conversion systems such as Lithium-ion cells.

Chapter 2, presents an analytical solution for steady state bioheat transfer in multilayer structure such as skin. This may be of significant technological importance since several cancer treatment therapies are thermally driven, and since heating and cooling of skin is carried out for various applications. The effect of heat generation within a tumor region in the skin, as well as external boundary conditions are accounted for in the models, which are found to be in good agreement with finite-element simulations. Besides improving the theoretical understanding of bioheat transport in a multilayer structure, the results discussed here is useful for estimating the thermal penetration depth which can help medical practitioners design novel thermal based therapeutics. Chapter 3, presents an analytical solution to the transient Pennes bioheat equation for multilayer perfused tissue. A detailed derivation of the analytical solution is presented. An interesting mathematical observation, for existence of both real and imaginary eigenvalues is derived and illustrated. The solution was verified against an equivalent steady state temperature solution derived from methodology developed in Chapter 2. Note that in both chapters each layer by itself is homogeneous and hence has a constant thermal conductivity although differ-

ent layers take different values. In Chapter 4, we relax this condition by assuming the tumor and surrounding tissue to have different thermal conductivity. A procedure based on Galerkin method is applied to determine the temperature anywhere in the vascular tissue subject to nanoparticle based hyperthermia therapy. The specific absorption rate (SAR) is an important parameter in planning a thermal based therapy and tumors of different shapes with different thermophysical properties will require different profiles for nanoparticle distributions and thus different SAR profiles. The work presented in chapter 4 can be viewed as a general temperature estimation tool in predictive modeling of SAR for tumors of various shapes and characteristics. In addition, the methodology developed here provides a highly accurate estimate of the temperature field factoring different physical processes that are known to occur in biological systems as suggested by the Pennes bioheat equation. In addition, in many other biological applications such as cryo-cooling a certain portion of the skin surface is exposed to heat transfer. The heat transfer in such cases varies as a function of space and one can compute the temperature field using such predictive models that can help experimentalists and medical practitioners in their discipline. For example, results developed here can be considered as solution for the direct problem for solving inverse problems in optimizing SAR distributions or temperature dependent blood perfusion rate to prevent tissue necrosis.

Solid bodies generating heat and subject to variable heat transfer is a fundamental heat transfer problem. Chapter 5, addresses the classical problem of heat transfer between a solid and the cross flow of a cooling fluid. This chapter presents an analytical technique which accounts for spatial variation of heat transfer on the cylinder surface to predict the temperature field inside the cylinder. The results presented in this chapter contribute to the fundamental theoretical understanding of an important heat transfer problem. In addition, the results may also help in understanding heat

transfer in energy conversion devices based on Li-ion cells that generate significant heat, and are known to have significant anisotropy in thermal conduction. In chapter 6, an extension of the same principle developed in chapter 5 is applied to spherical systems. The analytical technique presented here accounts for spatial variation of the heat transfer coefficient on the sphere surface, as well as orthotropic thermal conduction within the sphere. The temperature field inside the sphere is expressed in a series form, where the coefficients are determined by solving a set of linear algebraic equations. Results derived from two different approaches agree well with each other. The results presented in this chapter contribute towards the understanding of a classical heat transfer problem, and enables the analysis of an orthotropic sphere which is not possible using commercial CFD packages. This chapter may contribute towards the development of design tools for thermal management of heat-generating spherical systems with realistic convective heat transfer coefficients. Chapter 7, concludes the discussion on variable heat transfer problems by presenting an application related to heat transfer measurements by providing a tool for correction of lateral conduction error that prevails in the experimental measurements for heat transfer coefficient. A theoretical procedure to account for lateral thermal effects within a jet-cooled foil has been derived. The derivation provides a means for calculating a correction factor in the traditional heat transfer measurement methodology that accounts for two dimensional nature of thermal transport due to spatial variation in the heat transfer coefficient. Since an impinging jet is known to present sharp gradients in the heat transfer coefficient, accounting for these effects is important. Analytical solutions for the temperature distribution are derived for both slot and circular jets for a foil with insulation material at the bottom. Results indicate that the correction factor is most sensitive and is inversely proportional to the Biot number, in addition to also being dependent on $\rho$and γ . Correlations are obtained for various experimental conditions

that closely predict the peak errors obtained from the theoretical analysis. While the anisotropic nature of an insulating material is also accounted for in the theoretical model, results indicate that variation from the isotropic case is minimal. Results from this work may help improve the heat transfer measurements and design of equipments that encounter sharp gradients in heat transfer due to external flow conditions.

Finally, as part of future directions of this dissertation predictive modeling for temperature distribution in tissue will be extended for realistic SAR expressions obtained from experiments or clinical trial studies. Furthermore, the mathematical procedure will be extended to study the effect of tissue porosity in bioheat transfer. A porous tissue models accounts for non-Fourier heat conduction models based on dual phase lag theory and thus provide additional challenges in developing general temperature solution. Hence, careful consideration in developing the mathematical treatment to handle such problems is part of ongoing research. The mathematical procedure developed for accounting variable heat transfer coefficient can be efficiently applied towards estimating core temperature of solids from surface Infrared Thermography measurements [112] and in developing a thermal management tool for liquid jet impingement cooling of high heat flux microprocessors.

REFERENCES

[1] H. Wang, R. Goldstein, and S. Olson, "Effect of high freestream turbulence with large length scale on blade heat/mass transfer," in *ASME 1998 International Gas Turbine and Aeroengine Congress and Exhibition*. American Society of Mechanical Engineers, 1998, pp. V004T09A017–V004T09A017.

[2] S. Drake, D. Wetz, J. Ostanek, S. Miller, J. Heinzel, and A. Jain, "Measurement of anisotropic thermophysical properties of cylindrical li-ion cells," *Journal of Power Sources*, vol. 252, pp. 298–304, 2014.

[3] P. Pradhan, J. Giri, F. Rieken, C. Koch, O. Mykhaylyk, M. Döblinger, R. Banerjee, D. Bahadur, and C. Plank, "Targeted temperature sensitive magnetic liposomes for thermo-chemotherapy," *Journal of Controlled Release*, vol. 142, no. 1, pp. 108–121, 2010.

[4] Z. Zhang, J. Wang, and C. Chen, "Near-infrared light-mediated nanoplatforms for cancer thermo-chemotherapy and optical imaging," *Advanced Materials*, vol. 25, no. 28, pp. 3869–3880, 2013.

[5] Z. Xiao, C. Ji, J. Shi, E. M. Pridgen, J. Frieder, J. Wu, and O. C. Farokhzad, "Dna self-assembly of targeted near-infrared-responsive gold nanoparticles for cancer thermo-chemotherapy," *Angewandte Chemie*, vol. 124, no. 47, pp. 12 023–12 027, 2012.

[6] T. J. Dougherty, C. J. Gomer, B. W. Henderson, G. Jori, D. Kessel, M. Korbelik, J. Moan, and Q. Peng, "Photodynamic therapy," *Journal of the National Cancer Institute*, vol. 90, no. 12, pp. 889–905, 1998.

[7] J. Kennedy, R. Pottier, and D. Pross, "Photodynamic therapy with endogenous protoporphyrin: Ix: basic principles and present clinical experience," *Journal of Photochemistry and Photobiology B: Biology*, vol. 6, no. 1, pp. 143–148, 1990.

[8] B. W. Henderson and T. J. Dougherty, "How does photodynamic therapy work?" *Photochemistry and photobiology*, vol. 55, no. 1, pp. 145–157, 1992.

[9] D. E. Dolmans, D. Fukumura, and R. K. Jain, "Photodynamic therapy for cancer," *Nature reviews cancer*, vol. 3, no. 5, pp. 380–387, 2003.

[10] H. H. Pennes, "Analysis of tissue and arterial blood temperatures in the resting human forearm," *Journal of applied physiology*, vol. 1, no. 2, pp. 93–122, 1948.

[11] J. C. Chato, "A view of the history of heat transfer in bioengineering," *Advances in heat transfer*, vol. 22, pp. 1–18, 1992.

[12] M. M. Chen and K. R. Holmes, "Microvascular contributions in tissue heat transfer," *Annals of the New York Academy of Sciences*, vol. 335, no. 1, pp. 137–150, 1980.

[13] T.-C. Shih, P. Yuan, W.-L. Lin, and H.-S. Kou, "Analytical analysis of the pennes bioheat transfer equation with sinusoidal heat flux condition on skin surface," *Medical Engineering & Physics*, vol. 29, no. 9, pp. 946–953, 2007.

[14] C. K. Charny, "Mathematical models of bioheat transfer," *Advances in heat transfer*, vol. 22, pp. 19–155, 1992.

[15] J. Liu, "Bioheat transfer model," *Wiley encyclopedia of biomedical engineering*, 2006.

[16] F. A. Duck, *Physical properties of tissues: a comprehensive reference book*. Academic press, 2013.

[17] Z.-S. Deng and J. Liu, "Analytical study on bioheat transfer problems with spatial or transient heating on skin surface or inside biological bodies," *Journal of biomechanical engineering*, vol. 124, no. 6, pp. 638–649, 2002.

[18] S. Mahjoob and K. Vafai, "Analytical characterization of heat transport through biological media incorporating hyperthermia treatment," *International Journal of Heat and Mass Transfer*, vol. 52, no. 5, pp. 1608–1618, 2009.

[19] S. Mahjoob and K. Vafai, "Analysis of bioheat transport through a dual layer biological media," *Journal of Heat Transfer*, vol. 132, no. 3, p. 031101, 2010.

[20] K. Wang, F. Tavakkoli, S. Wang, and K. Vafai, "Analysis and analytical characterization of bioheat transfer during radiofrequency ablation," *Journal of biomechanics*, vol. 48, no. 6, pp. 930–940, 2015.

[21] M. A. Giordano, G. Gutierrez, and C. Rinaldi, "Fundamental solutions to the bioheat equation and their application to magnetic fluid hyperthermia," *International Journal of Hyperthermia*, vol. 26, no. 5, pp. 475–484, 2010.

[22] K. Chua and S. Chou, "On the study of the freeze–thaw thermal process of a biological system," *Applied Thermal Engineering*, vol. 29, no. 17, pp. 3696–3709, 2009.

[23] K. Yue, X. Zhang, and F. Yu, "An analytic solution of one-dimensional steady-state pennes bioheat transfer equation in cylindrical coordinates," *Journal of thermal Science*, vol. 13, no. 3, pp. 255–258, 2004.

[24] J. Okajima, S. Maruyama, H. Takeda, and A. Komiya, "Dimensionless solutions and general characteristics of bioheat transfer during thermal therapy," *Journal of Thermal Biology*, vol. 34, no. 8, pp. 377–384, 2009.

[25] H. Askarizadeh and H. Ahmadikia, "Analytical study on the transient heating of a two-dimensional skin tissue using parabolic and hyperbolic bioheat transfer equations," *Applied Mathematical Modelling*, vol. 39, no. 13, pp. 3704–3720, 2015.

[26] L. Hu, A. Gupta, J. P. Gore, and L. X. Xu, "Effect of forced convection on the skin thermal expression of breast cancer," *Journal of biomechanical engineering*, vol. 126, no. 2, pp. 204–211, 2004.

[27] X. He, S. Mcgee, J. E. Coad, F. R. Schmidlin, P. Iaizzo, D. J. Swanlund, E. Rudie, S. Kluge, and J. C. Bischof, "Investigation of the thermal and tissue injury behavior in microwave thermal therapy of the porcine kidney," in *Biomedical Optics 2003*. International Society for Optics and Photonics, 2003, pp. 133–144.

[28] S. Karaa, J. Zhang, and F. Yang, "A numerical study of a 3d bioheat transfer problem with different spatial heating," *Mathematics and Computers in Simulation*, vol. 68, no. 4, pp. 375–388, 2005.

[29] B. H. Dennis, R. C. Eberhart, G. S. Dulikravich, and S. W. Radons, "Finite-element simulation of cooling of realistic 3-d human head and neck," *Journal of biomechanical engineering*, vol. 125, no. 6, pp. 832–840, 2003.

[30] L. Wu, J. Cheng, W. Liu, and X. Chen, "Numerical analysis of electromagnetically induced heating and bioheat transfer for magnetic fluid hyperthermia," *IEEE Transactions on Magnetics*, vol. 51, no. 2, pp. 1–4, 2015.

[31] R. Singh, K. Das, J. Okajima, S. Maruyama, and S. C. Mishra, "Modeling skin cooling using optical windows and cryogens during laser induced hyperthermia in a multilayer vascularized tissue," *Applied Thermal Engineering*, vol. 89, pp. 28–35, 2015.

[32] J. Crezee and J. Lagendijk, "Experimental verification of bioheat transfer theories: measurement of temperature profiles around large artificial vessels in perfused tissue," *Physics in Medicine and Biology*, vol. 35, no. 7, p. 905, 1990.

[33] S. Becker and A. Kuznetsov, "Local temperature rises influence in vivo electroporation pore development: a numerical stratum corneum lipid phase transi-

tion model," *Journal of biomechanical engineering*, vol. 129, no. 5, pp. 712–721, 2007.

[34] R. Heller, M. J. Jaroszeski, D. S. Reintgen, C. A. Puleo, R. C. DeConti, R. A. Gilbert, and L. F. Glass, "Treatment of cutaneous and subcutaneous tumors with electrochemotherapy using intralesional bleomycin," *Cancer*, vol. 83, no. 1, pp. 148–157, 1998.

[35] A. Gothelf, L. M. Mir, and J. Gehl, "Electrochemotherapy: results of cancer treatment using enhanced delivery of bleomycin by electroporation," *Cancer treatment reviews*, vol. 29, no. 5, pp. 371–387, 2003.

[36] A. Attaluri, R. Ma, and L. Zhu, "Using microct imaging technique to quantify heat generation distribution induced by magnetic nanoparticles for cancer treatments," *Journal of Heat Transfer*, vol. 133, no. 1, p. 011003, 2011.

[37] Z. Qin and J. C. Bischof, "Thermophysical and biological responses of gold nanoparticle laser heating," *Chemical Society Reviews*, vol. 41, no. 3, pp. 1191–1217, 2012.

[38] A.-R. Denet, R. Vanbever, and V. Préat, "Skin electroporation for transdermal and topical delivery," *Advanced drug delivery reviews*, vol. 56, no. 5, pp. 659–674, 2004.

[39] U. Pliquett, "Mechanistic studies of molecular transdermal transport due to skin electroporation," *Advanced drug delivery reviews*, vol. 35, no. 1, pp. 41–60, 1999.

[40] M. P. Cetingul and C. Herman, "Using dynamic infrared imaging to detect melanoma: Experiments on a tissue-mimicking phantom," in *ASME 2010 International Mechanical Engineering Congress and Exposition*. American Society of Mechanical Engineers, 2010, pp. 139–147.

[41] D. Yang, M. C. Converse, D. M. Mahvi, and J. G. Webster, "Expanding the bioheat equation to include tissue internal water evaporation during heating," *IEEE Transactions on Biomedical Engineering*, vol. 54, no. 8, pp. 1382–1388, 2007.

[42] T. L. Bergman, F. P. Incropera, D. P. DeWitt, and A. S. Lavine, *Fundamentals of heat and mass transfer*. John Wiley & Sons, 2011.

[43] A. Zukauskas, E. Bagdonaite, G. Hewitt, and J. Ziugzda, *Heat Transfer of a Cylinder in Crossflow*, ser. Experimental and Applied Heat Transfer Guide Books. Springer Berlin Heidelberg, 1985. [Online]. Available: https://books.google.com/books?id=gWlYBAAACAAJ

[44] R. Nijsing, "Temperature and heat flux distribution in nuclear fuel element rods," *Nuclear Engineering and Design*, vol. 4, no. 1, pp. 1 – 20, 1966. [Online]. Available: http://www.sciencedirect.com/science/article/pii/0029549366900227

[45] H. Schlichting and K. Gersten, *Boundary-layer theory*. Springer Science & Business Media, 2003.

[46] A. D. Kraus, A. Aziz, and J. Welty, *Extended surface heat transfer*. John Wiley & Sons, 2002.

[47] H. Ünal, "Determination of the temperature distribution in an extended surface with a non-uniform heat transfer coefficient," *International journal of heat and mass transfer*, vol. 28, no. 12, pp. 2279–2284, 1985.

[48] H. Barrow, "Theoretical solution for the temperature in a straight fin with variable surface heat transfer coefficient," *Journal of heat recovery systems*, vol. 6, no. 6, pp. 465–468, 1986.

[49] S. Ma, A. Behbahani, and Y. Tsuei, "Two-dimensional rectangular fin with variable heat transfer coefficient," *International Journal of Heat and Mass Transfer*, vol. 34, no. 1, pp. 79–85, 1991.

[50] B. Vick and R. Wells, "Laminar flow with an axially varying heat transfer coefficient," *International journal of heat and mass transfer*, vol. 29, no. 12, pp. 1881–1889, 1986.

[51] B. Kundu and P. Das, "Performance analysis and optimization of straight taper fins with variable heat transfer coefficient," *International journal of heat and mass transfer*, vol. 45, no. 24, pp. 4739–4751, 2002.

[52] E. M. Mokheimer, "Performance of annular fins with different profiles subject to variable heat transfer coefficient," *International Journal of Heat and Mass Transfer*, vol. 45, no. 17, pp. 3631–3642, 2002.

[53] A. A. Nnanna, A. Haji-Sheikh, and D. Agonafer, "Effect of variable heat transfer coefficient, fin geometry, and curvature on the thermal performance of extended surfaces," *Journal of Electronic Packaging*, vol. 125, no. 3, pp. 456–460, 2003.

[54] H.-L. Lee, H.-M. Chou, and Y.-C. Yang, "The function estimation in predicting heat flux of pin fins with variable heat transfer coefficients," *Energy Conversion and Management*, vol. 45, no. 11, pp. 1749–1758, 2004.

[55] J. Taler, "Determination of local heat transfer coefficient from the solution of the inverse heat conduction problem," *Forschung im Ingenieurwesen*, vol. 71, no. 2, pp. 69–78, 2007.

[56] H.-L. Lee, Y.-C. Yang, and S.-S. Chu, "Transient thermoelastic analysis of an annular fin with coupling effect and variable heat transfer coefficient," *Journal of thermal stresses*, vol. 25, no. 12, pp. 1105–1120, 2002.

[57] Ş. Ö. Atayılmaz, "Experimental and numerical study of natural convection heat transfer from horizontal concentric cylinders," *International Journal of Thermal Sciences*, vol. 50, no. 8, pp. 1472–1483, 2011.

[58] T. M. Bandhauer, S. Garimella, and T. F. Fuller, "A critical review of thermal issues in lithium-ion batteries," *Journal of the Electrochemical Society*, vol. 158, no. 3, pp. R1–R25, 2011.

[59] D. Lisbona and T. Snee, "A review of hazards associated with primary lithium and lithium-ion batteries," *Process Safety and Environmental Protection*, vol. 89, no. 6, pp. 434–442, 2011.

[60] J. Shell, "Die wärmeübergangszahl von kugelflächen bei natürlicher konvektion, academie royale serbe," *A. Sci. Math. Phys*, vol. 4, pp. 189–194, 1938.

[61] T. Yuge, "Experiments on heat transfer from spheres including combined natural and forced convection," *Journal of Heat Transfer*, vol. 82, no. 3, pp. 214–220, 1960.

[62] T. Johnson and V. Patel, "Flow past a sphere up to a reynolds number of 300," *Journal of Fluid Mechanics*, vol. 378, pp. 19–70, 1999.

[63] H. Kramers, "Heat transfer from spheres to flowing media," *Physica*, vol. 12, no. 2-3, pp. 61–80, 1946.

[64] P. Choudhury and D. Drake, "Unsteady heat transfer from a sphere in a low reynolds number flow," *The Quarterly Journal of Mechanics and Applied Mathematics*, vol. 24, no. 1, pp. 23–36, 1971.

[65] Z.-G. Feng and E. Michaelides, "Unsteady heat transfer from a sphere at small peclet numbers," *Journal of fluids engineering*, vol. 118, no. 1, pp. 96–102, 1996.

[66] B. Abramzon and C. Elata, "Unsteady heat transfer from a single sphere in stokes flow," *International journal of heat and mass transfer*, vol. 27, no. 5, pp. 687–695, 1984.

[67] M. Rose, "What should we measure? an aero-engine turbine aero-dynamic perspective," *ROLLS ROYCE PLC-REPORT-PNR*, 1999.

[68] J.-C. Han, S. Dutta, and S. Ekkad, *Gas turbine heat transfer and cooling technology*. CRC Press, 2012.

[69] S. V. Ekkad and J.-C. Han, "A transient liquid crystal thermography technique for gas turbine heat transfer measurements," *Measurement Science and Technology*, vol. 11, no. 7, p. 957, 2000.

[70] R. Goldstein and H. Cho, "A review of mass transfer measurements using naphthalene sublimation," *Experimental Thermal and Fluid Science*, vol. 10, no. 4, pp. 416–434, 1995.

[71] S. V. Ekkad, S. Ou, and R. B. Rivir, "A transient infrared thermography method for simultaneous film cooling effectiveness and heat transfer coefficient measurements from a single test," *Journal of Turbomachinery*, vol. 126, no. 4, pp. 597–603, 2004.

[72] S. Han and R. Goldstein, "The heat/mass transfer analogy for a simulated turbine endwall," *International Journal of Heat and Mass Transfer*, vol. 51, no. 11, pp. 3227–3244, 2008.

[73] R. Vedula, D. Metzger, and W. Bickford, "Effects of lateral and anisotropic conduction on determination of local convection heat transfer characteristics with transient tests and surface coatings," in *Winter Annual Meeting of ASME, HTD-I*, 1988, pp. 21–27.

[74] M. Lin and T. Wang, "A transient liquid crystal method using a 3-d inverse transient conduction scheme," *International journal of heat and mass transfer*, vol. 45, no. 17, pp. 3491–3501, 2002.

[75] J. R. Kingsley-Rowe, G. D. Lock, and J. M. Owen, "Transient heat transfer measurements using thermochromic liquid crystal: lateral-conduction error," *International Journal of Heat and Fluid Flow*, vol. 26, no. 2, pp. 256–263, 2005.

[76] J. Bons, "Transient method for convective heat transfer measurement with lateral conductionpart i: Application to a deposit-roughened gas turbine surface," *Journal of Heat Transfer*, vol. 131, no. 1, p. 011301, 2009.

[77] J. Von Wolfersdorf, "Influence of lateral conduction due to flow temperature variations in transient heat transfer measurements," *International journal of heat and mass transfer*, vol. 50, no. 5, pp. 1122–1127, 2007.

[78] G. Vogel, A. Graf, J. Von Wolfersdorf, and B. Weigand, "A novel transient heater-foil technique for liquid crystal experiments on film-cooled surfaces," *Journal of turbomachinery*, vol. 125, no. 3, pp. 529–537, 2003.

[79] G. Caciolli, B. Facchini, A. Picchi, and L. Tarchi, "Comparison between psp and tlc steady state techniques for adiabatic effectiveness measurement on a multiperforated plate," *Experimental Thermal and Fluid Science*, vol. 48, pp. 122–133, 2013.

[80] T. Astarita, G. Cardone, L. de Luca, and G. M. Carlomagno, "Some experimental investigations on gas turbine cooling performed with infrared thermography at federico ii," *International Journal of Rotating Machinery*, vol. 2015, 2015.

[81] R. Goldstein, A. Behbahani, and K. K. Heppelmann, "Streamwise distribution of the recovery factor and the local heat transfer coefficient to an impinging circular air jet," *International journal of heat and mass transfer*, vol. 29, no. 8, pp. 1227–1235, 1986.

[82] D. Sarkar, A. Haji-Sheikh, and A. Jain, "Temperature distribution in multi-layer skin tissue in presence of a tumor," *International Journal of Heat and Mass Transfer*, vol. 91, pp. 602–610, 2015.

[83] D. Sarkar, A. Jain, and A. Haji-Sheikh, "Analytical temperature distribution in a multi-layer tissue structure in the presence of a tumor," in *ASME 2013 International Mechanical Engineering Congress and Exposition*. American Society of Mechanical Engineers, 2013, pp. V08AT09A060–V08AT09A060.

[84] D. Sarkar, A. Haji-Sheikh, and A. Jain, "Theoretical analysis of transient bio-heat transfer in multi-layer tissue," in *ASME 2015 International Mechanical Engineering Congress and Exposition*, 2015.

[85] D. Sarkar, A. Haji-Sheikh, and A. Jain, "Thermal transport in perfused biological tissue due to gold/magnetic nanoparticle heating," in *ASME 2016 NanoEngineering for Medicine and Biology Conference*, Technical Presentation, 2016.

[86] D. Sarkar, K. Shah, A. Haji-Sheikh, and A. Jain, "Analytical modeling of temperature distribution in an anisotropic cylinder with circumferentially-varying convective heat transfer," *International Journal of Heat and Mass Transfer*, vol. 79, pp. 1027–1033, 2014.

[87] D. Sarkar, A. Haji-Sheikh, and A. Jain, "Thermal conduction in an orthotropic sphere with circumferentially varying convection heat transfer," *International Journal of Heat and Mass Transfer*, vol. 96, pp. 406–412, 2016.

[88] D. Sarkar, A. Jain, R. Goldstein, and V. Srinivasan, "Corrections for lateral conduction error in steady state heat transfer measurements," *International Journal of Thermal Sciences*, vol. 109, pp. 413–423, 2016.

[89] A. Haji-Sheikh, J. Beck, and D. Agonafer, "Steady-state heat conduction in multi-layer bodies," *International Journal of Heat and Mass Transfer*, vol. 46, no. 13, pp. 2363–2379, 2003.

[90] L. Choobineh and A. Jain, "Analytical solution for steady-state and transient temperature fields in vertically stacked 3-d integrated circuits," *IEEE Transactions on Components, Packaging and Manufacturing Technology*, vol. 2, no. 12, pp. 2031–2039, 2012.

[91] S. Ghalambor, D. Agonafer, and A. Haji-Sheikh, "Analytical thermal solution to a nonuniformly powered stack package with contact resistance," *Journal of Heat Transfer*, vol. 135, no. 11, p. 111015, 2013.

[92] M. N. Ozisik, *Heat conduction*. John Wiley & Sons, 1993.

[93] T.-Y. Cheng and C. Herman, "Optimization of skin cooling for thermographic imaging of near-surface lesions," in *ASME 2011 International Mechanical Engineering Congress and Exposition*. American Society of Mechanical Engineers, 2011, pp. 351–360.

[94] D. A. Grahn and H. C. Heller, "Methods and devices for extracting thermal energy from the body core of a mammal," Dec. 2 2003, uS Patent 6,656,208.

[95] R.-V. Churchill, "Fourier series and boundary value problems." 1961.

[96] K. D. Cole, J. V. Beck, A. Haji-Sheikh, and B. Litkouhi, *Heat conduction using Greens functions*. Taylor & Francis, 2010.

[97] T. Rivlin, *Approximate Methods of Higher Analysis (LV Kantorovich and VI Krylov)*. Society for Industrial and Applied Mathematics, 1960.

[98] J. N. Reddy, *An introduction to the finite element method*. McGraw-Hill New York, 1993, vol. 2, no. 2.2.

[99] H. F. Bowman, E. G. Cravalho, and M. Woods, "Theory, measurement, and application of thermal properties of biomaterials," *Annual review of biophysics and bioengineering*, vol. 4, no. 1, pp. 43–80, 1975.

[100] S. Patankar, *Numerical heat transfer and fluid flow*. CRC press, 1980.

[101] J. P. Boyd, *Chebyshev and Fourier spectral methods*. Courier Corporation, 2001.

[102] A. Haji-Sheikh, "On solution of parabolic partial differential equations using galerkin functions," *Integral methods in science and engineering*, pp. 467–479, 1986.

[103] A. Haji-Sheikh, "Heat diffusion in heterogeneous bodies using heat-flux-conserving basis functions," *Journal of heat transfer*, vol. 110, no. 2, pp. 276–282, 1988.

[104] B. Alberts, D. Bray, J. Lewis, M. Raff, K. Roberts, J. D. Watson, and A. Grimstone, "Molecular biology of the cell (3rd edn)," *Trends in Biochemical Sciences*, vol. 20, no. 5, pp. 210–210, 1995.

[105] D. Fuentes, J. Oden, K. Diller, A. Elliott, Y. Feng, J. Hazle, A. Shetty, and R. Stafford, "Computational and mr-guided patient-specific laser induced thermal therapy of cancer."

[106] K. R. Diller, "Heat transfer in health and healing," *Journal of heat transfer*, vol. 137, no. 10, p. 103001, 2015.

[107] M. L. Etheridge, J. Choi, S. Ramadhyani, and J. C. Bischof, "Methods for characterizing convective cryoprobe heat transfer in ultrasound gel phantoms," *Journal of biomechanical engineering*, vol. 135, no. 2, p. 021002, 2013.

[108] R. A. Silverman *et al.*, *Special functions and their applications*. Courier Corporation, 1972.

[109] W. W. Bell, *Special functions for scientists and engineers*. Courier Corporation, 2004.

[110] S. Wolfram, *The Mathematica*. Cambridge university press Cambridge, 1999.

[111] M. Abramowitz and I. A. Stegun, *Handbook of mathematical functions: with formulas, graphs, and mathematical tables*. Courier Corporation, 1964, vol. 55.

[112] D. Anthony, D. Sarkar, and A. Jain, "Contactless, non-intrusive core temperature measurement of a solid body in steady-state," *International Journal of Heat and Mass Transfer*, vol. 101, pp. 779–788, 2016.

BIOGRAPHICAL STATEMENT

Daipayan Sarkar was born in Kolkata, India, in 1989. He received his B.E. degree from University of Mumbai, India, in 2010, his M.S. and Ph.D. degrees from The University of Texas at Arlington in 2012 and 2016, respectively, all in Mechanical Engineering. He has worked as a Summer Research Fellow at the Indian Institute of Science, Bangalore. His current research interests are in the area of bioheat transfer, nanoparticle assisted hyperthermia, predictive oncology, translational medicine and estimating thermal properties of novel materials for applications related to energy conversion systems. After his Ph.D., he plans to work as a Research Associate in Department of Physics, The University of Texas at Arlington where his role will be to assist medical physicists and radiation oncologists at University of Texas, Southwestern Medical Center for developing a protocol for heavy ion therapy for cancer. In addition, I will participate in a research collaboration between Prof. Kenneth Diller (Department of Biomedical Engineering, University of Texas, Austin), Prof. Robert Matthew Brothers (Department of Kinesiology, University of Texas, Arlington) and Prof. Ankur Jain (Department of Mechanical and Aerospace Engineering, University of Texas, Arlington) related to estimation of intramuscular blood perfusion rate during cryo-cooling of skin tissue. He aspires to study applied mathematics, building models for tumor growth and transport phenomena, are some of his career goals in academia. He is a member of ASME and SIAM. Please reach him by email to sdaipayan@gmail.com or daipayan.sarkar@mavs.uta.edu.